G. ÇAKIR KABAKCI

EXPERIMENTAL AND NUMERICAL ANALYSES OF REINFORCED POLYMER COMPOSITES

THE GRADUATE SCHOOL OF NATURAL AND APPLIED SCIENCES
OF
ATILIM UNIVERSITY

GAMZE ÇAKIR KABAKCI

A DOCTOR OF PHILOSOPHY THESIS
IN
THE DEPARTMENT OF MECHANICAL ENGINEERING

JUNE, 2024

ATILIM UNIVERSITY 2024

EXPERIMENTAL AND NUMERICAL ANALYSES OF REINFORCED POLYMER COMPOSITES

A THESIS SUBMITTED TO
THE GRADUATE SCHOOL OF NATURAL AND APPLIED SCIENCES
OF
ATILIM UNIVERSITY

BY

GAMZE ÇAKIR KABAKCI

IN PARTIAL FULFILLMENT OF THE REQUIREMENTS
FOR
THE DEGREE OF DOCTOR OF PHILOSOPHY
IN
MECHANICAL ENGINEERING

JUNE, 2024

Approval of the Graduate School of Natural and Applied Sciences, Atilim University.

_____

Prof. Dr. Ender KESKİNKILIÇ

Director

I certify that this thesis satisfies all the requirements as a thesis for the degree of **Doctor of Philosophy in Mechanical Engineering Department, Atilim University**.

_____

Prof. Dr. Sadık Engin KILIÇ

Head of Department

This is to certify that we have read the thesis EXPERIMENTAL AND NUMERICAL ANALYSES OF REINFORCED POLYMER COMPOSITES submitted by GAMZE ÇAKIR KABAKCI and that in our opinion it is fully adequate, in scope and quality, as a thesis for the degree of Doctor of Philosophy.

_____

Prof. Dr. Özgür Aslan

Supervisor

Examining Committee Members:

Prof. Dr. A. Hakan Argeşo
Aerospace Engineering, Atilim University _____

Prof. Dr. Özgür Aslan
Mechanical Engineering, Atilim University _____

Asst. Prof. Dr. Hakan Kalkan
Manufacturing Engineering, Atilim University _____

Asst. Prof. Dr. Ferit Sait
Mechanical Engineering, Çankaya University _____

Asst. Prof. Dr. Bahram Lotfi
Mechanical Engineering, TOBB ETÜ _____

Date: June 24, 2024

I declare and guarantee that all data, knowledge and information in this document has been obtained, processed and presented in accordance with academic rules and ethical conduct. Based on these rules and conduct, I have fully cited and referenced all material and results that are not original to this work.

Name, Last Name : GAMZE ÇAKIR KABAKCI

Signature :

ABSTRACT

EXPERIMENTAL AND NUMERICAL ANALYSES OF REINFORCED POLYMER COMPOSITES

Kabakcı, Gamze Çakır

Ph.D., Department of Mechanical Engineering

Supervisor : Prof. Dr. Özgür Aslan

June, 2024, 126 pages

Fresh scrap Low Density Polyethylene (LDPE) and Polyurethane (PU) based composites, designed with fresh scrap rubber and short carbon and glass fiber reinforcements, are thoroughly investigated regarding toughening mechanisms, mechanical and physical properties, and microstructural and fracture surface analysis. The mechanical properties of these composites are thoroughly examined to collect crucial information on fundamental material characteristics. After determining the volume percent of inclusions in the matrix, the focus shifts to the effects of the reinforcements on toughening mechanisms, with carbon and glass fibers employed to enhance the multifunctionality of the composites. Following general characterizations, additional tests and measurements are conducted. The test results are then numerically reproduced using finite element analysis (FEA) with ABAQUS/Standard. Simulations are executed with varied randomizations of inclusions across differently sized macrostructures to confirm the consistency of numerical outcomes. Representative volume elements (RVEs) featuring randomly dispersed inclusions are employed for homogenization, utilizing periodic boundary conditions (PBCs) to approximate the heterogeneous composite as a homogeneous material equivalent. The stress-strain response of the heterogeneous composite is characterized by assessing average stress and strain tensors over integration volume elements. Furthermore, a material model is implemented as a

user subroutine (UMAT) for conducting implicit nonlinear finite element calculations. Comparative analysis of numerical outcomes with experimental results verifies the reliability and accuracy of the simulation approach.

Keywords: low density polyethylene, polyurethane, recycled rubber, glass fiber, carbon fiber, scanning electron microscopy

ÖZ

GÜÇLENDİRİLMİŞ POLİMER KOMPOZİTLERİN DENEYSEL VE SAYISAL ANALİZLERİ

Kabakcı, Gamze Çakır

Doktora, Makine Mühendisliği

Tez Yöneticisi : Prof. Dr. Özgür Aslan

Temmuz 2018, 126 sayfa

Taze hurda Düşük Yoğunluklu Polietilen (LDPE) ve Poliüretan (PU) esaslı kompozitler, taze hurda kauçuk ve kısa karbon ve cam elyaf takviyeleri ile tasarlanmış olup, bu malzemelerin sertleşme mekanizmaları, mekanik ve fiziksel özellikleri ile mikroyapısal ve kırılma yüzeyi analizi açısından detaylı olarak araştırılmaktadır. Bu kompozitlerin mekanik özellikleri, temel malzeme karakteristikleri hakkında kritik bilgiler toplamak için kapsamlı bir şekilde incelenmektedir. Matris içindeki takviyelerin hacim yüzdesinin belirlenmesinden sonra, takviyelerin sertleşme mekanizmaları üzerindeki etkilerine odaklanılmaktadır; karbon ve cam elyaf takviyeleri kompozitlerin çok işlevselliklerini artırmak için kullanılmaktadır. Genel karakterizasyonların ardından ek testler ve ölçümler yapılmaktadır. Test sonuçları daha sonra ABAQUS/Standard ile sonlu elemanlar analizi (FEA) kullanılarak sayısal olarak yeniden üretilmektedir. Simülasyonlar, farklı boyutlardaki makroyapılar üzerinde farklı rastgele içeriklerle gerçekleştirilerek sayısal sonuçların tutarlılığı doğrulanmaktadır. Rastgele dağılmış içerikler içeren temsilci hacim elemanları (RVE'ler), homojenleştirme için kullanılmakta ve heterojen kompoziti homojen bir malzeme olarak yaklaşık olarak temsil etmek için periyodik sınır koşulları (PBC'ler) kullanılmaktadır. Heterojen kompozitin gerilme-şekil değiştirme tepkisi, temsili hacim elemanları üzerinde ortalama ger-

ilme ve şekil değiştirme tensörleri değerlendirilerek karakterize edilmektedir. Ayrıca, malzeme modeli, örtük doğrusal olmayan sonlu eleman hesaplamaları için bir kullanıcı altrutini (UMAT) olarak uygulanmaktadır. Sayısal sonuçların deneysel sonuçlarla karşılaştırmalı analizi, simülasyon yaklaşımının güvenilirliğini ve doğruluğunu doğrulamaktadır.

Anahtar Kelimeler: düşük yoğunluklu polietilen, poliüretan, geri dönüştürülmüş kauçuk, cam fiber, karbon fiber, taramalı elektron mikroskobu

ACKNOWLEDGMENTS

I would first like to extend my deepest gratitude to Prof. Özgür Aslan for his invaluable support in completing this thesis. I am honored to be guided by such a distinguished mentor with extensive expertise acquired in prestigious academic environments worldwide. Beyond academic endeavors, his profound vision and contributions to my life will undoubtedly leave a lasting impact on my journey.

I would like to express my sincere thanks to my colleagues at the Computational Science & Engineering Laboratory for their invaluable support and contributions to my work.

I would like to express my deep and heartfelt appreciation to my beloved parents, Muzaffer and Hatice Çakır, for their steadfast support, love, and trust throughout my life. I am deeply thankful to my dear sisters, Rüya, Başak and Burçak, for their constant belief in me and their encouragement.

My heartfelt gratitude goes to my dear husband, Nuri Kabakcı, for his unwavering support and motivation, which have been constant throughout my life. His encouragement has been my strength, and his belief in me has been a guiding light. I look forward to cherishing our profound and meaningful bond forever.

TABLE OF CONTENTS

LIST OF TABLES

TABLES

LIST OF FIGURES

FIGURES

CHAPTER 1

INTRODUCTION

Polymer-based composites have emerged as versatile and high-performance materials, widely used across various industries due to their superior mechanical properties, lightweight nature, and adaptability. Among the myriad of polymers available, Low-Density Polyethylene (LDPE) and Polyurethane (PU) are particularly noteworthy due to their unique properties and extensive range of applications [1].

LDPE is a thermoplastic polymer characterized by its low density, high ductility, and excellent chemical resistance [2]. The molecular structure of LDPE comprises long chains with significant branching, which results in its notable flexibility and toughness. These properties make LDPE an ideal material for applications that require resilience and durability under various environmental conditions. LDPE typically has a density ranging from approximately 0.91 to 0.93 g/cm³, making it one of the lightest polymers available [3]. The melting point of LDPE is around 105-115°C, which allows for easy processing and recycling [4]. LDPE exhibits a tensile strength typically between 10 and 30 MPa, providing adequate strength for many applications while maintaining flexibility [5]. With an elongation at break of over 400%, it is highly ductile and can withstand significant deformation before breaking [6]. The thermal conductivity of LDPE is in the range of 0.33-0.35 W/m·K, indicating its effectiveness as an insulating material [2]. It is resistant to alcohols, acids, and bases, but it has limited resistance to hydrocarbons, making it suitable for a variety of chemical storage applications [7]. LDPE is widely used in packaging, plastic bags, containers, and tubing due to its flexibility and chemical resistance [8]. Additionally, its low melting point allows for easy processing and recycling, contributing to its popularity in various manufacturing sectors.

Polyurethane is a versatile polymer available in various forms, including foams, elastomers, and rigid plastics. The key to PU's versatility lies in its chemistry; it is formed through the reaction of a polyol and an isocyanate, leading to a broad range of physical properties depending on the choice of reactants and processing conditions [9]. The density of PU varies, ranging from 1.0 to 1.2 g/cm³ for rigid forms, making it adaptable for both lightweight and heavy-duty applications [10]. PU can range from very soft and flexible (shore A) to very hard and rigid (shore D), allowing it to be tailored for specific applications such as flexible foams or hard protective coatings [11]. It generally exhibits a tensile strength between 10 and 100 MPa, which provides sufficient strength for both flexible and rigid applications [12]. The elongation at break for PU varies widely, from 50% to over 800%, highlighting its adaptability for applications requiring high elasticity or rigidity [11]. The thermal conductivity of PU foam is approximately 0.02-0.03 W/m·K, making it an excellent insulating material [13]. PU generally has good resistance to oils, solvents, and oxidation, enhancing its durability in various environments [14]. PU's properties make it suitable for a wide range of applications, including automotive parts, insulation materials, coatings, and adhesives. Its ability to be engineered into both flexible and rigid forms provides significant advantages in designing products with specific performance requirements.

The enhancement of polymer matrices through the incorporation of reinforcing particles has led to the development of composite materials with superior mechanical, thermal, and chemical properties. Both LDPE and PU serve as excellent matrices for such composites, benefiting from reinforcement at both the nano and macro scales. Nanoparticles such as carbon nanotubes (CNTs), graphene, and nanosilica are commonly used to enhance the properties of LDPE and PU matrices. These nanoparticles offer significant improvements in strength, stiffness, thermal stability, and barrier properties due to their high surface area and strong interfacial interactions with the polymer matrix [3]. Macro-scale reinforcements, including fibers (e.g., glass, carbon, and aramid fibers) and particulates (e.g., metal and ceramic particles), provide substantial enhancements in mechanical properties such as tensile strength, impact resistance, and dimensional stability. These reinforcements are critical in applications requiring high load-bearing capacity and structural integrity [4].

Recycled fresh scrap rubber is a promising reinforcement material due to its elasticity,

durability, and cost-effectiveness. Recycled rubber is derived from discarded tires and other rubber products, which are processed into small particles or crumb rubber. The incorporation of recycled rubber into polymer matrices not only improves the mechanical properties of the composites but also contributes to environmental sustainability by reducing waste [5]. Recycled rubber can significantly enhance the impact resistance, flexibility, and energy absorption capacity of the composite material [6]. Research has shown that incorporating recycled rubber into LDPE and PU matrices can improve the toughness and ductility of the composites, making them suitable for applications in automotive and construction industries [15].

Several studies have investigated the use of recycled rubber in polymer composites. Das et al. [16] explored the mechanical properties of LDPE composites reinforced with recycled rubber particles and found significant improvements in impact strength and elongation at break. Liu et al. [17] examined the effects of incorporating recycled rubber into PU matrices and reported enhanced tensile strength and flexibility. These studies demonstrate the potential of recycled rubber as a cost-effective and sustainable reinforcement material for polymer composites.

Carbon fibers are renowned for their high strength-to-weight ratio, excellent stiffness, and thermal stability. These fibers are typically used in high-performance applications where lightweight and high strength are crucial, such as in aerospace and automotive sectors. The tensile strength of carbon fibers can reach up to 5,000 MPa, with a modulus of approximately 230-240 GPa [18]. When incorporated into LDPE and PU matrices, carbon fibers significantly enhance the mechanical properties of the composites, including tensile strength, modulus, and fatigue resistance [7].

Glass fibers are another widely used reinforcement in polymer composites. They offer a good balance of strength, stiffness, and cost-effectiveness. Glass fibers have a tensile strength of about 3,500 MPa and a modulus of around 70-90 GPa [19]. When used in LDPE and PU matrices, glass fibers improve the dimensional stability, impact resistance, and overall durability of the composites [10]. These properties make glass fiber-reinforced composites ideal for applications in construction, marine, and automotive industries.

The comprehensive study of these polymer-based composites involves evaluating their

toughening mechanisms, mechanical and physical properties, and conducting microstructural and fracture surface analyses. Scanning electron microscopy (SEM) is often employed to investigate the microstructure, providing detailed insights into the dispersion and interaction of reinforcements within the polymer matrix. SEM analysis helps in understanding the distribution of the reinforcing materials and the quality of the interfacial bonding, which are critical for predicting the performance of the composite under various loading conditions [20].

In advanced engineering applications, particularly in aerospace and automotive sectors, the demand for lightweight, strong, and durable materials is paramount. Polymer-based composites, with their tailored properties and multifunctionality, meet these stringent requirements, offering a pathway to more efficient and environmentally friendly technologies.

The integration of numerical methods, such as finite element analysis (FEA), further aids in predicting the behavior of these composites under various loading conditions, ensuring their reliability and performance in real-world applications. FEA is a computational tool that simulates how materials and structures respond to forces, deformations, and other physical effects. This method allows researchers and engineers to model complex composite structures and predict their mechanical performance under different scenarios, including stress, strain, and thermal effects [21].

For example, Sudarisman and Davies [22] used FEA to study the stress distribution and failure modes of carbon fiber-reinforced PU composites under tensile loading. Their findings provided valuable insights into optimizing the composite's design for improved mechanical performance. Similarly, Chowdhury et al. [23] employed FEA to analyze the impact behavior of LDPE composites reinforced with recycled rubber. The study highlighted the effectiveness of recycled rubber in enhancing the composite's impact resistance, validating the experimental results through numerical simulations.

Another example is the work by Haris and Aziz [24], who used FEA to investigate the thermal properties of graphene-reinforced PU composites. Their simulations predicted significant improvements in thermal conductivity and stability, which were later confirmed through experimental tests. These examples demonstrate the critical

role of numerical methods in advancing the understanding and application of polymer composites reinforced with nano and macro-scale particles.

This thesis aims to explore the development, characterization, and application of LDPE and PU composites reinforced with macro-scale particles such as recycled fresh scrap rubber, carbon fiber and glass fiber. By examining the interplay between polymer matrices and reinforcing materials, this work seeks to contribute to the advancement of high-performance composites tailored for specific industrial applications. In the following chapters, we will delve deeper into the synthesis and processing techniques for these composites, the characterization of their properties, and a detailed analysis of their performance in various applications. Through this comprehensive study, we aim to provide insights into the potential of LDPE and PU composites to meet the growing demands of modern engineering challenges.

1.1 BACKGROUND and MOTIVATION

Polymer-based composites have become pivotal in modern engineering due to their unique ability to combine the advantageous properties of both polymers and reinforcing materials. The primary components of these composites include a polymer matrix, which acts as a binder, and various reinforcements, such as fibers or particulates, which impart strength and stiffness to the material. This combination results in materials that are lightweight yet robust, with applications spanning across numerous industries, including aerospace, automotive, marine, and construction.

Low Density Polyethylene (LDPE) and Polyurethane (PU) are two of the most commonly used polymer matrices in composite materials. LDPE is known for its flexibility, chemical resistance, and ease of processing, making it ideal for a range of applications from packaging to automotive parts. PU, on the other hand, is valued for its exceptional abrasion resistance, durability, and versatility, used in everything from coatings and foams to structural components.

The enhancement of these polymer matrices with recycled rubber and fibers such as glass and carbon fibers leads to composites with significantly improved mechanical properties. Recycled rubber not only contributes to the mechanical strength and toughness of the composites but also addresses environmental concerns by recycling waste materials. Glass fibers offer high tensile strength and stability, while carbon fibers provide exceptional stiffness, thermal stability, and low weight.

Advanced characterization techniques, including scanning electron microscopy (SEM), are employed to study the microstructure of these composites. These techniques allow for a detailed understanding of how the reinforcing materials are distributed within the polymer matrix and how they interact at the microscopic level. Such insights are crucial for optimizing the performance and reliability of the composites.

The motivation for studying LDPE and PU-based composites reinforced with recycled rubber, glass fibers, and carbon fibers stems from several key factors:

- Recycling and Waste Reduction: Incorporating recycled rubber into composites provides a sustainable solution to the disposal of rubber waste, which is

a significant environmental challenge. By repurposing waste materials, these composites contribute to the reduction of landfill use and promote a circular economy.

- Resource Efficiency: Utilizing recycled materials and enhancing them with fibers reduces the demand for virgin raw materials, conserving natural resources and minimizing the environmental footprint of composite production.

- Mechanical Performance: The addition of glass and carbon fibers to LDPE and PU matrices significantly enhances the mechanical properties of the composites, such as tensile strength, stiffness, and toughness. These improvements are critical for applications that require high performance and durability.

- Multifunctionality: Combining different types of reinforcements allows for the design of composites with tailored properties, meeting specific requirements of various applications. For instance, carbon fibers provide excellent strength-to-weight ratios, which are essential for aerospace and automotive applications.

- Cost-Effectiveness: Utilizing recycled materials and optimizing composite formulations can lead to cost savings in material procurement and waste management. Additionally, the enhanced performance of these composites can lead to longer lifespans and reduced maintenance costs in their applications.

- Innovation in Material Science: Exploring the toughening mechanisms and the interactions between different types of reinforcements within the polymer matrix can lead to the development of new materials with unprecedented properties. This research pushes the boundaries of what is possible with polymer-based composites.

- Numerical Modeling and Simulation: Integrating numerical methods such as finite element analysis (FEA) with experimental research provides a comprehensive understanding of the material behavior under various conditions. This approach not only validates the experimental findings but also guides the design and optimization of new composite materials.

In summary, the study of LDPE and PU-based composites reinforced with recycled rubber, glass fibers, and carbon fibers is driven by the need to develop sustainable, high-performance materials that can meet the demanding requirements of modern engineering applications. This research has the potential to contribute significantly to environmental conservation, economic efficiency, and technological innovation.

Figure 1.1 illustrates the flow chart depicting the motivation behind this thesis.

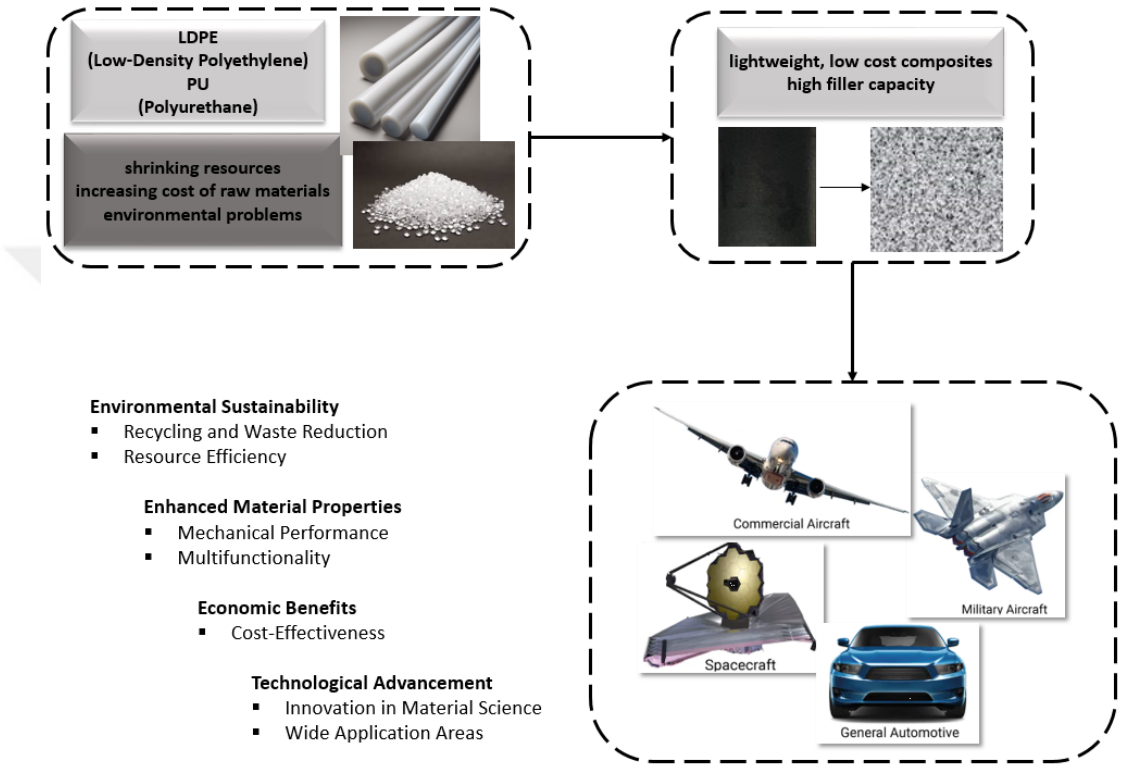

Figure 1.1: Motivation Flow Chart

In a heterogeneous structure, the size, shape, properties, and distribution of inclusions significantly influence the overall physical behavior. These inclusions can vary widely in their characteristics, leading to complex interactions within the material. However, conducting straightforward experimental observations on multiple specimens with varying phase characteristics and volume fractions is often impractical due to time and cost constraints [25].

To overcome this challenge, several homogenization techniques have been devised. These methods aim to develop a constitutive model that can be applied at the macroscopic level, providing an averaged and homogenized representation of the material's behavior. Homogenization approaches essentially bridge the gap between the microscale and macroscale, allowing for the prediction of effective properties of composite materials without the need for exhaustive experimental data.

These techniques can be broadly categorized into analytical, numerical, and semi-analytical methods. Analytical methods, such as the rule of mixtures and self-consistent schemes, provide closed-form solutions based on simplifying assumptions. Numerical methods, including finite element analysis (FEA) and computational homogenization, offer more detailed insights by simulating the material's response under various conditions. Semi-analytical methods combine elements of both approaches to balance accuracy and computational efficiency.

By utilizing homogenization techniques, researchers and engineers can design and optimize materials for specific applications more effectively. This is particularly valuable in industries such as aerospace, automotive, and construction, where material performance under various conditions is critical. The development of robust constitutive models through homogenization not only saves time and resources but also enhances the ability to predict material behavior in real-world applications, leading to safer and more efficient designs.

Within the realm of analytical estimates, micromechanical models such as the Halpin-Tsai model [26] and the Mori-Tanaka model [27] are utilized to predict the elastic properties of composites. These models consider the geometry, orientation of inclusions, and the elastic properties of both the filler and the matrix. The Halpin-Tsai model is a mathematical approach utilized to estimate the modulus of composite

materials [26], [28]. It relies on averaging the individual properties of the components to calculate the overall property. This method is suitable for linear material properties, such as elastic moduli, and primarily considers the volume ratio of the heterogeneities. Additionally, equivalent material properties can be derived through the analytical solution of a boundary value problem using the Eshelby model [29] and other self-consistent approaches developed by researchers such as Hashin [30], Hashin and Shtrikman [31], and Hill [32]. These models provide a framework for understanding the macroscopic behavior of composites by averaging the properties of the microscale components. As another mathematical approach, asymptotic expansion theory has been developed to provide effective overall properties as well as local stress and strain values. This theory, advanced by Sanchez-Palencia [33] and Bensoussan, Lions, and Papanicolaou [34], is particularly useful for simple microscopic geometries. The macroscopic linear properties have also been investigated by Beran [35] and Torquato [36], who have contributed significantly to the understanding of the statistical nature of material properties. Research on the random distribution of heterogeneities in materials has been conducted by Milton [37], Chaboche et al. [38], Kroner [39], Sanchez-Palencia and Zaoui [40], and Nemat-Nasser [41]. These studies have provided valuable insights into the behavior of composites with randomly distributed inclusions, further enhancing the predictive capabilities of micromechanical models.

In computational homogenization, the behavior of heterogeneous composite materials is governed by constitutive laws and the spatial distribution of material components. The literature offers numerous in-depth studies on numerical homogenization methods. Suquet [42], [43] has applied the averaging approach to solve nonlinear problems across two scales. By using the deformation gradient tensor to address the problem at the microscopic level, the averaging formulation is then applied to produce the macroscopic stress tensor. Hill [44] introduced the concept of a representative volume element (RVE), typically defined as a volume of heterogeneous material large enough to be statistically representative of the composite. The finite element method is employed to perform analysis at the RVE level, as demonstrated by Terada and Kikuchi [45], Smit [46], Smit et al. [47], Miehe et al. [48], and Feyel and Chaboche [49]. Their work has been instrumental in the application of finite element methods

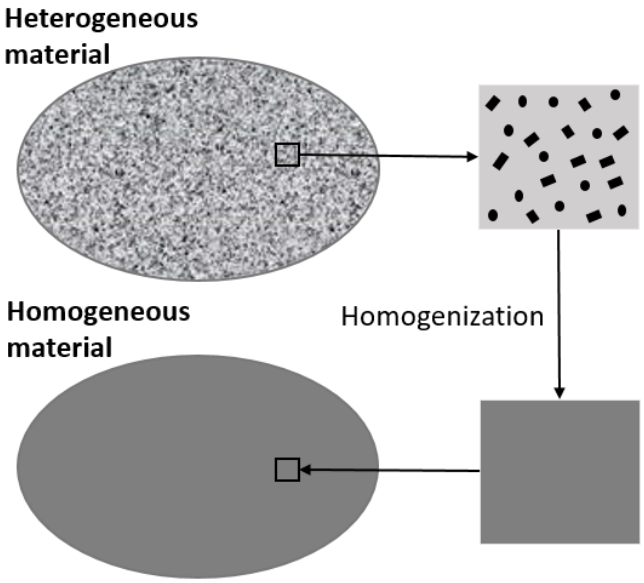

Figure 1.2: Homogenization Scheme of Composite Materials

to homogenization problems, enabling detailed analysis of composite materials.

The contributions of Moulinec [50] and Miehe [51] have extended these approaches to accommodate large deformations with arbitrary nonlinear material behavior at the microscale. This has significantly broadened the applicability of computational homogenization techniques to more complex and realistic material behaviors. Geers and Kouznetsova [52, 53, 54] have developed a second-order homogenization technique that solves boundary value problems at the microscale using the deformation gradient tensor and the corresponding Lagrangian gradient [55]. This advanced method allows for more accurate modeling of material behavior under various loading conditions. Multi-scale computational homogenization scheme is presented in Figure 1.2.

Overall, multi-scale computational homogenization schemes have evolved to provide a robust framework for predicting the behavior of composite materials. These methods are essential for designing and optimizing materials in various engineering applications, ensuring that their macroscopic properties can be reliably predicted from their microscopic structures. The comprehensive study and development of these techniques continue to enhance our understanding and capabilities in material science and engineering.

In this thesis, fresh scrap Low Density Polyethylene (LDPE) and Polyurethane (PU)

composites, designed with fresh scrap rubber, short carbon, and glass fibers, are investigated in detail. The research centers on investigating toughening mechanisms, along with analyzing the mechanical and physical properties, as well as conducting microstructural and fracture surface analyses of these composites. Detailed scrutiny of the mechanical properties aims to collect essential data on fundamental material parameters.

To assess the mechanical behavior of the composites comprehensively, uniaxial compression tests are conducted to determine their stress-strain responses under controlled conditions. Following these experimental tests, the Halpin-Tsai (H-T) model, which applies a rule-of-mixtures approach, is employed. This model calculates the homogenized moduli of the composite materials by considering the properties of their individual components.

Additionally, to delve deeper into the mechanical properties of the polymer-based composites, their uniaxial response is further investigated through macromechanical finite element simulations using ABAQUS/Standard software. These simulations allow for detailed analysis of how the composite materials behave under various loading conditions, providing insights into their structural integrity and performance characteristics.

Representative Volume Elements (RVEs) serve as essential tools for homogenization, containing a random distribution of inclusions within their defined square domain. The size of each RVE, specifically the length of its edge, is carefully chosen based on the designated number of inclusions and their volume fraction. To ascertain the isotropic effective elastic properties of the composite material, periodic boundary conditions are applied rigorously across the RVEs.

During the analysis process, the average strain and stress tensors are meticulously computed over the integration volume elements within each RVE. This detailed evaluation provides a comprehensive description of the material's stress-strain behavior under varying conditions, ensuring accurate predictions of its mechanical response.

This comprehensive analysis provides insights into the mechanical performance of LDPE and PU composites, aiding in the development of materials with enhanced

properties for various engineering applications. The use of advanced modeling techniques and simulations ensures a thorough understanding of the composites' behavior under different loading conditions, contributing to the optimization and design of high-performance composite materials.

1.2 OBJECT AND SCOPE

In this thesis, Low Density Polyethylene (LDPE) and Polyurethane (PU) based composites, designed with fresh scrap rubber, short carbon fibers, and glass fibers, are thoroughly investigated. The study focuses on the toughening mechanisms, mechanical and physical properties, as well as microstructural and fracture surface analysis. The mechanical properties of the composites are extensively examined to gather basic material parameters.

Following the initial characterization of the composites, further tests and measurements are carried out to investigate the time-dependent behavior and toughening mechanisms. Three specific compositions are selected for detailed analysis. Representative Volume Elements (RVEs) are defined for these chosen compositions, ensuring that their properties enable a continuum representation that accurately mimics the behavior observed at the RVE level.

The macroscopic responses obtained from experimental tests are subsequently compared with the numerical responses of the RVEs. This comparison is conducted under appropriate boundary conditions, revealing a high degree of similarity between the experimental and numerical results. This validation confirms the accuracy and reliability of the numerical approach in predicting the mechanical behavior of the composites.

The objectives of this thesis are presented in the following list:

- Design and manufacture LDPE and PU composites incorporating fresh scrap rubber, short carbon fibers, and glass fibers as volume fillers and reinforcements.
- Conduct surface modification of polymers and reinforcements to enhance composite performance.
- Identify the impact of inclusions on material properties and fracture toughness using a variety of laboratory tests.
- Develop numerical models of the macrostructure of the composites.
- Generate several RVEs for the candidate compositions.

- Implement the homogenization model in finite element analysis (FEA) software, specifically ABAQUS/Standard.
- Numerically reproduce basic characterization tests to validate the models.
- Validate the numerical approach by comparing specific test results with existing analytical approaches and finite element method (FEM) results.
- Perform implicit nonlinear finite element calculations using the user subroutine UMAT.

CHAPTER 2

REINFORCED POLYMER-BASED COMPOSITES

2.1 Experimental Study

2.1.1 General Characteristics of the Materials

2.1.1.1 Fresh Scrap Low Density Polyethylene (LDPE)

LDPE is a thermoplastic made from the monomer ethylene. Known for its low density and high flexibility, it is widely used in applications such as plastic bags, containers, and various types of packaging. LDPE is valued for its chemical resistance, durability, and ease of processing [56].

Fresh scrap LDPE refers to the leftover material from manufacturing processes, which has not yet been subjected to any post-consumer use. This type of scrap is often cleaner and more uniform in composition compared to post-consumer LDPE, making it an attractive source for recycling [57]. Recycling fresh scrap LDPE involves melting and reforming the plastic, which can then be reused in similar applications or in the production of new products [58].

2.1.1.2 Fresh Scrap Polyurethane (PU)

Polyurethane is a versatile polymer available in various forms, including foams, elastomers, and coatings. It is renowned for its excellent abrasion resistance, flexibility, and load-bearing capacity. PU is commonly used in furniture, automotive parts, insu-

lation, and footwear [59].

Fresh scrap PU, like LDPE, is a by-product of the manufacturing process. It includes off-cuts, trimmings, and other remnants that are typically clean and uncontaminated. Recycling PU is more challenging than LDPE due to its thermosetting nature, but advances in chemical recycling and mechanical processing are making it increasingly feasible [60].

2.1.1.3 Fresh Scrap Recycled Rubber (NBR)

The recycled rubber utilized in this thesis is sourced as fresh scrap directly from the production line by sports equipment manufacturers. It is devoid of any metallic inclusions. The rubber particles exhibit an average diameter ranging from 30 to 50 μm, with a density of 1.5 g/cm^3. The material possesses a modulus of elasticity measuring 10 MPa, an elongation at break of 80–100 %, and a hardness between 37 and 40 "Shore A".

2.1.1.4 Carbon Fibers (CFs)

One of the most notable properties of carbon fiber is its high tensile strength. Carbon fibers possess tensile strengths that can exceed 4,000 MPa. It also exhibits a high modulus of elasticity ranging from 200 to 800 GPa, carbon fiber-reinforced composites can maintain their shape under high stress, offering structural integrity and rigidity. This property is particularly beneficial in aerospace and automotive applications, where maintaining shape and performance under load is crucial. Carbon fiber has also excellent thermal stability, allowing it to maintain its properties at elevated temperatures.

2.1.1.5 Glass Fibers (GFs)

Glass fibers are characterized by their high tensile strength, which can range from 3,400 to 4,800 MPa. The modulus of elasticity of glass fibers typically ranges from

70 to 90 GPa. They have a density of 2.45 g/cm^3, softening temperature is found around 1000°C and thermal expansion is about at the level of 2.85 μm °C.

2.1.2 Manufacturing of LDPE and PU based Composites

Fresh scrap LDPE and PU based composites have been designed with fresh scrap rubber (major), short carbon and glass fiber reinforcements. An economical and safe process has been developed for manufacturing polymer-based composites reinforced with recycled rubber powder, as well as short carbon and glass fibers. To enhance the interface quality between the polymer matrix and the reinforcements, a special pre-treatment process is applied to ensure successful composite production.

Prior to mixing with the polymer matrix, the reinforcements undergo a drying process at 50°C in a sterilizer-oven for 48 hours. This drying step is crucial for removing moisture, thus ensuring efficient and strong chemical bonding between the matrix and reinforcements. After drying, the reinforcements are blended with the polymer matrix at a speed of 1200 rpm for 10 minutes to achieve a preliminary uniform mixture. Following this, the mixture is subjected to a milling process for 4 hours at 250 rpm. During milling, 3 wt% of Zn-Stearate dry lubricant is added to the mixture. The lubricant aids in achieving a homogeneous distribution of the reinforcements throughout the polymer matrix.

The final stage of the manufacturing process involves hot compaction. The blended and milled mixture is compacted at 200°C for 20 minutes under a pressure of 30 MPa. This step consolidates the composite material, ensuring proper adhesion and integration of the reinforcements within polymer matrix.

A similar procedure is given in Figure 2.1. This process effectively produces polymer-based composites with enhanced mechanical properties, owing to the optimized interface bonding and uniform distribution of recycled rubber powder, short carbon fibers, and glass fibers. The careful control of processing parameters ensures the economic viability and safety of the manufacturing process. Figure 2.2 depicts the equipment employed during the process. Finally, depending on the type of test, the specimens are produced in different sizes to meet the specific requirements and standards of each

testing method. They are cut by waterjet and metallographic cut-off machine (Figure 2.3).

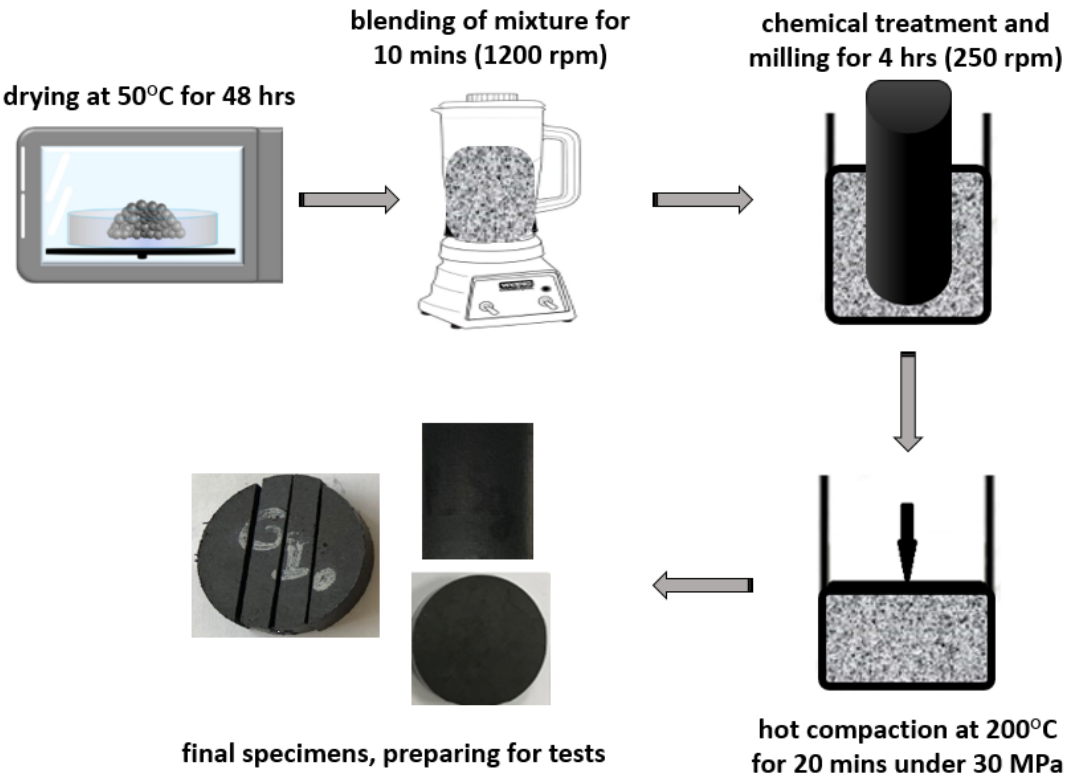

Figure 2.1: Manufacturing steps of polymer-based composites

Figure 2.2: Milling (left) and hot compaction (right) of the mixture

Figure 2.3: Waterjet (left) and metallographic cut-off machine (right)

2.1.3 Compositions

Low Density Polyethylene (LDPE) and Polyurethane (PU) have been reinforced with fine fresh scrap rubber powder (NBR), carbon fibers (CFs) and glass fibers (GFs) to provide multifunctionality to the composites.

In manufacturing the composite matrix, 60 weight percent (wt %) of polymer and 30 wt % of recycled rubber are employed. Furthermore, to enhance strength and durability, 5 volume percent (vol %) of carbon fibers (CFs) and 5 vol % of glass fibers (GFs) are integrated as reinforcements within both LDPE and PU matrices. Table 2.1 details the chemical compositions of the composites used in specimen preparation.

Table 2.1: Chemical composition of LDPE and PU composites.

Composite Name	Matrix	Rubber (NBR) (wt %)	Carbon Fiber (CF) (vol%)	Glass Fiber (GF) (vol%)	Bismuth Oxide (Bi_2O_3) (wt %)	Graphene Nanoplatelets (GNP) (wt %)
LDPE-I	LDPE	30	5	5	0.15	0.15
PU-I	PU	30	5	5	0.15	0.15

2.1.4 Characterization Tests

2.1.4.1 Density and Surface Hardness Measurement

Density measurements are conducted using a pycnometer to accurately determine the volume (see Table 2.2). Also, mass measurements are recorded by a high sensitive balance.

Table 2.2: Density of the composites

Composite Name	Density (g/cm^3)
LDPE-I	1.41
PU-I	1.59

After post curing in drying oven again 24 hours, hardness measurements on the specimens are performed by using Shore D hardness test device on the polished flat surfaces of the specimens (see Figure 2.4).

Figure 2.4: Shore D hardness tester

In the Shore-D hardness test, measurements were taken from at least five different points on the specimen surface, and the average values are summarized in Table 2.3. Generally, the fillers used as reinforcements enhance surface hardness.

Table 2.3: Shore D hardness measurements of the composites

Composite Name	Shore-D Hardness
LDPE-I	96 ± 10
PU-I	98 ± 10

The hardness values of these composites surpass those typically found in conventional polymer-based components, demonstrating the beneficial influence of reinforcement particles. Achieving uniform enhancement of surface hardness across the entire surface is essential for optimizing the performance of these novel polymer-based composite designs. This uniform hardness is critical for improving toughness in tribological applications, where surfaces are subjected to friction and potential surface damage from contact with other components.

2.1.4.2 Differential Scanning Calorimetry (DSC)

As is well known, differential scanning calorimetry (DSC) is a powerful analytical technique employed to measure several key properties of samples extracted from composites. This thermal analysis method is particularly useful for identifying fusion points, crystallization points, and glass transition temperatures (T_g).

In DSC, a sample and a reference material are subjected to a controlled temperature program. The technique measures the difference in heat flow between the sample and the reference as a function of temperature. This difference in heat flow provides insights into endothermic and exothermic processes occurring within the sample, such as melting, crystallization, and glass transitions.

In this study, DSC experiments on polymer-based composites determine their transformation points. The results present heat flux (mW) versus temperature (°C) curves, shown in Figures 2.5 and 2.6. These curves are instrumental in calculating the enthalpies of transitions by integrating the peaks corresponding to specific transitions.

Moreover, DSC analysis provides valuable insights into the thermal behavior of materials, helping to understand the stability and performance of the composites under various temperature conditions. By analyzing the DSC curves, researchers gain information about the material's thermal history, phase transitions, and the degree of crystallinity, which are crucial for optimizing the composite's properties for specific applications.

Additionally, DSC can be used to assess the purity of materials, as impurities typically alter the melting behavior of a substance. This technique also aids in the study of polymer curing processes, degradation, and the effect of additives or fillers on the polymer matrix.

Overall, DSC is a versatile and essential tool in the field of material science, providing comprehensive thermal profiles that are critical for the development and quality control of composite materials.

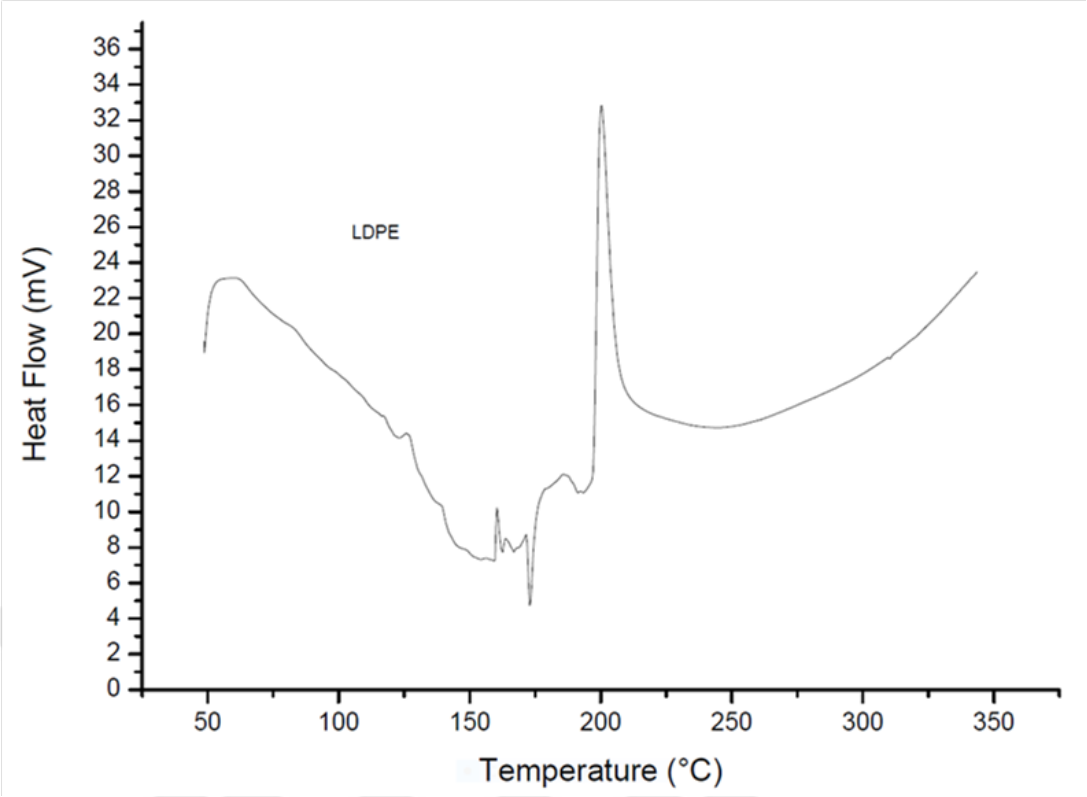

Figure 2.5: Differential Scanning Calorimetry (DSC), for composite LDPE-I to optimize hot compaction levels during manufacturing

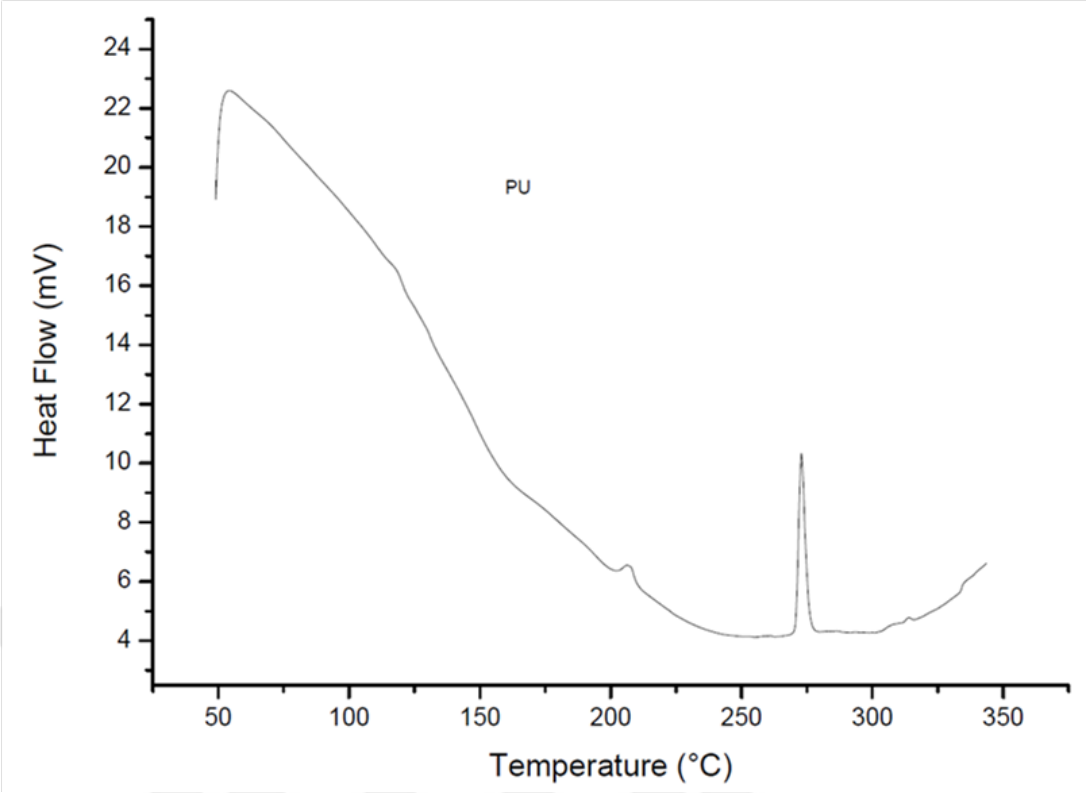

Figure 2.6: Differential Scanning Calorimetry (DSC), for composite PU-I to optimize hot compaction levels during manufacturing

2.1.4.3 Incremental Cyclic Compression Tests

In this study, incremental cyclic compression tests are conducted up to failure to observe saturation, load absorption, and hardening phenomena during cyclic loading. All of the composites exhibit stress relaxations at the peak of loading, with $\Delta\sigma$ ranging from 3 to 6 MPa. This stress relaxation occurs due to the saturation of the microstructure during cyclic loading, which closes micro-porosities and leads to hardening of the structure through the interaction between the reinforcements and the matrix.

During the cyclic loading, significant plastic deformation regularly occurs in the LDPE-based composite specimens, as shown in Figures 2.7 and 2.8. This plastic deformation indicates the material's response to repeated loading and unloading cycles, revealing its ability to absorb energy and redistribute stresses.

These findings should align with the results from impact shock and drop weight tests, which are discussed in the next subsection. These tests will provide additional insights into the composites' behavior under dynamic loading conditions, further validating the observations from the cyclic compression tests. Understanding these behaviors is crucial for evaluating the material's performance and durability in real-world applications, such as automotive, aerospace, and construction industries.

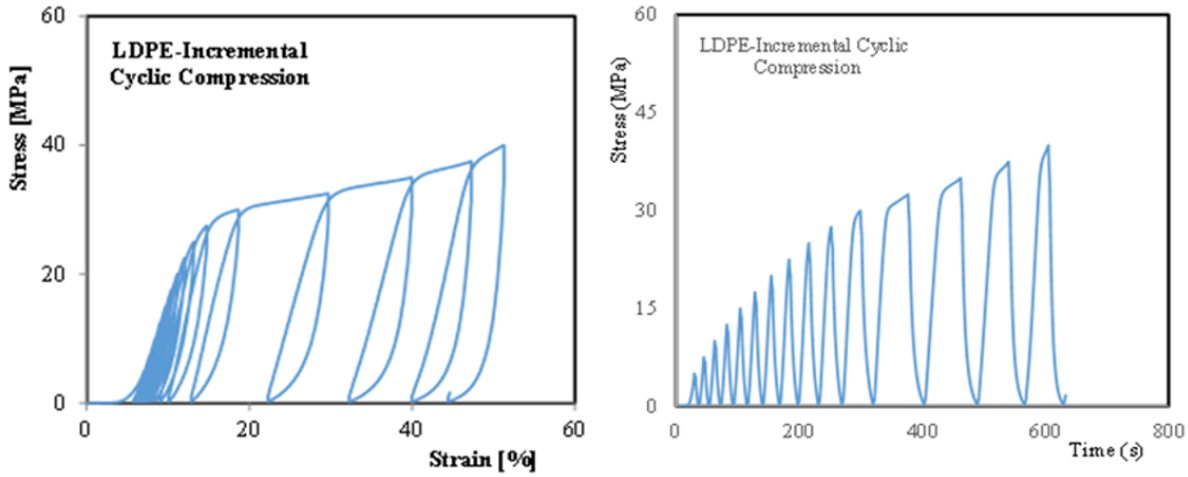

Figure 2.7: Incremental cyclic compression tests for LDPE-I

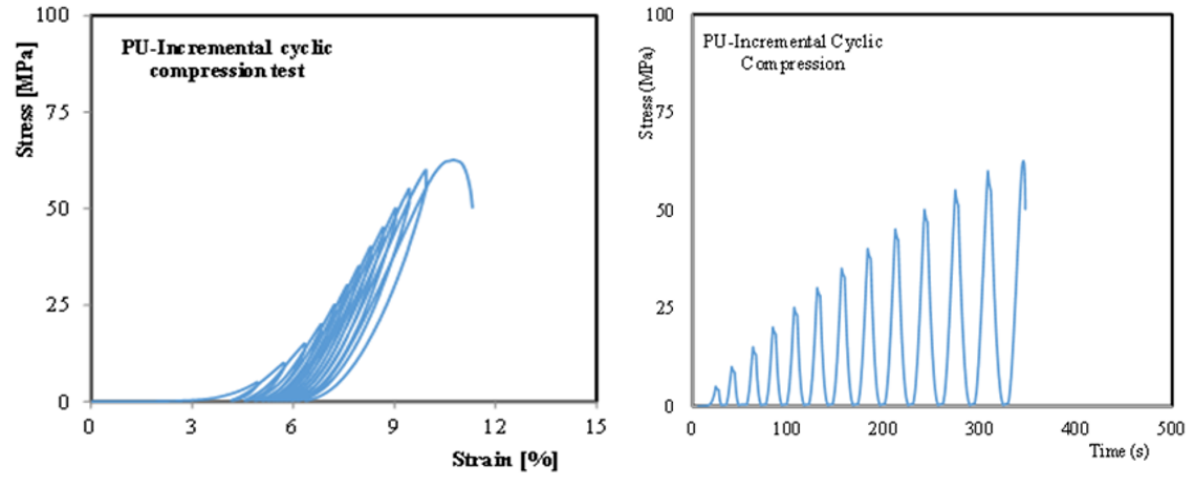

Figure 2.8: Incremental cyclic compression tests for PU-I

2.1.4.4 Low Velocity Impact Testing (Drop Weight Test)

Dynamic compression tests are conducted using a specialized drop weight test apparatus. In these tests, a standard flat-bottom punch is released from a predetermined height to impact the test specimens. The impact behavior of the manufactured composites is monitored and analyzed through force-time curves generated during the tests. The apparatus used for the drop weight tests, as well as a schematic representation of the testing process, are illustrated in Figure 2.9. These figures provide a clear overview of the experimental setup and the method employed to evaluate the impact performance of the composite materials.

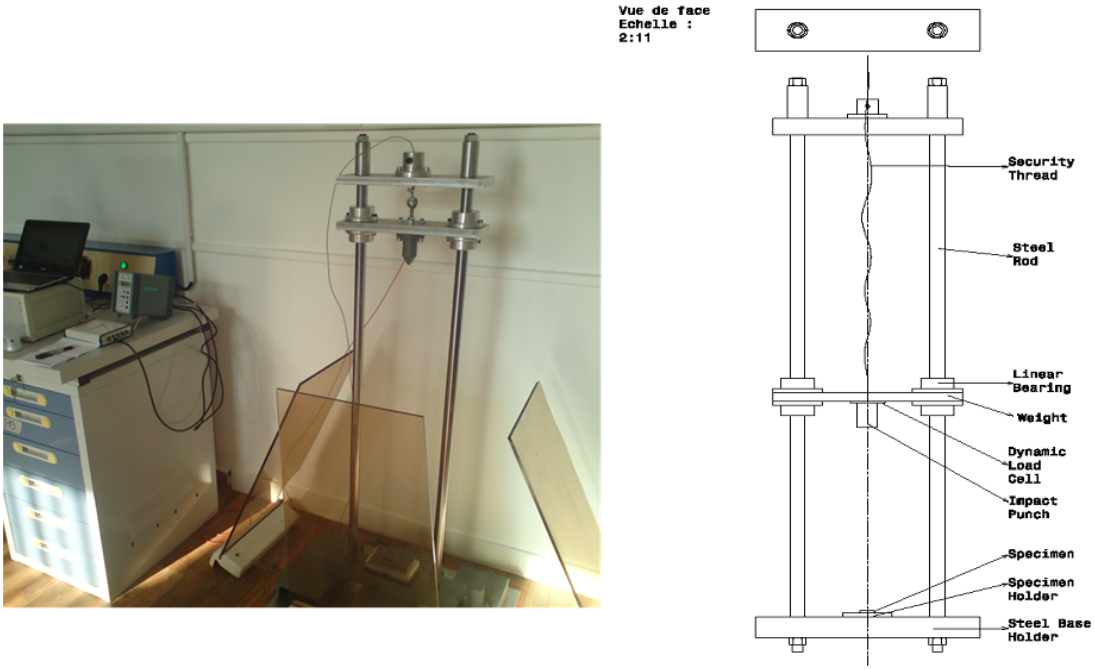

Figure 2.9: Drop weight test apparatus (left) and schematic drawing (right)

The conversion of potential energy into kinetic energy is determined by the drop height and the mass of the impactor. When the impactor head contacts the specimen, the impact energy is

$$K = \frac{1}{2}mv^2 \tag{2.1}$$

where m is the drop mass and v is the impact velocity. The performance of specimen in terms of energy absorption is assessed by the ratio of energy absorbed by the specimen to the impact energy of the impactor. Newton's second law of motion dictates the impact force.

$$F_i = ma_i \tag{2.2}$$

in which a_i is the measured deceleration of the impactor assembly. The energy absorption is determined by the closed area under the load-displacement curve. By applying the trapezoidal method, the curve up to the maximum load is divided into multiple smaller trapezoids. The energy absorption value is then calculated as the total sum of the areas of these small trapezoids as follows:

$$E = \sum I_i = \frac{1}{2}\sum_{i=0}^{n}(F_{i+1} + F_i)(x_{i+1} - x_i) \tag{2.3}$$

E is the absorbed energy, I_i is the trapezoidal area, F_i is the contact force and x_i is the displacement increment caused by the impact force at each time interval.

Drop weight tests are conducted to observe the impact behavior of these composites through force-time curves. For these tests, the drop mass is 1.9 kg, and the impact speed, accounting for friction, is calculated to be 3.2 m/s. The impact energy is calculated using Equation (2.2), resulting in 9.728 J. The force-time curves for compositions LDPE-I and PU-I are presented in Figure 2.10.

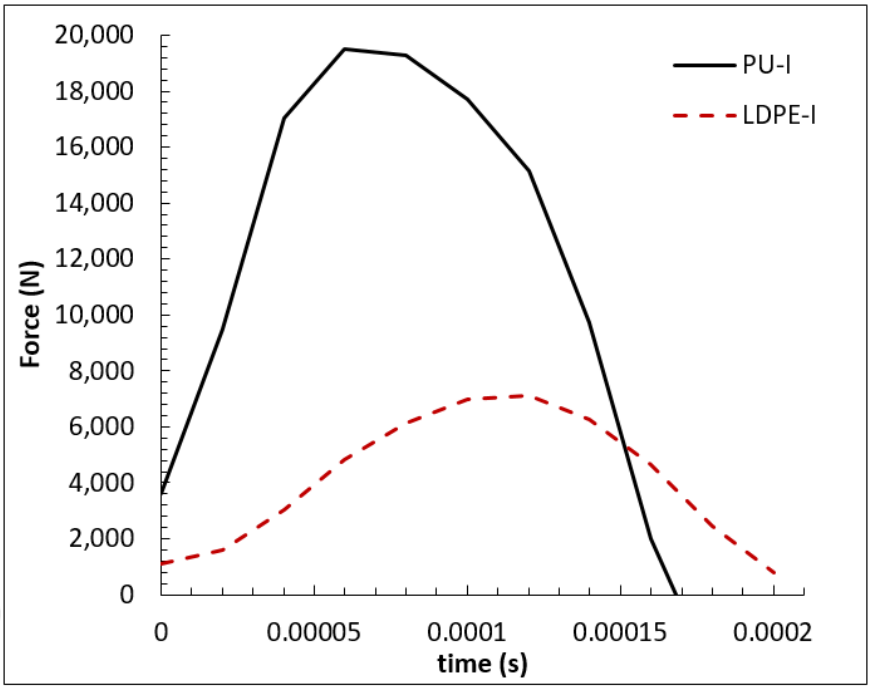

Figure 2.10: Force-time curves of the composites LDPE-I and PU-I

The time integral of the impact force over time is computed to determine the area under the force-time curve, which is used to calculate a_i from Equation (2.2). By performing first and second integrals of acceleration, the velocity and displacement history of the drop can be obtained. Consequently, force-displacement curves are plotted for compositions LDPE-I and PU-I in Figure 2.11. As depicted in this figure, the area under the load-displacement curve visually represents the absorbed energy.

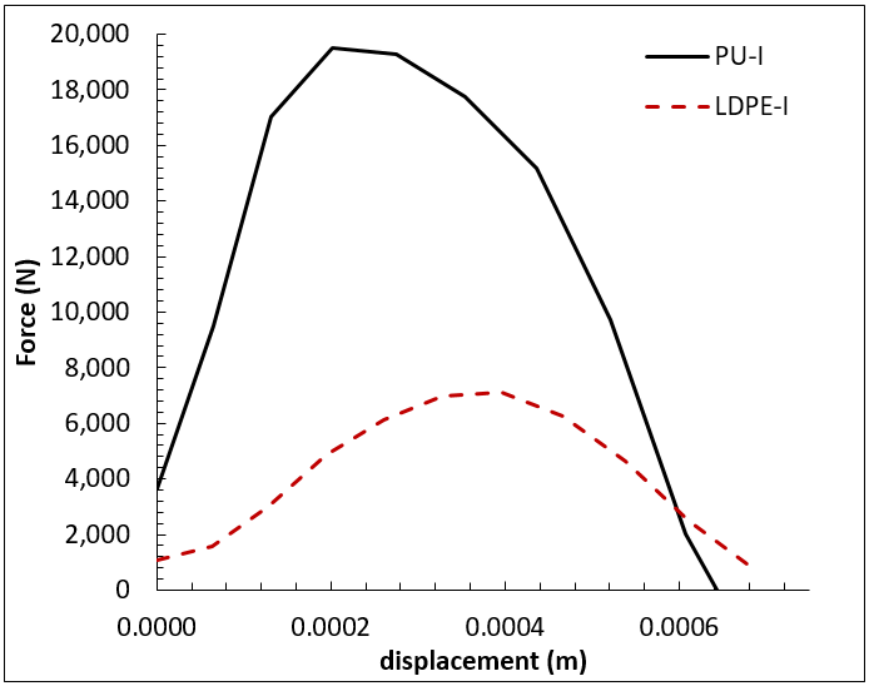

Figure 2.11: Force-displacement curves of the composites LDPE-I and PU-I

Table 2.4 provides data on the energy absorbed on impact and the energy absorption performance.

Table 2.4: Average results for the energy absorption performance

Composite Name	Impact Energy, K (J)	Energy absorbed, E (J)	Energy absorption (%)
LDPE-I	9.728	3.02	31.04
PU-I	9.728	8.38	86.13

2.1.4.5 Three Point Bending (3PB) Fatigue Test Analyses

Three-point bending (3PB) fatigue tests are conducted on the polymer-based composites, LDPE-I and PU-I, to evaluate their time-dependent behavior under cyclic loading, simulating real service conditions.

All tests are performed on a developed fatigue test device (see Figure 2.12), with maximum stress controlled at three different frequencies: 8, 10, and 12 Hz, in Mode II according to ASTM D790 standards. The primary objective is to subject the test samples to conditions that closely mimic real-world service environments, evaluating the influence of different frequencies on fatigue damage behavior.

For each fatigue test, a pre-stress is applied to all specimens to estimate their stiffness and displacement amplitude during cyclic loading. The stiffness values, dependent on key parameters obtained from the fatigue tests, are calculated using the following equation:

$$stiffness(N/mm) = \frac{F(amplitude)}{D(amplitude)} = \frac{F_{max} - \frac{F_{max}+F_{min}}{2}}{D_{max} - \frac{D_{max}+D_{min}}{2}} \tag{2.4}$$

Figures 2.13 and 2.14 present the results for two different composite structures. Each specimen shows a specific evolution of stiffness and displacement amplitude depending on the number of cycles at different frequencies. However, the frequency does not significantly affect these composites under laboratory conditions.

The maximum stress controlled remains constant throughout the tests, ensuring the reliability of the fatigue tests. As observed, stiffness decreases regularly, while displacement amplitude increases as cracks initiate and propagate. At the final stage of fatigue life, stiffness decreases significantly, and displacement amplitude increases drastically.

Fatigue life for the specimens tested in this study varies from 1.10^6 to 6.10^6 cycles. The PU-I composite specimens exhibit slightly higher fatigue resistance compared to the LDPE-I.

These findings provide valuable insights into the fatigue behavior of polymer-based

composites, contributing to the development of materials with improved performance and durability in real-world applications.

The fatigue test results reveal several critical aspects of the composites' behavior under cyclic loading. The 3PB fatigue tests effectively simulate the long-term performance of composites under repeated stress, which is essential for predicting their lifespan in practical applications. By testing at different frequencies (8, 10, and 12 Hz), the study assesses how varying loading rates influence fatigue damage. While the frequency does not have a significant effect under laboratory conditions, it is important to consider in real-world scenarios where loading rates can vary.

The evolution of stiffness and displacement amplitude provides insights into the stages of crack initiation and propagation. Monitoring these parameters helps in understanding the material's failure mechanisms and improving its resistance to fatigue. The slightly higher fatigue resistance of PU-I composites suggests that this material might be better suited for applications requiring high fatigue endurance. This information can guide material selection and design in industries such as automotive, aerospace, and construction.

The consistency of the maximum stress controlled during the tests ensures that the observed fatigue behavior is reliable and reproducible. This consistency is crucial for developing standardized testing protocols and for ensuring that the composites perform as expected in real-world applications.

In conclusion, the 3PB fatigue tests provide comprehensive data on the fatigue behavior of LDPE-I and PU-I composites, helping to optimize their design and application for enhanced performance and durability in various industrial sectors.

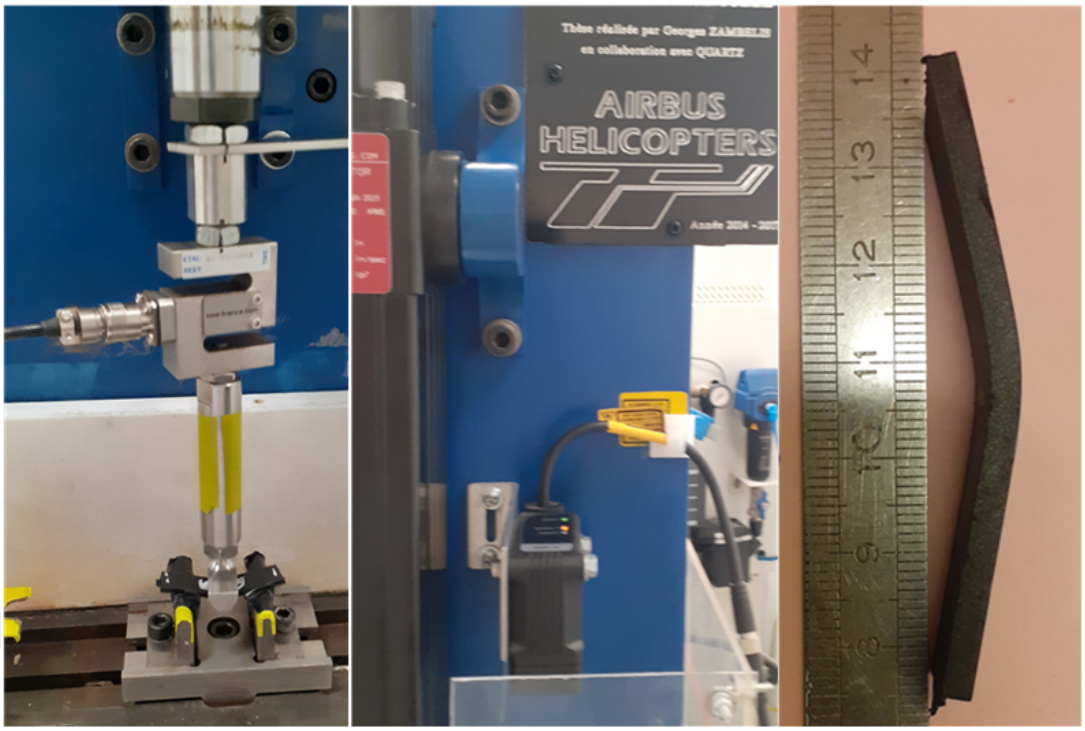

Figure 2.12: 3PB-Fatigue test device

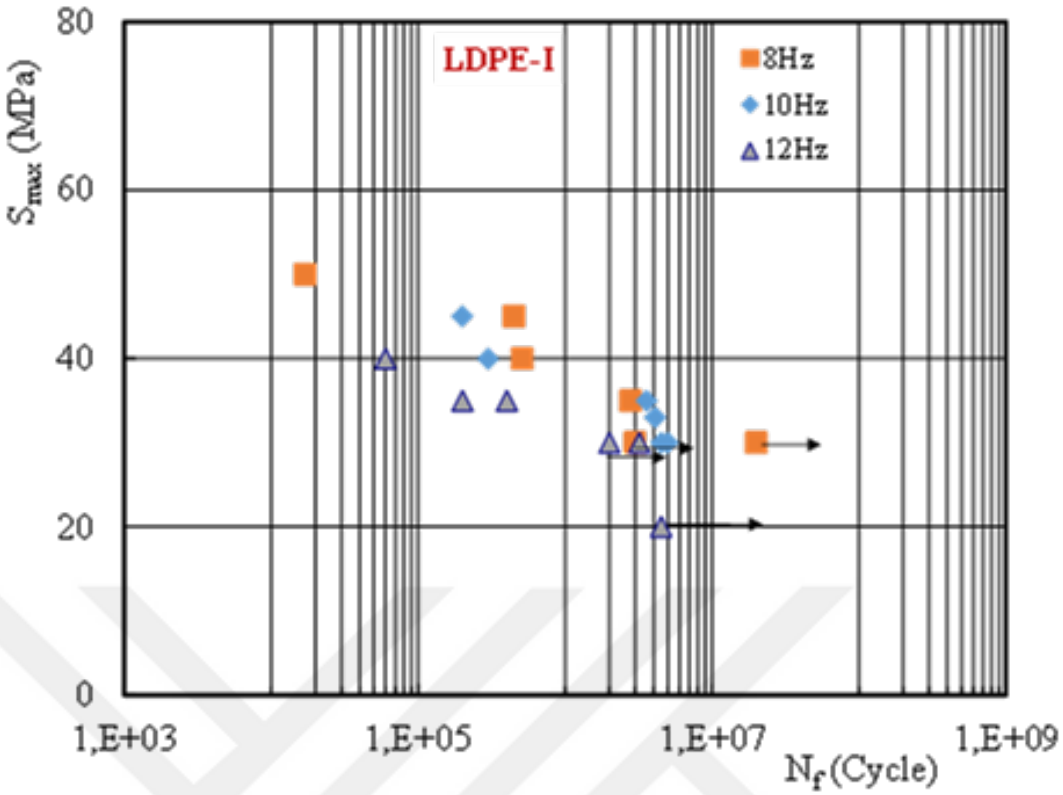

Figure 2.13: 3PB-Fatigue carried out under stress controlled at the three frequencies, 8, 10, 12 Hz for composite LDPE-I

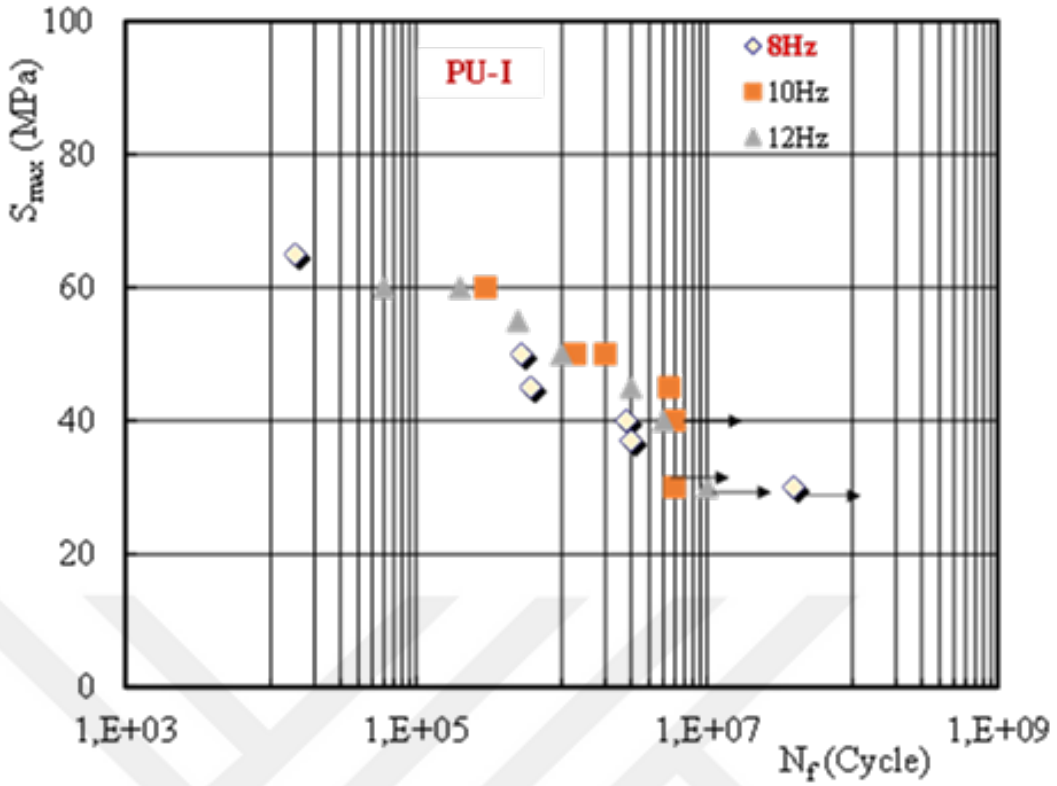

Figure 2.14: 3PB-Fatigue carried out under stress controlled at the three frequencies, 8, 10, 12 Hz for composite PU-I

2.1.4.6 Compression Test

To characterize the mechanical behavior of matrices and polymer-based composites, they undergo uniaxial compression tests following DIN 50106 standards at a constant crosshead speed of 1 mm/min. Figure 2.15 illustrates the test setup.

Figure 2.15: Uniaxial compression test setup

The stress-strain responses of the matrix and composite are presented in Figure 2.16. As depicted in this figure, the incorporation of fibers enhances the strength of the composite beyond that of the matrix, highlighting the positive impact of reinforcements. The summarized comparison of the test results can be found in Table 2.5.

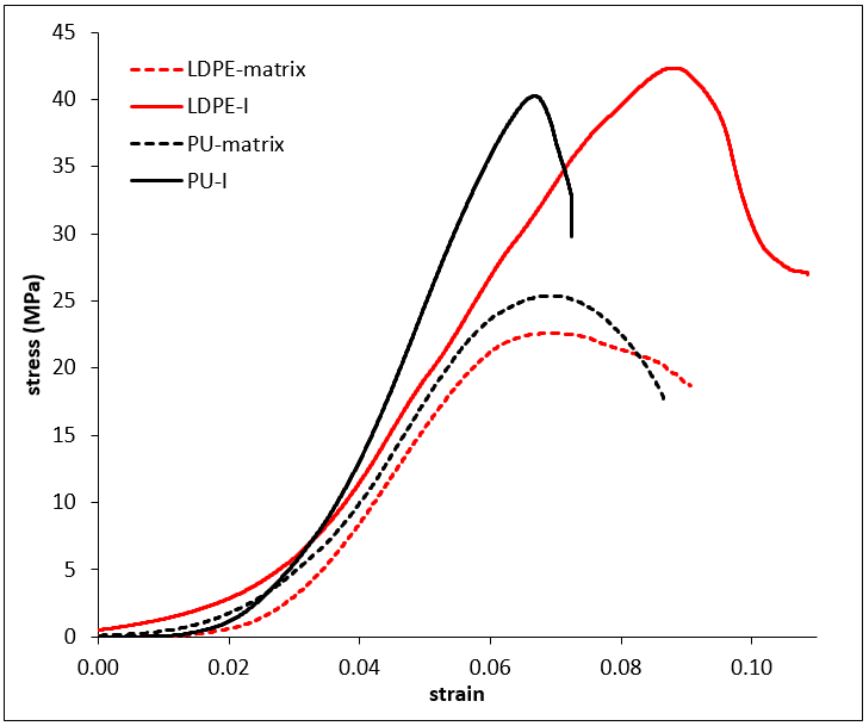

Figure 2.16: Uniaxial compressive responses of the matrices and the composites filled with CFs and GFs

Table 2.5: Comparison of the compression test results

Composite Name	Ultimate Stress (MPa)	Strain at Break ϵ_f (%)	Modulus of Elasticity E (MPa)
LDPE-matrix	22.59	9.64	639
LDPE-I	42.34	10.85	754
PU-matrix	25.38	8.65	409
PU-I	40.27	7.24	657

2.1.4.7 Microstructural Observations

Microstructure and surface damage evaluations were conducted using SEM, as shown in Figure 2.17. SEM observations were performed on the fracture surfaces of the tested specimens using an electron microscope. Interface analyses between matrix and reinforcement for each composite is carried out to optimize a strong adhesion structure of the composite for accomplished toughening mechanisms. Cavitation and void formation, along with matrix expansion, and local debonding of nanoparticles leading to void growth, are identified as enhanced toughening mechanisms in the structure. Microstructural analyses were also conducted on the polished surfaces of the specimens. This included mapping the distribution of particles and performing chemical analyses using EDS (Energy Dispersive X-ray Spectroscopy).

Figure 2.17: Scanning Electron Microscopy (SEM)

After the realization of mechanical tests, microstructure and fracture surface are analyzed for the distribution of the reinforcement in the matrix. The microstructures are evaluated with different reinforcements after sectioning and polishing. Energy Dispersive Spectroscopy (EDS) analyses is also used to control the chemical composition of the polymer-based composites. Microstructure and fracture surface of composites LDPE-I and PU-I are presented in Figures 2.18, 2.19, 2.20, 2.21, 2.22 and 2.23.

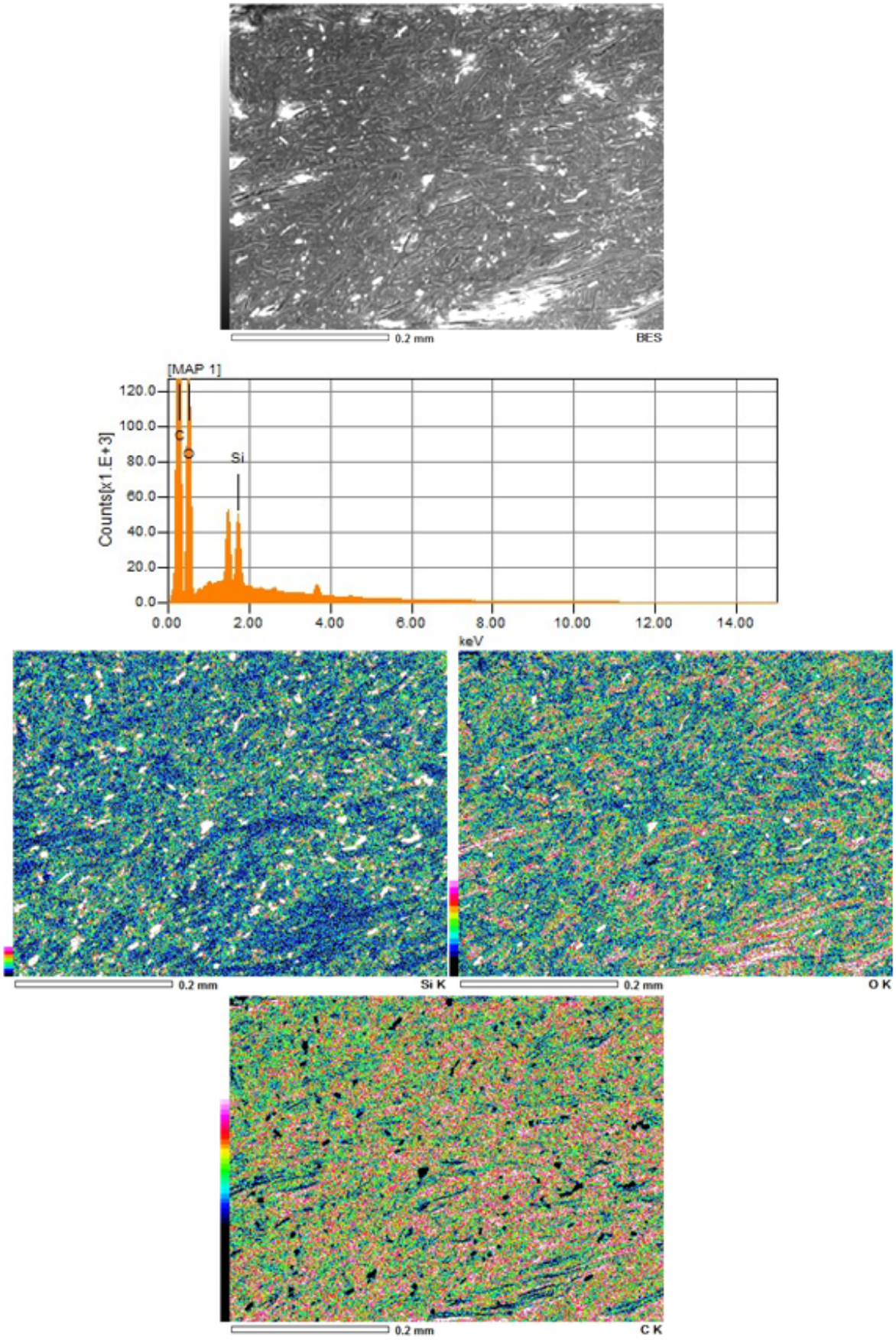

Figure 2.18: LDPE-I microstructure – mapping analyses

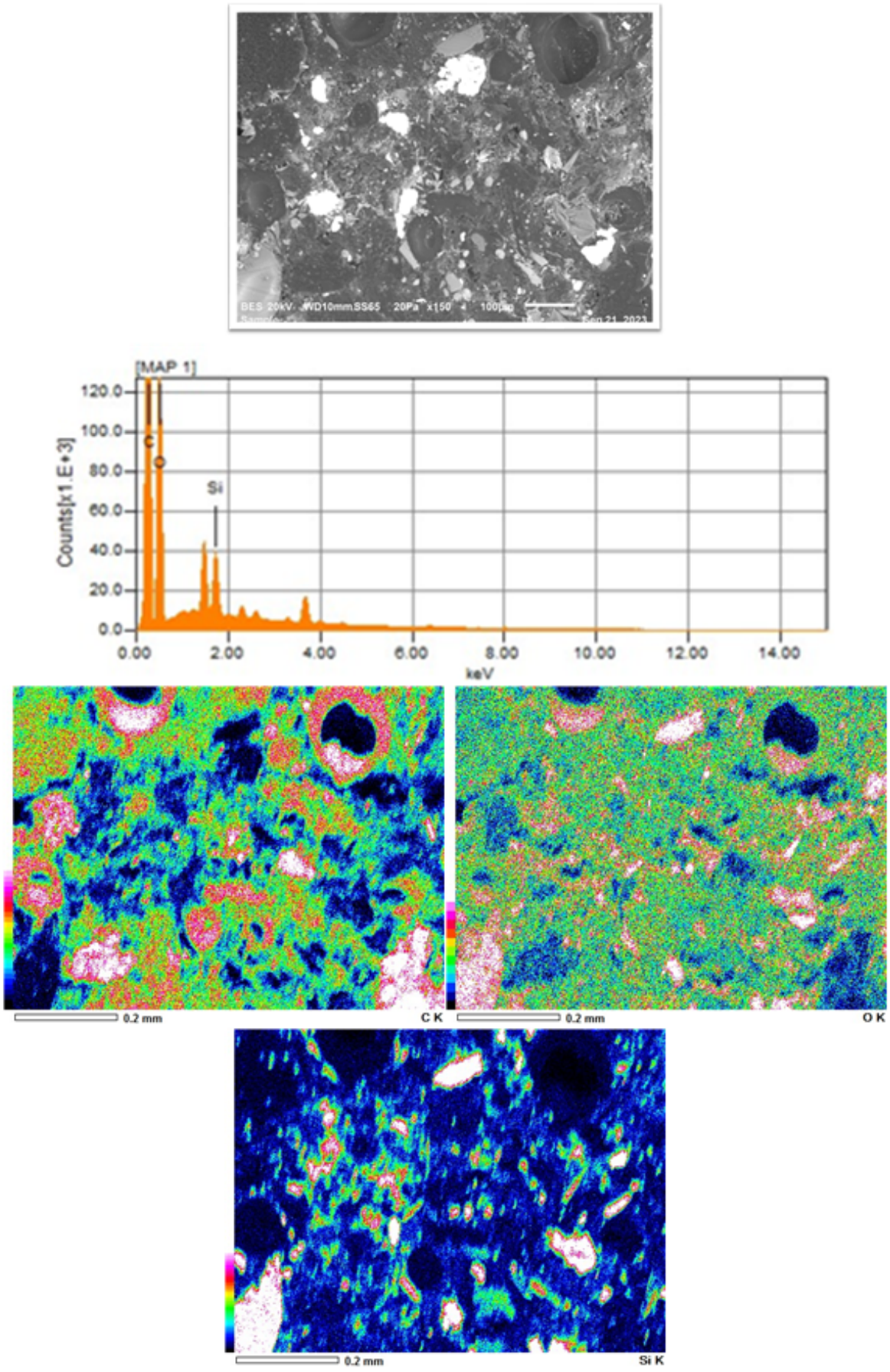

Figure 2.19: PU-I microstructure – mapping analyses

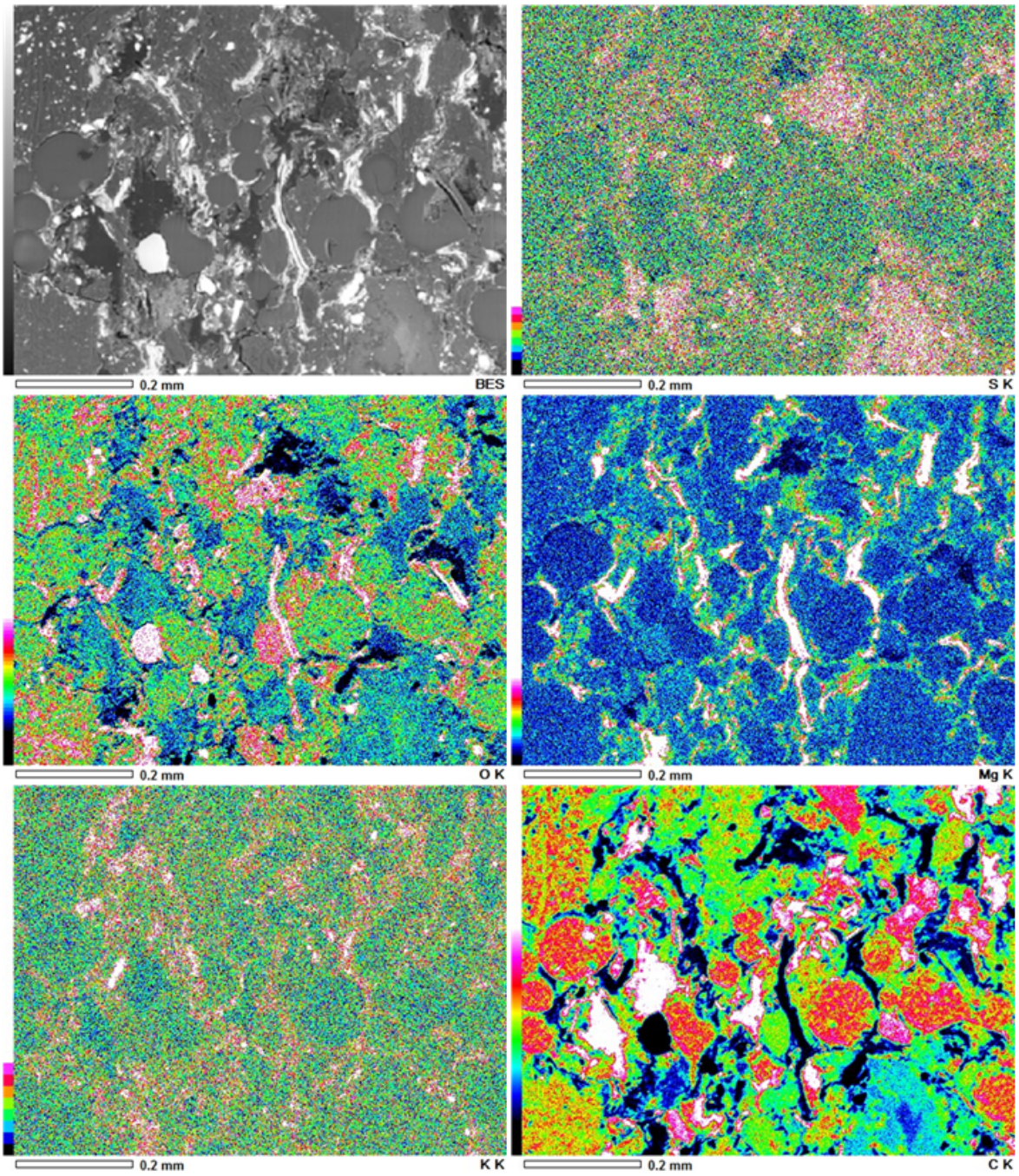

Figure 2.20: Energy Dispersive Spectroscopy (EDS) analyses for the composites

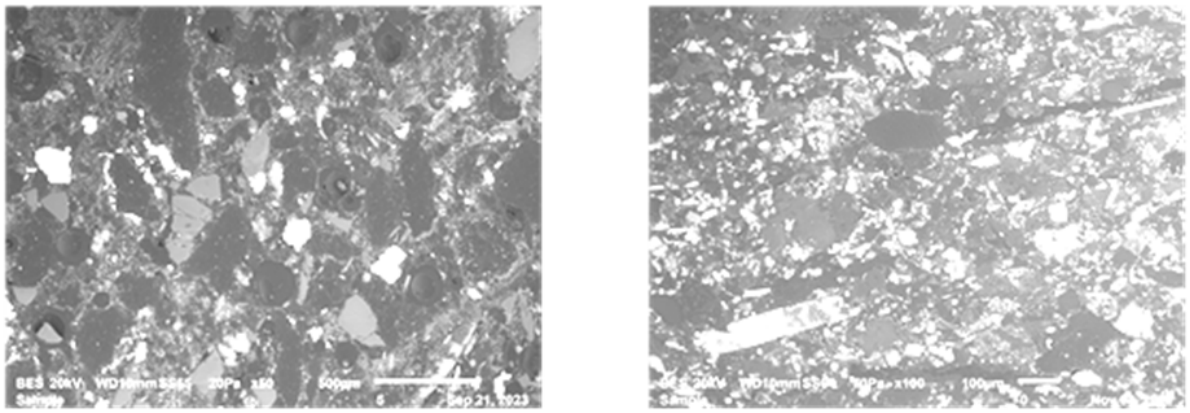

Figure 2.21: Microstructure analyses of LDPE-I (left) and PU-I (right)

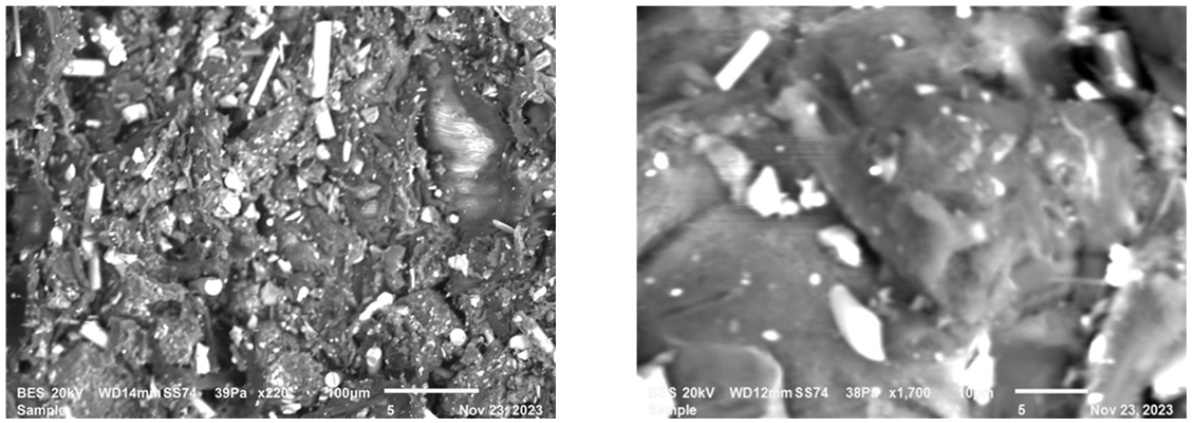

Figure 2.22: Fracture surface of LDPE-I

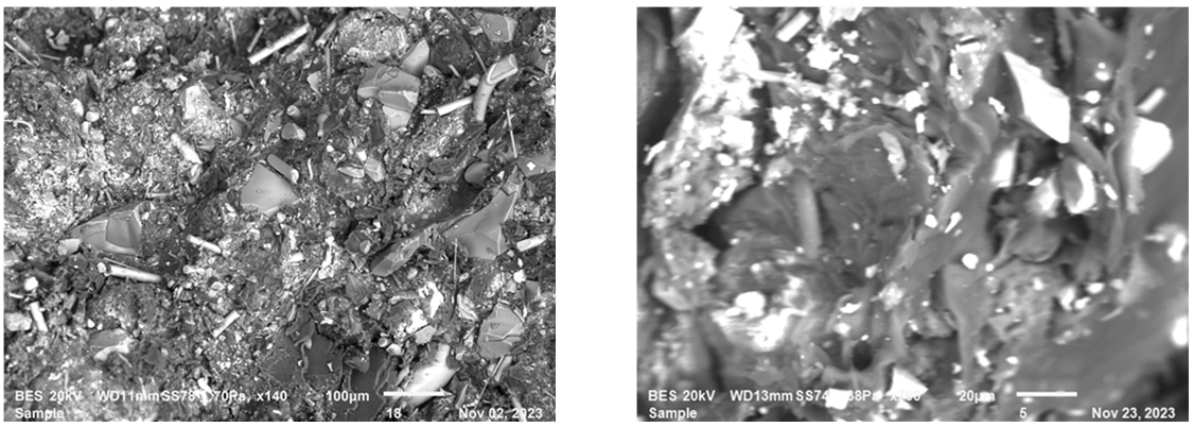

Figure 2.23: Fracture surface of PU-I

The matrix of the composites exhibits a generally uniform distribution of reinforcements throughout, although there are some minor clusters or agglomerations of the fine powders that serve as reinforcements. These clusters of particles may contribute to a decrease in the strain efficiency of the composites.

In the mapping images, a color legend is provided on the left-hand side, which shows the intensity of the identified elements. This legend is positioned at the bottom right corner of each image. The color scale progresses upwards to indicate higher intensities of the specified element. These visual representations clearly illustrate the homogeneous distribution of the reinforcement elements within the composite matrix.

2.2 Micromechanical Models

2.2.1 Analytical Homogenization

For polymer-based composites, accounting for the homogenization process is essential because the matrix and fillers exhibit distinct material properties. Understanding this process is key to accurately predicting the overall mechanical behavior of the composite material. There are several analytical models designed to estimate the theoretical modulus of such composites. One of the most widely used models is the Halpin–Tsai homogenization model. This model is particularly favored for its ability to estimate the homogenized moduli of heterogeneous materials with reasonable accuracy. The Halpin–Tsai model provides a mathematical approach to predict the elastic properties of composites based on various factors. These factors include the shape and orientation of the fillers, as well as the elastic properties of both the fillers and the matrix. The Halpin–Tsai model adapts well to composite materials, offering insights into how different components interact within the composite structure. By incorporating the geometry of the fillers (whether they are fibers, particles, or platelets) and their alignment within the matrix, the model can predict how these factors influence the overall stiffness and elasticity of the composite material.

The equation for the Halpin–Tsai model is formulated to consider these variables and provide a comprehensive understanding of the composite's mechanical behavior. Specifically, the model addresses the elastic modulus by integrating the contributions from both the fillers and the matrix, resulting in a homogenized modulus that reflects the combined characteristics of the composite.

The Halpin–Tsai model [26] is expressed as follows:

$$\frac{E_c}{E_m} = \frac{1 + \xi_f \eta V_f}{1 - \eta V_f}, \eta = \frac{\frac{E_f}{E_m} - 1}{\frac{E_f}{E_m} + \xi_f}, \xi_f = \frac{2L_f}{D_f} \tag{2.5}$$

where E_c, E_f and E_m represent the modulus of elasticity of the composite, fibers, and matrix, respectively. V_f denotes the volume fraction of the reinforcements, ξ_f is the shape or reinforcing factor that depends on the geometry of the filler, η is an

elastic modulus correction factor, and L_f and D_f are the length and diameter of the reinforcement particles, respectively.

The classical Halpin–Tsai (H-T) model is typically used for composites reinforced with a single scale of reinforcement. However, for predicting the elastic properties of composites that include rubber and reinforcement particles, a modified H-T model is applied. This modified model accounts for the effects of multiple scales of reinforcement. The equation for the macro reinforcements in the modified H-T model is given as follows:

$$E_c = \left[\frac{3}{8}\frac{1+\xi_f\eta_L V_f}{1-\eta_L V_f} + \frac{5}{8}\frac{1+2\eta_T V_f}{1-\eta_T V_f}\right] E_m, \eta_L = \frac{\frac{E_f}{E_m}-1}{\frac{E_f}{E_m}+\xi_f}, \eta_T = \frac{\frac{E_f}{E_m}-1}{\frac{E_f}{E_m}+2}, \xi_f = \frac{2L_f}{D_f} \quad (2.6)$$

In this context, L and T represent the longitudinal and transversal moduli, respectively, and are included in the calculation of ξ in formulation of η.

The modified Halpin–Tsai model is employed to estimate the elastic properties of the composite materials. This model takes into account the distinct characteristics of the matrix and various reinforcements to provide a comprehensive prediction of the composite's behavior.

To begin, the geometric and material properties, which are essential for the H-T model, are calculated. These properties are derived from the mass and volume of the manufactured specimens, including the polymer matrix, rubber, carbon fibers (CFs), and glass fibers (GFs). Detailed information on these calculated properties is provided in Table 2.6.

Table 2.6 includes data on the densities, moduli, and volume fractions of each component, along with their longitudinal and transversal moduli. This comprehensive set of data is crucial for accurately applying the modified H-T model, ensuring that all relevant factors influencing the composite's elastic properties are considered.

Table 2.6: Properties of materials used in the H-T calculations.

Material	Density (g/cm^3)	Modulus of elasticity, E (MPa)	Diameter (μm)	Length (μm)
LDPE	0.94	400	-	-
PU	1.20	600	-	-
Rubber	1.50	10	50	150
CF	2.00	2.88×10^5	10	50
GF	2.45	7.50×10^4	10	40

For the LDPE-I and PU-I composites, there are three different reinforcements: pure rubber, carbon fibers, and glass fibers. Therefore, the modified Halpin–Tsai (H-T) model must be applied in three steps to account for each type of reinforcement. The first step involves calculating the modulus of elasticity of the recycled rubber-polymer matrix using the modified H-T equations. This process is as follows:

$$E_{c1} = \left[\frac{3}{8}\frac{1+\xi_R\eta_L V_R}{1-\eta_L V_R} + \frac{5}{8}\frac{1+2\eta_T V_R}{1-\eta_T V_R}\right]E_P,\ \eta_L = \frac{\frac{E_R}{E_P}-1}{\frac{E_R}{E_P}+\xi_R},$$
$$\eta_T = \frac{\frac{E_R}{E_P}-1}{\frac{E_R}{E_P}+2},\ \xi_R = \frac{2L_R}{D_R} \tag{2.7}$$

where E_{c1} represents the modulus of elasticity of the new matrix, E_R denotes the modulus of elasticity of rubber, E_P signifies the modulus of elasticity of polymer. The parameters V_R, D_R, L_R, and ξ_R correspond to the volume fraction, diameter, length, and the shape factor of the rubber, respectively. With these values, the modulus of elasticity of the new matrix is determined. Subsequently, the same formula is applied to include carbon fibers in the matrix.

$$E_{c2} = \left[\frac{3}{8}\frac{1+\xi_{CF}\eta_L V_{CF}}{1-\eta_L V_{CF}} + \frac{5}{8}\frac{1+2\eta_T V_{CF}}{1-\eta_T V_{CF}}\right]E_{c1},\ \eta_L = \frac{\frac{E_{CF}}{E_{c1}}-1}{\frac{E_{CF}}{E_{c1}}+\xi_{CF}},$$
$$\eta_T = \frac{\frac{E_{CF}}{E_{c1}}-1}{\frac{E_{CF}}{E_{c1}}+2},\ \xi_{CF} = \frac{2L_{CF}}{D_{CF}} \tag{2.8}$$

in which E_{c2} the modulus of elasticity of the new composite, E_{CF} the modulus of

elasticity of carbon fibers, V_{CF}, D_{CF}, L_{CF}, and ξ_{CF} are the geometric properties of carbon fibers. Here, the volume fraction and the shape factor of fibers are 0.05 and 10, respectively. Finally, the modulus of elasticity of composite is obtained by adding glass fiber particles as

$$E_c = \left[\frac{3}{8}\frac{1+\xi_{AF}\eta_L V_{GF}}{1-\eta_L V_{GF}} + \frac{5}{8}\frac{1+2\eta_T V_{GF}}{1-\eta_T V_{GF}}\right] E_{c2},\ \eta_L = \frac{\frac{E_{GF}}{E_{c2}} - 1}{\frac{E_{GF}}{E_{c2}} + \xi_{GF}},$$
$$\eta_T = \frac{\frac{E_{GF}}{E_{c2}} - 1}{\frac{E_{GF}}{E_{c2}} + 2},\ \xi_{GF} = \frac{2L_{GF}}{D_{GF}} \tag{2.9}$$

where E_c the modulus of elasticity of final composite, E_{GF} the modulus of elasticity of the alumina fibers;, V_{GF}, D_{GF}, L_{GF}, and ξ_{GF} are the geometric properties of glass fiber particles. The volume fraction of glass fiber is 0.05 and the shape factor is 10. The same procedure is applied to composites LDPE-I and PU-I and homogenized elastic moduli are detailed in Table 2.7 alongside the experimentally derived values for comparison.

Table 2.7: Modulus of elasticity obtained by Halpin–Tsai Homogenization

Composite Name	Density (g/cm^3)	H-T Modulus E_c (MPa)	Experimental Modulus E (MPa)	Error (%)
LDPE-I	1.41	656	754	12.95
PU-I	1.59	560	657	14.77

While the elastic moduli calculated from the experimental data and the Halpin-Tsai model do not closely match, there is a noticeable similarity in the general trend of changes in elastic moduli based on the composition of the composites.

The discrepancy observed between the elastic moduli estimated from experimental data and those predicted by the H-T model underscores a notable divergence in quantitative accuracy. Despite this, both methods consistently indicate a trend where the elastic moduli increase with the addition of particles into the matrix. This trend highlights the reinforcing effect of fillers in enhancing the stiffness of the composites.

Analytical models such as the H-T model are constrained by their simplifications, which involve averaging the properties of filler and matrix materials and considering

geometric parameters like shape and volume fraction of inclusions. These simplifications, while providing a theoretical framework, may not fully capture the complex interactions and variations present in real-world composite materials.

Given the limitations of analytical approaches in accurately predicting complex material behaviors, numerical methods offer a more robust alternative. Numerical simulations can handle intricate geometries and nonlinear material responses, providing insights into composite performance with greater precision and reliability. Thus, for comprehensive analysis and design of composite materials, the use of numerical methods becomes imperative to ensure accurate characterization of their mechanical properties and behavior under various conditions.

2.2.2 Computational Homogenization

In various engineering disciplines, understanding the overall macroscopic properties of heterogeneous materials is crucial. However, conducting straightforward experimental observations across multiple material samples with varying phase characteristics, volume fractions, and loading conditions proves challenging due to time and cost constraints. Moreover, creating a finite element mesh that accurately represents microstructural details and allows for the numerical analysis of macroscopic structural behavior within a reasonable timeframe remains impractical due to significant length scale disparities.

To address these challenges, several homogenization techniques have been developed to establish effective constitutive models applicable at the macroscopic scale [25]. These methods aim to circumvent the complexities of microstructural variations by providing averaged material properties that reflect the behavior of the entire composite.

One effective approach involves employing numerical techniques and simulations on microstructural samples. Central to this method is the concept of Representative Volume Element (RVE), which plays a pivotal role in homogenization. The RVE is a volume of the material that is statistically representative of the composite's microstructure. By analyzing RVEs through numerical simulations, engineers can extrapolate

macroscopic material behaviors, making this approach indispensable in the study of heterogeneous materials.

Representative Volume Element (RVE) serves as a critical concept in the study of heterogeneous materials, defined as a volume V that effectively encapsulates the microstructural variability found within a composite material. This definition necessitates that the RVE encompasses a sufficient number and variety of microstructural features to provide a statistically representative sample of the entire composite.

To maintain applicability within continuum mechanics, the RVE must also be relatively small in comparison to the overall dimensions of the structure being analyzed. This ensures that the behaviors observed within the RVE can be extrapolated to describe the macroscopic mechanical properties of the material accurately.

In practical terms, different types of boundary conditions can be prescribed on the RVE to impose specific mean strain or stress states. It is crucial that the mechanical response of the RVE remains independent of the chosen boundary conditions, ensuring robustness and reliability in the characterization of material behavior [61].

Among the various boundary conditions used, periodic boundary conditions are particularly favored in RVE simulations. Studies have demonstrated that periodicity yields more realistic estimations of effective moduli compared to other boundary conditions like uniform displacement or uniform traction. This preference arises from the ability of periodic boundary conditions to better capture the repetitive nature of microstructures within the composite, thereby enhancing the accuracy of macroscopic predictions derived from RVE analyses.

Periodic boundary conditions in the context of RVEs dictate that the shape and orientation of opposite edges remain unchanged throughout the deformation process. This ensures that stress continuity is maintained across these boundaries, with stress vectors on opposite sides acting in opposite directions [25].

Various studies have sought to define the Representative Volume Element (RVE) for different applications and purposes. Gitman's review highlights the diverse efforts and methodologies employed in this field [62].

- RVE must encompass enough microstructural details [63].
- It should be much smaller than the macroscopic structural dimensions but sufficiently larger than the microstructural features [64].
- RVE should contain a substantial number of micro-heterogeneities, including inclusions, grains, voids, and fibers [44].
- Statistical homogeneity and ergodicity are necessary for RVE to accurately represent the macro response [65].
- RVE's response must be consistent regardless of the boundary conditions applied [66].
- The size of RVE is determined based on specific effective properties and the volume fraction of micro-heterogeneities [61, 62, 67].

The numerical approach begins with the creation of candidate Representative Volume Elements (RVEs), achieved using a Python script written for ABAQUS/CAE. This script automates the generation of reinforcements based on a specified volume ratio, ensuring consistent and accurate RVE creation. The second phase involves applying periodic boundary conditions to the RVEs and conducting numerical simulations to replicate basic laboratory tests. These tests, with known macroscopic responses and boundary conditions, provide a benchmark for validating the simulations. The third major step in the numerical analysis is performing homogenization procedure for Finite Element Analysis (FEA). This step involves a detailed comparison between the experimentally obtained mechanical characteristics and the results from the homogenization model. The aim is to ensure that the numerical model accurately reflects the physical behavior of the composites, thereby validating the simulation approach. In the final step, a material model for the polymer matrix is developed and implemented into a user-defined material subroutine (UMAT) for ABAQUS. This subroutine allows for detailed simulation of the material's behavior under various loading conditions, integrating the homogenized properties and ensuring accurate predictions of the composite's performance. This comprehensive approach ensures that the numerical model is robust, validated, and capable of accurately predicting the behavior

of polymer-based composites under different conditions. It thus provides a powerful tool for designing and analyzing advanced composite materials.

The uniaxial response of polymer-based composites, filled with recycled rubber (RR), carbon fibers (CFs), and glass fibers (GFs), as well as the influence of these fillers on the finite strain behavior of the composites, is thoroughly examined through macromechanical finite element simulations using ABAQUS/Standard. A detailed 2D finite element model is developed to accurately represent the dimensions of the test specimens, aiming to replicate the stress-strain response of the composite materials. These simulations focus specifically on uniaxial compressive tests for LDPE-I and PU-I composites. The 2D macrostructure of these composites is defined by a matrix embedded with randomly dispersed particles, simulating the real-life dispersion of fillers within the polymer matrix.

To achieve a realistic randomization of the inclusions within the matrix geometry, a Python script is meticulously crafted. This script automates the placement of inclusions, ensuring that the generated model in ABAQUS/CAE accurately represents the heterogeneous nature of the composite material. This methodological approach allows for precise simulations that closely mimic the physical behavior observed in experimental tests. By utilizing these advanced simulation techniques, the study provides valuable insights into the mechanical performance and finite strain behavior of the polymer-based composites. The results obtained from these simulations are critical for understanding how the incorporation of recycled rubber, carbon fibers, and glass fibers affects the overall mechanical properties of the composites, ultimately aiding in the development of more robust and efficient composite materials.

Initially, a fiber particle is generated within the rectangular representation of the matrix by defining a "random" function within the Python script. To ensure proper placement and avoid any overlap, an algorithm is implemented that checks for intersections between newly created fibers and previously generated fibers or matrix boundaries. This algorithm also calculates the minimum allowable distance between each inclusion to maintain spatial uniformity. At each iteration, the cumulative volume ratio is recalculated to keep track of the total volume occupied by the fibers. The process continues, drawing and placing fibers while continually checking and adjusting for

overlap and spacing, until the desired total volume ratio of inclusions within the matrix is achieved. This approach ensures a random yet evenly distributed arrangement of fibers, providing a realistic model for finite element analysis in ABAQUS/CAE.

By adhering to these detailed steps, the script accurately replicates the random distribution of fibers in a composite material, allowing for precise simulation and analysis of the composite's mechanical behavior under various loading conditions.

However, accurately modeling each composite with the actual specimen size necessitates the use of a vast number of random particles, making it time-consuming and involves an extensive number of elements, making the analysis challenging to converge. For example, a model for the LDPE-I test specimen with dimensions 24×30.75 mm requires a matrix filled with $147,600$ randomly dispersed particles. To address this, the model area is reduced to be 14 times smaller than the actual specimen, and numerous simulations with varying random inclusions are performed to verify result reproducibility.

The uniaxial compressive tests are simulated for a 2D macrostructure with dimensions 10×5 mm, defined by a matrix filled with $10,000$ randomly distributed rectangular particles, representing 10% by volume of the test specimen. Once the model is created, $817,108$ linear 3-node triangular elements are used for the matrix and inclusions, with an approximate element size of 0.05 mm. Static uniform boundary conditions (SUBC) are then applied to the model, with a maximum displacement of 1.1 mm in the uniaxial direction. Figure 2.24 depicts the macromechanical finite element model of the composites. By scaling down the model size and using a substantial number of elements, the simulations provide a reliable representation of the composite behavior, allowing for a detailed analysis of the mechanical properties and ensuring the results are consistent and reproducible.

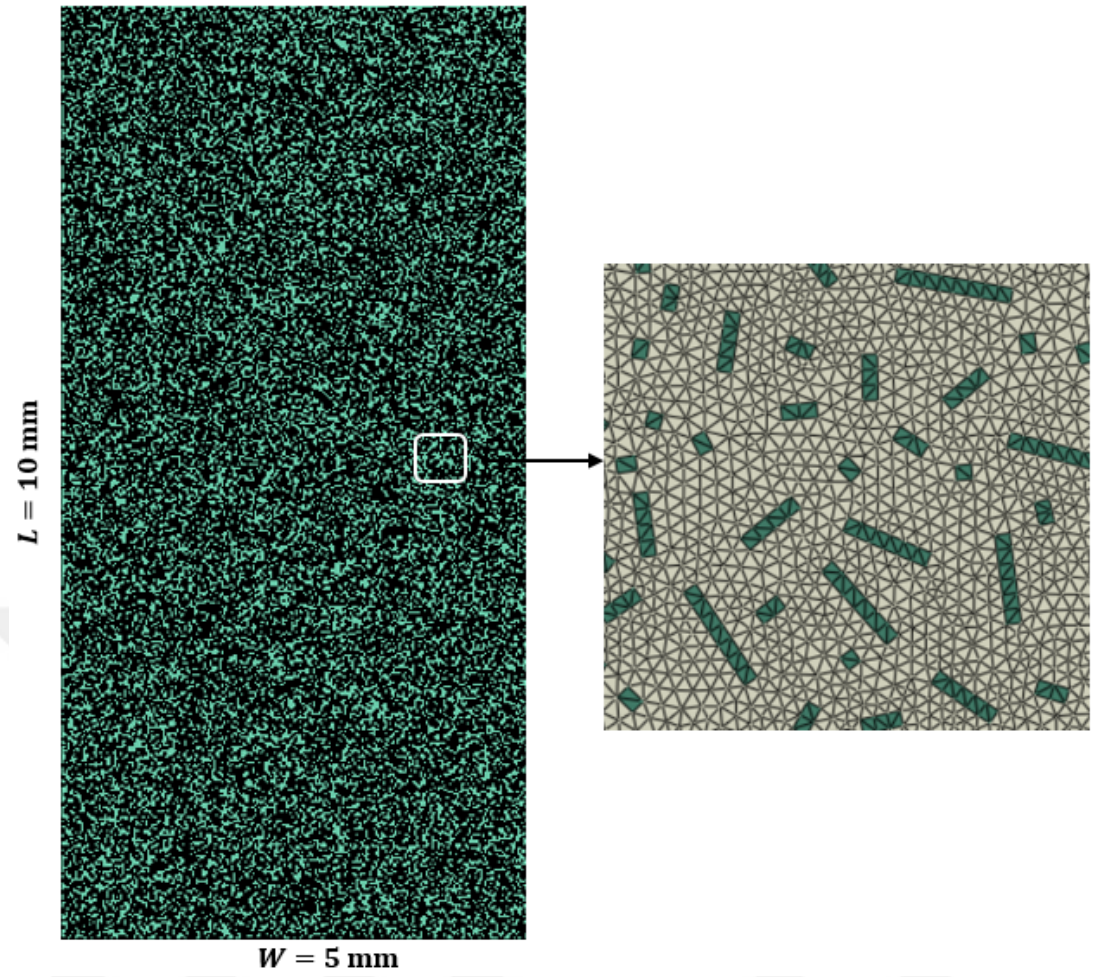

Figure 2.24: Macromechanical finite element model of the polymer-based composite filled with 5% CFs and 5% GFs

In this study, the mechanical behavior of carbon fibers (CFs) and glass fibers (GFs) is pivotal due to their significantly higher stiffness compared to the polymer matrix they reinforce. Carbon fibers exhibit an elastic modulus of 2.88×10^5 MPa with a Poisson's ratio of 0.3, making them ideal for applications requiring lightweight, high-strength materials. On the other hand, glass fibers have an elastic modulus of 7.50×10^4 MPa, also with a Poisson's ratio of 0.3, offering good strength and moderate stiffness, suitable for applications where cost-effectiveness and durability are paramount. These mechanical characteristics of the fibers influence how they interact with the matrix, affecting the overall stiffness, strength, and impact resistance of the composite materials you are investigating.

In Figure 2.16, it is evident that the composite material exhibits significantly higher strength compared to the matrix alone, showcasing the pronounced effect of reinforcement. The mechanical properties of the composite are notably enhanced due to the addition of reinforcements such as carbon fibers (CFs) and glass fibers (GFs). This enhancement is reflected in the material's response under load: the stress-strain curve shows a nonlinear behavior typical of composite materials, where the stiffness varies with increasing deformation.

Moreover, the plastic response of the composite materials demonstrates a softening behavior as it approaches failure. This ductile response indicates that the composites can withstand considerable deformation before eventual fracture, which is crucial in applications where toughness and resilience are paramount. Overall, these findings underscore the effective role of reinforcements in improving both the strength and ductility of polymer-based composites, making them suitable for demanding engineering applications where robustness and reliability are required.

Damage initiation in ductile materials, including composites, involves complex interactions between stress conditions, strain rates, and material microstructure. In the case of composites, where the matrix and reinforcements differ significantly in mechanical properties, understanding these initiation mechanisms is crucial for predicting failure.

When a composite undergoes loading, stresses concentrate around imperfections such as voids between the matrix and reinforcing fibers. These voids are much smaller than the dimensions of the reinforcing fibers but can significantly influence the material's

overall strength and failure behavior.

Ductile damage initiation criteria aim to predict the point at which these voids initiate fracture. This criterion typically considers the equivalent plastic strain, $\bar{\epsilon}_D^{pl}$, which is a measure of localized plastic deformation, influenced by stress triaxiality (η) and strain rate ($\dot{\bar{\epsilon}}^{pl}$). Stress triaxiality ($\eta$) is defined as the ratio of pressure stress (p) to the Mises equivalent stress (q), capturing the state of stress within the material.

For predicting damage initiation, the criterion states that damage begins when the equivalent plastic strain, $\bar{\epsilon}_D^{pl}$, reaches a critical value determined by stress triaxiality and strain rate conditions. Damage initiation occurs when the following condition is fulfilled:

$$\omega_D = \int \frac{d\bar{\epsilon}^{pl}}{\bar{\epsilon}_D^{pl}(\eta, \dot{\bar{\epsilon}}^{pl})} = 1 \tag{2.10}$$

where ω_D is a state variable that increases monotonically with plastic deformation. At each increment during the analysis the incremental increase in ω_D is computed as

$$\Delta\omega_D = \frac{\Delta d\bar{\epsilon}^{pl}}{\bar{\epsilon}_D^{pl}(\eta, \dot{\bar{\epsilon}}^{pl})} \geq 0 \tag{2.11}$$

This critical value varies based on material properties and loading conditions, influencing how void growth and subsequent failure mechanisms evolve during mechanical loading of the composite.

In summary, the ductile damage initiation criterion provides a framework for understanding how voids initiate fracture in composites, offering insights into their mechanical behavior under different loading conditions and aiding in the development of robust predictive models for composite performance and durability.

To evaluate the damage properties and strain-softening response of the composites, a detailed analysis of the materials' behavior is performed by examining the displacement and strain measurements obtained from experimental studies. This analysis helps construct the strain-softening response, which characterizes how the material undergoes progressive deformation and damage under loading conditions.

In order to simulate these behaviors numerically, finite element analysis is conducted using ABAQUS software. The results from these simulations provide insights into the strain distribution and evolution within the composites, specifically in the axial direction. These results are crucial for understanding how the composites respond to mechanical loads and for predicting their failure mechanisms.

Figure 2.25 displays the strain distribution in the axial direction, highlighting areas of strain concentration and potential failure points. The accuracy of the numerical model is validated by comparing its results with experimental data, ensuring that the simulations realistically represent the physical behavior of the composites.

Additionally, Figures 2.26 and 2.27 compare the numerical macroscopic response of the polymer-based reinforced composites with the corresponding experimental results. These comparisons demonstrate the ability of the numerical model to capture the complex interactions between the matrix and the reinforcements, such as recycled rubber (RR), carbon fibers (CFs), and glass fibers (GFs). The close agreement between the simulated and experimental stress-strain curves indicates the robustness of the model in predicting the mechanical performance of the composites.

The insights gained from these analyses are valuable for optimizing composite design and improving material properties. By understanding the strain-softening behavior and damage initiation mechanisms, engineers can develop composites with enhanced durability and performance, tailored for specific applications in various industries.

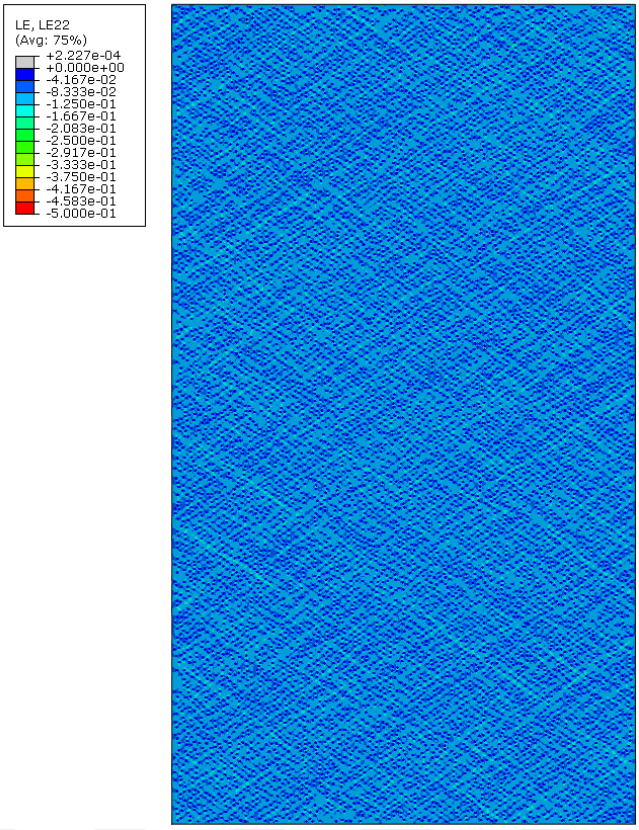

Figure 2.25: Deformed geometry of macromechanical finite element model of polymer-based reinforced composite

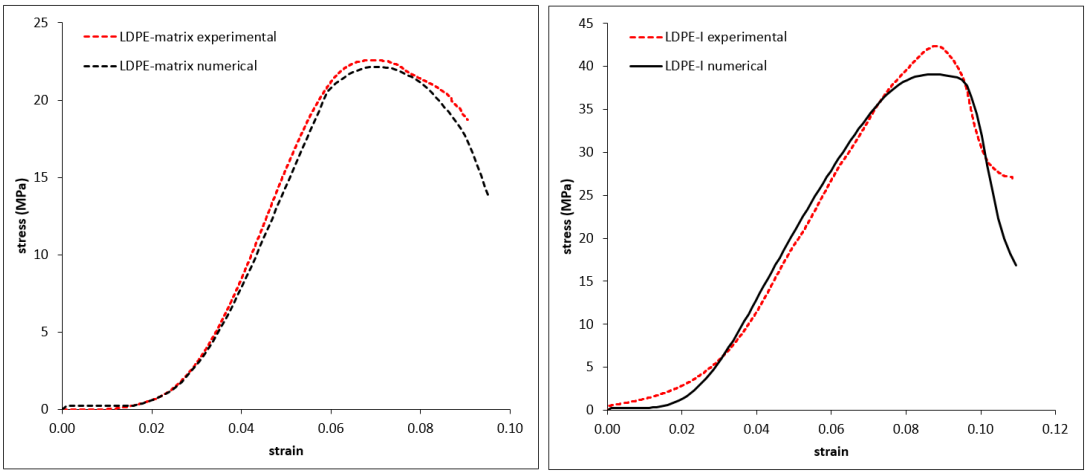

Figure 2.26: Comparison of the experimental and numerical results of LDPE matrix (left) and composite LDPE-I (right)

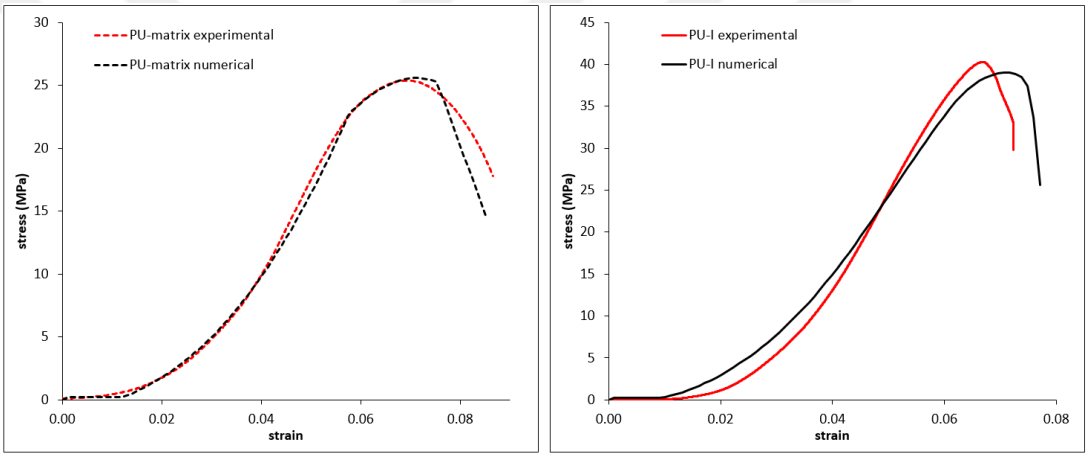

Figure 2.27: Comparison of the experimental and numerical results of PU matrix (left) and composite PU-I (right)

In Figures 2.26 and 2.27, the left side showcases the results for matrices, while the right side presents the data for the composites. For the matrix, the experimental data reveals its inherent mechanical properties, providing a baseline for evaluating the effects of reinforcement. The numerical simulation for the matrix aims to replicate these properties accurately, capturing the stress-strain response and validating the finite element model's accuracy. By ensuring a close match between the experimental and numerical results, confidence is established in the model's ability to predict the behavior of the matrix material under various loading conditions. On the other hand, the composite, which includes reinforcements such as recycled rubber (RR), carbon fibers (CFs), and glass fibers (GFs), exhibits enhanced mechanical properties compared to the pure matrix. The right side of the comparison illustrates how these reinforcements influence the composite's overall strength and deformation characteristics. The experimental results for LDPE-I show a significant improvement in stiffness and load-bearing capacity due to the presence of the reinforcements.

Both comparisons highlight the importance of numerical modeling in understanding and predicting the mechanical performance of polymer-based composites. The agreement between experimental and numerical results demonstrates the model's effectiveness in simulating real-world conditions, providing valuable insights for optimizing composite design and improving material properties. This comparison underscores the role of finite element analysis as a powerful tool for advancing the development of high-performance composite materials tailored for specific applications.

Modeling microstructures using a Representative Volume Element (RVE) is fundamental for addressing homogenization problems in composite materials. The RVE must contain a sufficient number of microstructural heterogeneities to be statistically representative of the material, while being small enough to function as a continuum mechanics volume element. The principle behind RVE modeling is that its behavior should not depend on the type of boundary conditions applied [61], [66].

Periodicity conditions are frequently imposed on the RVE because they yield accurate estimations of the effective moduli of the composite material. This involves ensuring that the deformations on opposing edges of the RVE are identical, maintaining the geometric and stress continuity across the boundaries [25]. This method captures the

true nature of the material's response under various loading conditions.

In computational micromechanics, the implementation of periodic boundary conditions (PBCs) is crucial. These conditions require that the shape and orientation of opposite edges of the RVE remain the same throughout the deformation process. Additionally, for stress continuity, the stress vectors on opposing sides must be equal in magnitude but opposite in direction. This ensures that the simulation accurately reflects the behavior of the entire material, not just the RVE itself.

PBCs are favored because they provide a more accurate and realistic representation of the material's behavior compared to other boundary conditions. They help in achieving a consistent and reliable estimation of the material properties, which is essential for the design and analysis of composite materials. By maintaining the periodicity and stress continuity, PBCs enable a comprehensive understanding of how the microstructure influences the macroscopic properties of the composite, facilitating better predictions and optimizations in material engineering.

A 2D RVE is employed for homogenization, containing randomly positioned inclusions. To enforce PBCs on the RVE, a periodic geometry and mesh are necessary. Using a Python script, the inclusions are randomized within a square with periodic boundaries. A volume element V is defined, and PBCs are applied at its boundary δV to assess its overall properties. This script is provided in Appendix A.

The displacement field across the volume V ensures that displacements on opposite edges of the RVE are consistent to maintain its periodic nature. This approach enables simulation of material behavior under varying loads while preserving the periodic microstructure. The displacement field over the entire volume is formulated as:

$$\mathbf{u} = \mathbf{E}.\mathbf{x} + \boldsymbol{\nu} \quad \forall \mathbf{x} \in V \tag{2.12}$$

Here, $\mathbf{E}$ represents the macroscopic strain tensor, $\mathbf{x}$ is the position vector, and $\boldsymbol{\nu}$ denotes periodic displacement fluctuations with zero mean over the RVE. Then, in indicial notation,

$$u_i = \epsilon^0_{ij} x_j + \nu_i \tag{2.13}$$

Here, the prescribed displacement u_i at position x on the boundary surfaces x_j is defined relative to a reference point. ϵ^0_{ij} represents the average strain applied to the RVE, and ν_i denotes the periodic fluctuation that maintains identical values at corresponding points on opposite faces. This ensures that the displacements across pairs of parallel opposite boundary surfaces

$$u_i^{k^+} = \epsilon^0_{ij} x_j^{k+} + \nu_i \tag{2.14}$$

$$u_i^{k^-} = \epsilon^0_{ij} x_j^{k-} + \nu_i \tag{2.15}$$

k^+ and k^- denote the k^{th} pair of parallel boundary surfaces facing each other. The fluctuation ν_i maintains identical values across these parallel boundaries, ensuring periodicity,

$$u_i^{k^+} - u_i^{k^-} = \epsilon^0_{ij}(x_j^{k^+} - x_j^{k^-}) = \epsilon^0_{ij} \Delta x_j^k \tag{2.16}$$

An illustration of a randomly distributed inclusion-matrix RVE is shown in Figure 2.28, using CPS4R element type (4-node bilinear plane stress quadrilateral, reduced integration, hourglass control), with a volume fraction of inclusions (V_f) set at 10% and an inclusion length (L) of 206 μm. Equations 2.17 and 2.18 corresponding to Equation 2.16 are provided to describe this configuration.

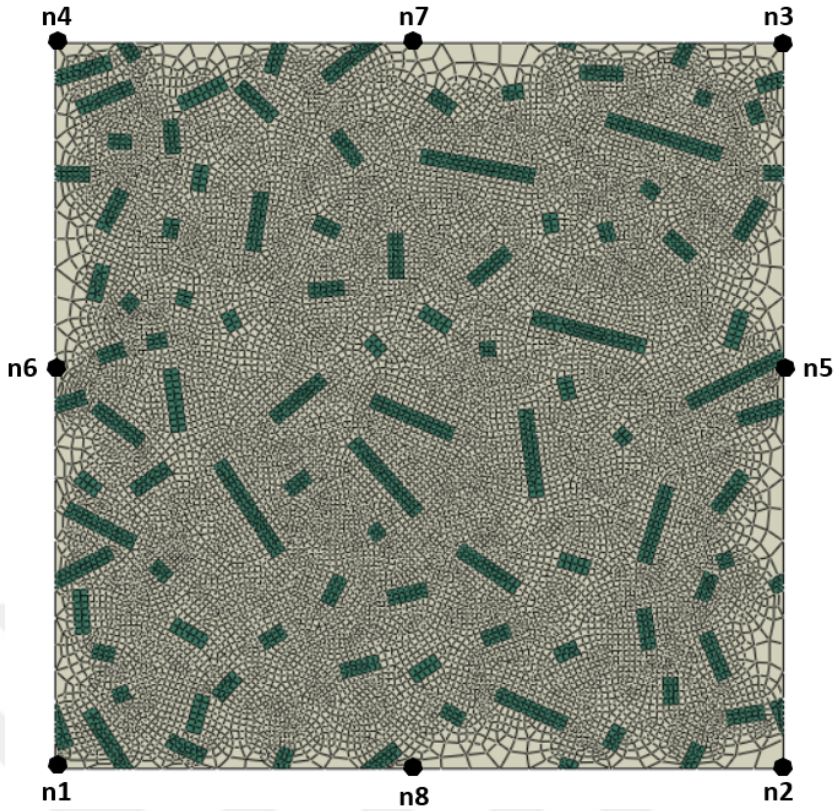

Figure 2.28: Paired nodes of RVE in two opposite parallel boundary surfaces

PBCs can be defined for this RVE by

$$u_{x,y}^{n5} - u_{x,y}^{n6} - u_{x,y}^{n2} + u_{x,y}^{n1} = 0 \tag{2.17}$$

$$u_{x,y}^{n7} - u_{x,y}^{n8} - u_{x,y}^{n4} + u_{x,y}^{n1} = 0. \tag{2.18}$$

Compression test results are replicated using distance-controlled PBCs with a total volume fraction $V_f = 0.10$. The maximum strain is derived from compression tests for various RVE lengths, and displacements are recorded at paired nodes connected within the RVE.

To determine the optimal RVE size, multiple randomizations of the composites are conducted with varying RVE lengths (see Figure 2.29).

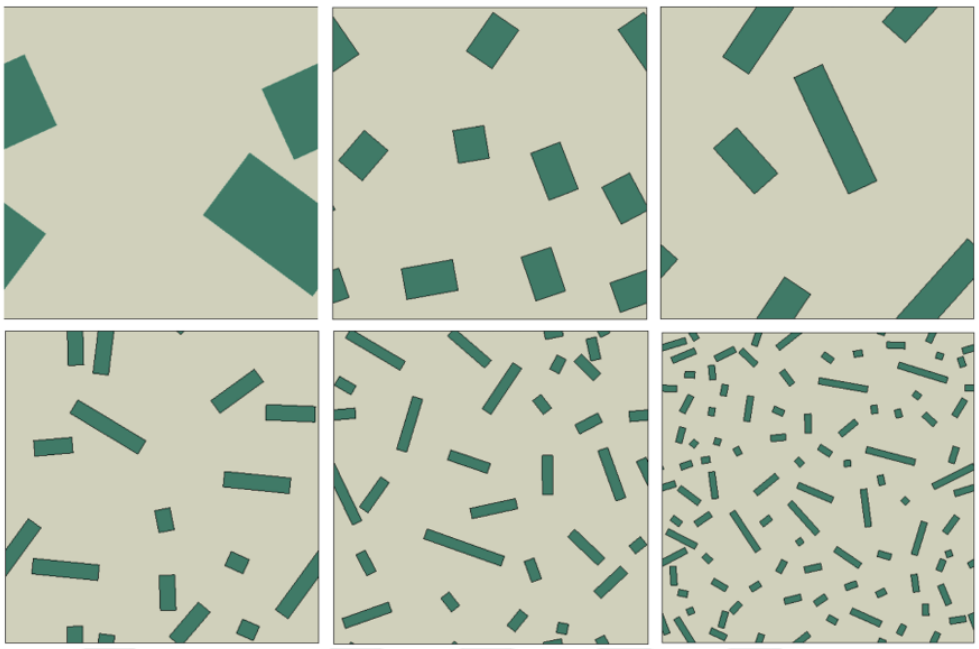

Figure 2.29: Randomization of RVE with different lengths

Table 2.8 shows the count of randomly placed inclusions corresponding to different sizes of the volume element used for determining the RVE dimensions.

Table 2.8: The length of RVE with the number of randomized AFs

volume fraction, V_f (%)	RVE size, L (μm)	# of inclusions, N
10	100	2
10	141	4
10	200	8
10	283	16
10	400	32
10	566	64
10	800	128

The application of periodic boundary conditions is depicted in Figure 2.30 for a two-dimensional RVE with a volume fraction of $V_f = 0.10$. As illustrated, carbon fibers (CFs) and glass fibers (GFs) that span the boundary surfaces are sectioned and translated to the corresponding opposite sides to preserve periodicity.

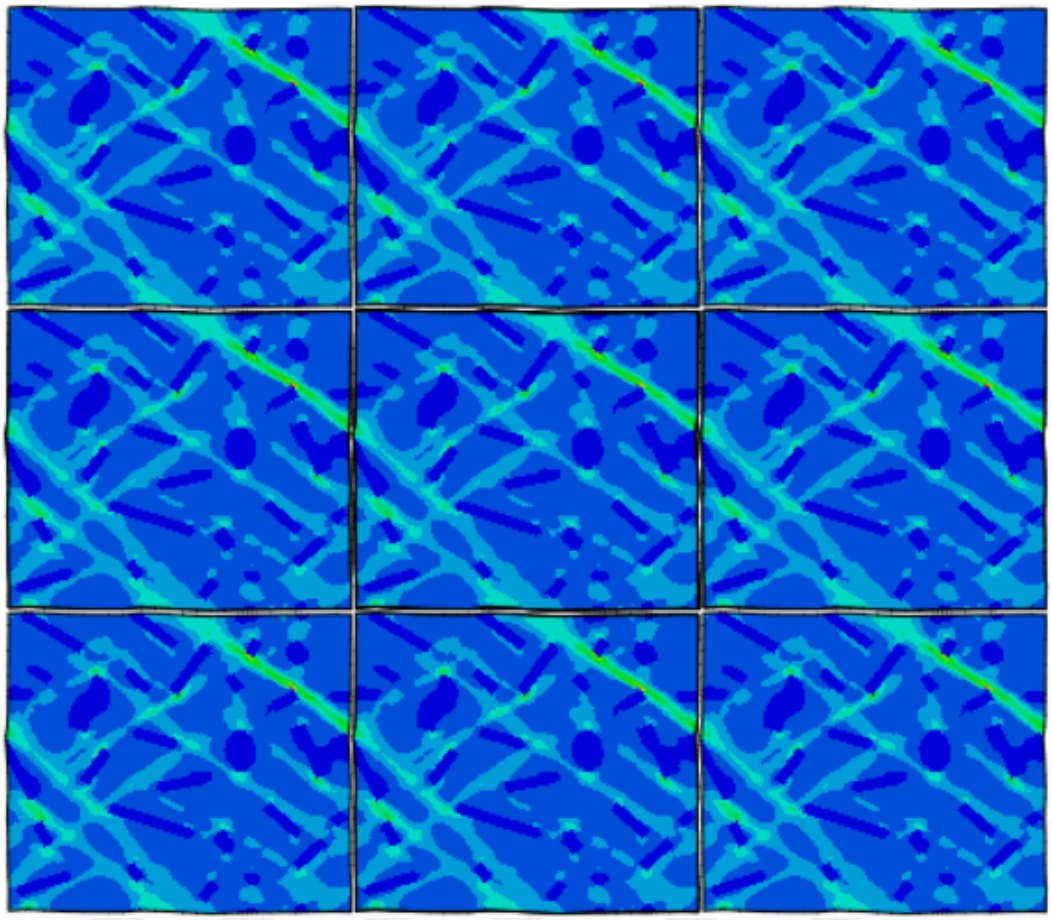

Figure 2.30: Implementation of PBCs to RVE $L = 150\ \mu$m ($V_f = 0.10$)

Kanit et al. [61] demonstrate that the constitutive behavior of random heterogeneous materials can be effectively derived for large volumes using only a few realizations. This means that it is possible to accurately determine the material properties by analyzing a limited number of samples for extensive volumes. As a primary objective, a 2D model with the actual dimensions of the specimen has been analyzed using a limited number of these realizations.

The macroscopic stresses and strains, which characterize the mechanical properties at the macroscopic level, can be interpreted as volumetric averages of microscopic fields within a specified volume, as noted by Vignoli and Savi [68]. To achieve macroscopic homogeneity, it is assumed that the strain and stress averages are independent of spatial variations. This assumption allows the integral over a certain region, divided by its volume, to represent these averaged quantities.

More precisely, if the position vector is denoted as $\mathbf{x}$, the volume-averaged stresses and strains, represented by square brackets, are defined as the mean values of point stress or strain over the entire volume V. These relationships are formalized in the following expressions, as established in the works of Hashin [69] and Kanit et al. [61], providing a rigorous framework for understanding and calculating the averaged mechanical properties of heterogeneous materials.

$$\mathbf{E} = \langle \boldsymbol{\epsilon} \rangle = \frac{1}{V} \int_V \boldsymbol{\epsilon} dV \tag{2.19}$$

where $\mathbf{E}$ represents a symmetric second-rank tensor. Consequently, the macroscopic stress tensor:

$$\boldsymbol{\Sigma} = \langle \boldsymbol{\sigma} \rangle = \frac{1}{V} \int_V \boldsymbol{\sigma} dV. \tag{2.20}$$

By using Equations 2.19 and 2.20, a Python script is meticulously developed to facilitate volume integration, which is crucial for evaluating the average stress and strain values across each integration point for every frame of the simulation (see Appendix B). This process is essential for accurately capturing the mechanical behavior of the heterogeneous composite material.

The script operates by first discretizing the composite's volume V into a finite number of elements. Each integration point within these elements is then used to calculate the local stress and strain values during the simulation. By performing volume integration, the script aggregates these local values to determine the overall, or macroscopic, stress and strain responses of the composite material.

This method ensures that the numerical response of the heterogeneous composite is obtained with high precision, reflecting the true mechanical properties and behavior of the material under various loading conditions. The integration results are crucial for validating the composite's performance and for comparing with experimental data to ensure the reliability of the simulation.

By utilizing this approach, the variations within the composite material are accurately captured, providing a comprehensive understanding of its mechanical properties. This enables engineers and researchers to predict the composite's behavior under different scenarios, thereby aiding in the design and optimization of advanced composite materials.

The primary concept behind the overall average homogenization approaches is that specific fourth-order concentration tensors can be employed to link the volume-averaged strains and stresses to each other or to the overall boundary conditions. These tensors act as bridge elements, translating localized microscopic behaviors into macroscopic properties that can be observed and measured.

Establishing the average stress or strain concentration tensor is crucial for relating the average stress or strain within the inclusion to globally applied boundary conditions. The stress or strain concentration tensor effectively captures how the material's microstructural heterogeneities influence the macroscopic response. This is particularly important in composite materials, where differences in the mechanical properties of the matrix and reinforcements lead to complex stress and strain distributions.

The relationship between the average strains within the inclusion, the overall macroscopic strains, and the averaged strains across the matrix is defined by a fourth-order strain concentration tensor field $\mathbb{A}$ [61].

$$\boldsymbol{\epsilon}(\mathbf{x}) = \mathbb{A}(\mathbf{x}) : \mathbf{E} \tag{2.21}$$

a four-rank concentration tensor field $\mathbb{B}$ for SUBC problem

$$\boldsymbol{\sigma}(\mathbf{x}) = \mathbb{B}(\mathbf{x}) : \boldsymbol{\Sigma} \tag{2.22}$$

This tensor field plays a critical role in periodic boundary condition (PBC) problems, ensuring that the microscopic response within the inclusions and matrix can be accurately upscaled to predict the macroscopic behavior of the composite material.

In practical terms, the strain concentration tensor $\mathbb{A}$ allows for the calculation of effective material properties by averaging the local strains in the inclusions and matrix. This averaging process takes into account the geometry, distribution, and mechanical properties of the inclusions. By doing so, the homogenization method provides a way to predict the overall elastic and plastic behavior of composite materials under various loading conditions.

Since the concentration tensor field in SUBC (Static Uniform Boundary Condition) problems is equivalent to the fourth-rank identity tensor $\mathbb{I}$, it simplifies to [61]

$$\langle \mathbb{A} \rangle = \langle \mathbb{B} \rangle = \mathbb{I} \tag{2.23}$$

To ensure the accuracy of the calculations, the Python script used for evaluating average stress and strain has been enhanced. This updated script now includes calculations of the strain tensor field during macroscopic simulations under SUBC conditions. These results are meticulously compared with the average strain tensor, and the identity tensor is verified to validate the computational framework.

Simulations are conducted using various sizes of RVEs, each employing PBCs. This approach enables the computation of macroscopic strain and stress tensors for each RVE size analyzed. Additionally, for macroscopic structures subjected to SUBC, average stress and strain values are derived and analyzed.

The simulations encompass all sizes detailed in Table 2.8. Stress-strain responses ob-

tained from RVEs of different sizes for the LDPE-I composite are presented in Figures 2.31 and 2.32. These figures compare simulation outcomes against experimental test results conducted at a volume fraction (V_f) of 0.10, providing comprehensive validation of the computational models against empirical data.

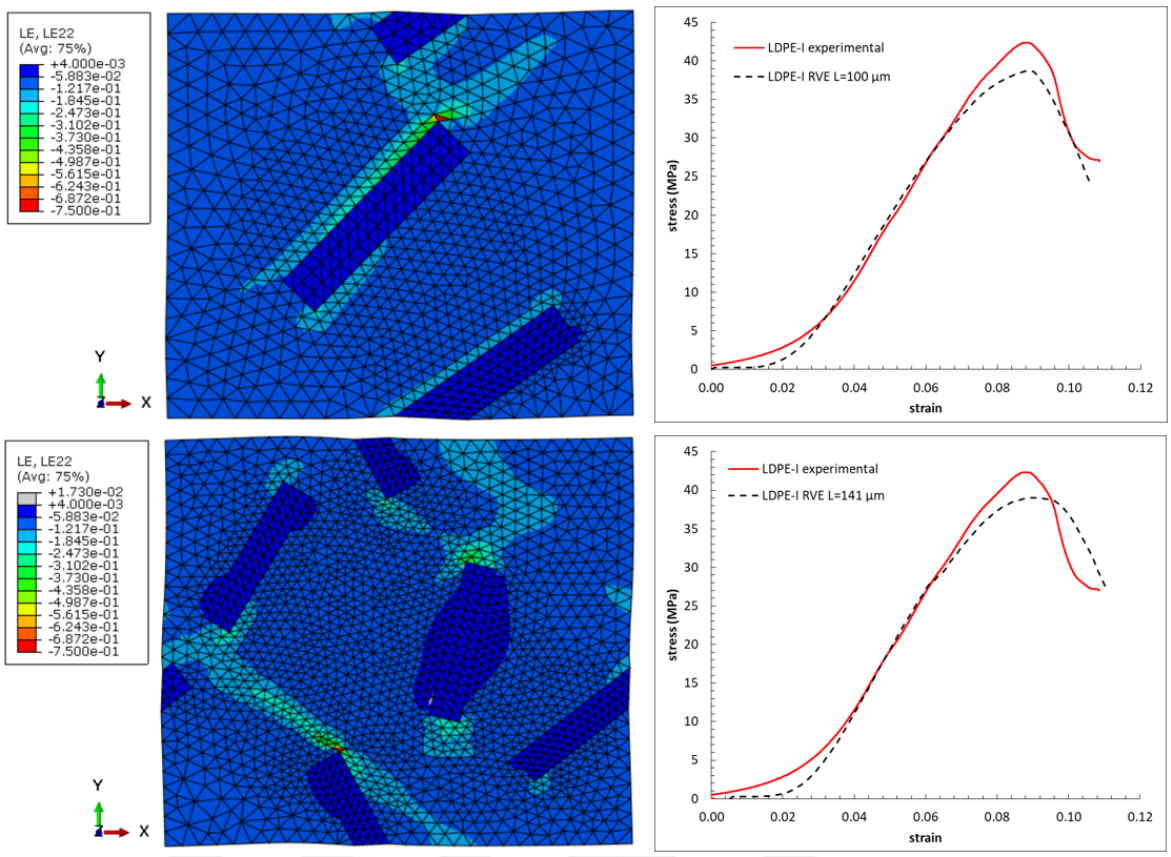

Figure 2.31: RVE with $L = 100$ μm (top) and $L = 141$ μm (bottom) for LDPE-I ($V_f = 0.10$)

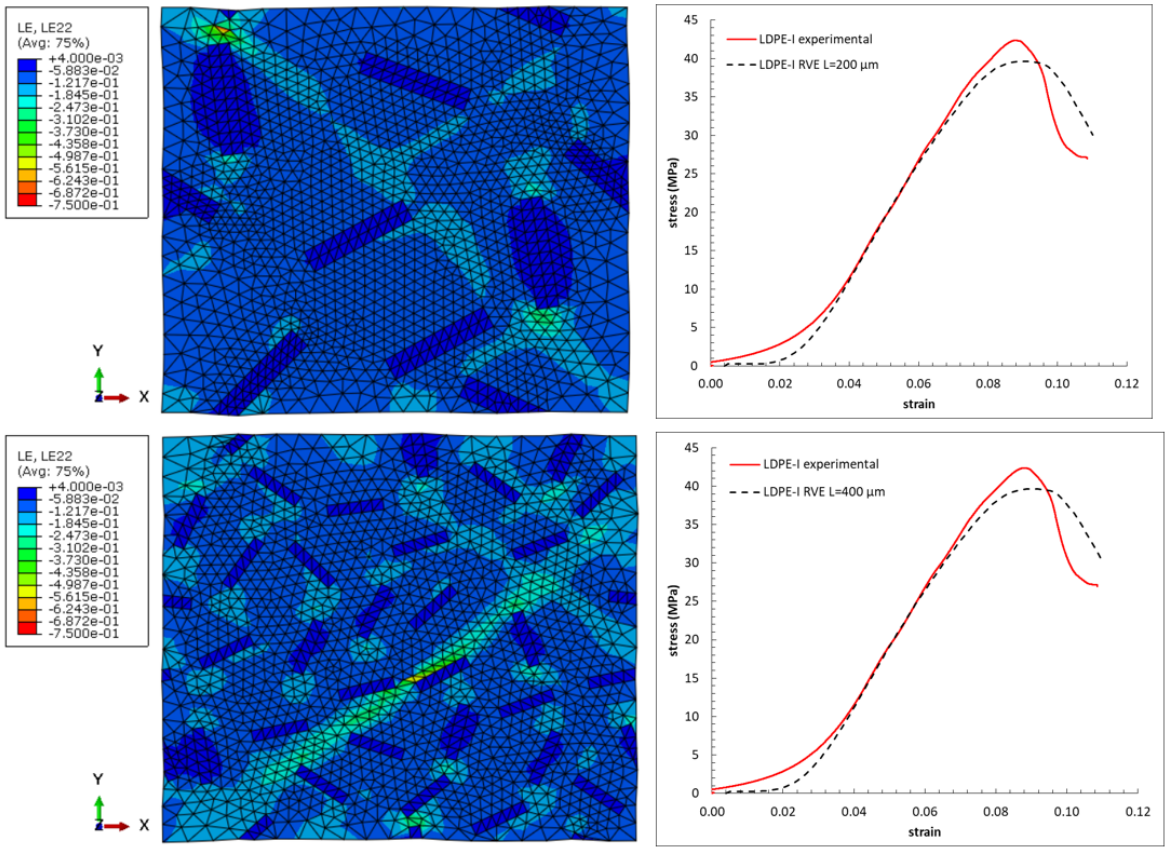

Figure 2.32: RVE with $L = 200$ μm (top) and $L = 400$ μm (bottom) for LDPE-I ($V_f = 0.10$)

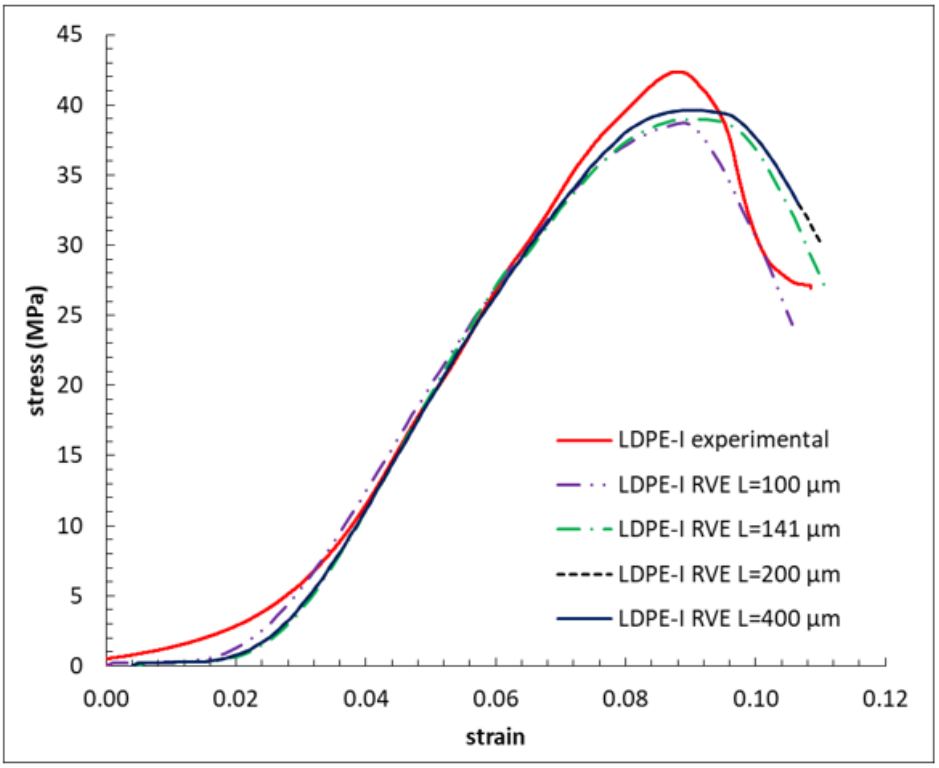

Figure 2.33: Comparison of the responses for different RVE sizes

Upon examining the simulation results (Figure 2.33) across different RVE sizes, it becomes evident that an RVE with a minimum dimension of $L = 200\ \mu$m shows a stress-strain curve that closely aligns with the macroscopic response. This finding implies that the smallest RVE size capable of representing macroscopic behavior is $L = 200\ \mu$m, establishing it as the suitable size for all volume fractions.

Furthermore, Figure 2.34 presents a comparison between the experimental and numerical results for the PU-I composite. This comparison allows for assessing the accuracy of the numerical simulations in replicating the experimental behavior of the composite material.

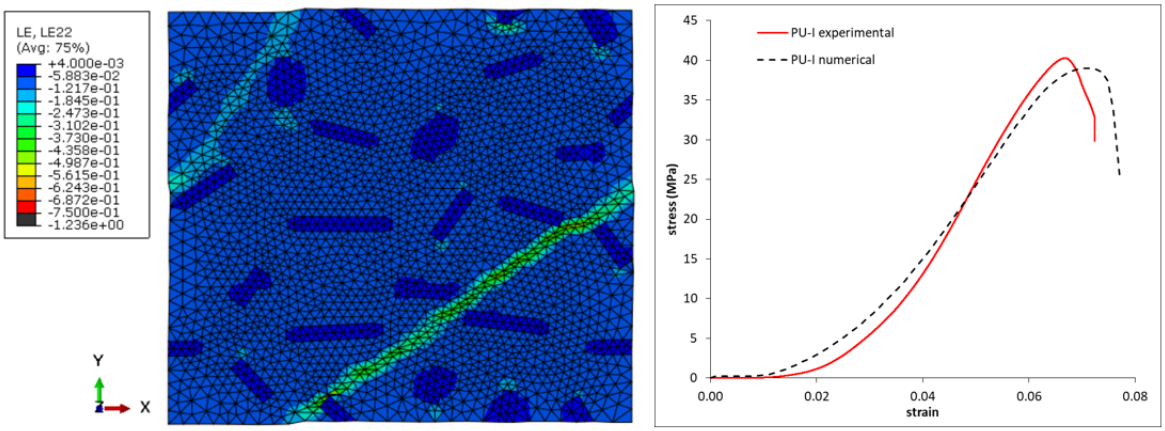

Figure 2.34: Strain contour of RVE with $L = 200$ μm (left) and comparison of responses for PU-I ($V_f = 0.10$)

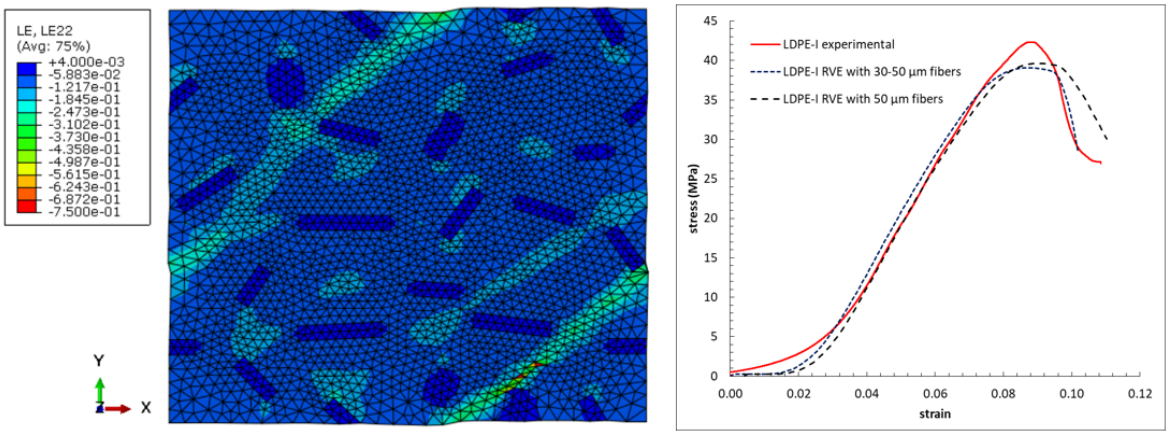

Figure 2.35: RVE with fiber length of 30-50 μm (left) and comparison of the responses (right)

The average length of both CFs and GFs used in all analyses is estimated to be 50 μm. Numerical simulations are performed to investigate the influence of varying lengths of these fibers within the predicted RVE size ($L = 200\mu m$). Inclusions ranging from 30 μm to 50 μm in length are considered, and the results are depicted in Figure **??**. It is observed that despite the changes in inclusion sizes, there is little discernible impact on the numerical outcomes. This suggests that within the analyzed range, the length variations of CFs and GFs do not significantly alter the predicted mechanical behavior of the composite.

2.3 Matrix Model Implementation in User Subroutine UMAT

2.3.1 Kinematics

2.3.1.1 Basic Kinematics

The Kroner decomposition, introduced by Kroner [70], provides a fundamental kinematical framework for the multiplicative decomposition of the deformation gradient, denoted as $\mathbf{F}(\mathbf{X})$:

$$\mathbf{F} = \mathbf{F}^e\mathbf{F}^p. \tag{2.24}$$

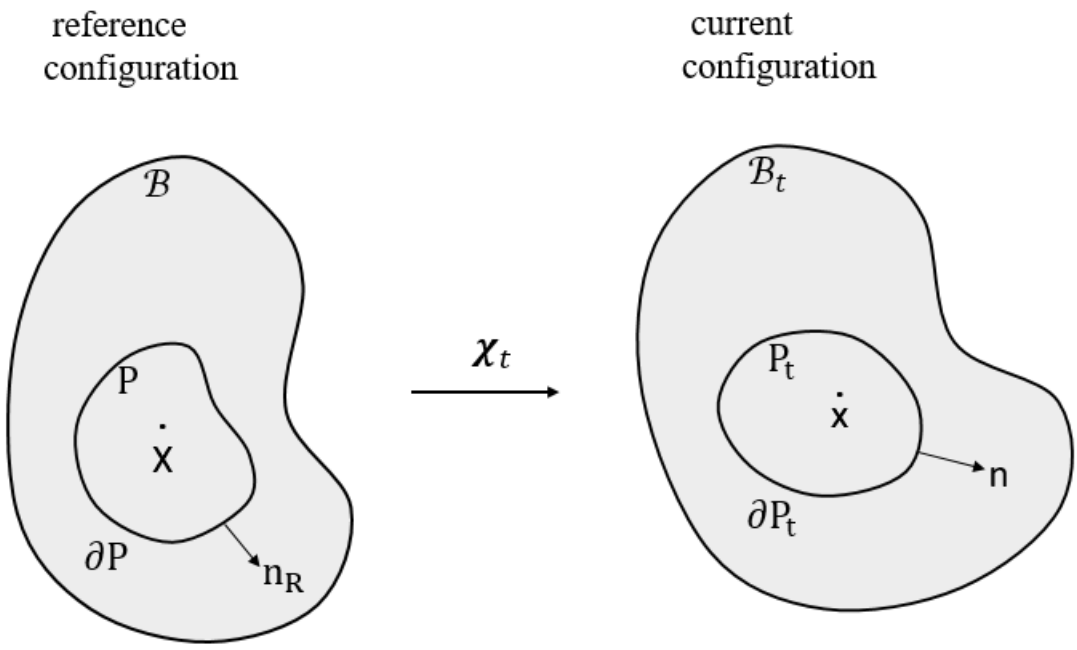

Figure 2.36: Reference undeformed configuration and a current deformed configuration of a body

The tensor $\mathbf{F}$ represents the gradient of the function $\chi(\mathbf{X}, t)$, which maps each material point $\mathbf{X}$ from a homogeneous body $\mathcal{B}$ in a fixed reference configuration to its corresponding point $\mathbf{x} = \chi(\mathbf{X}, t)$ in the deformed body's current configuration (Figure 2.36). Consequently, the deformation gradient, velocity, and velocity gradient are derived from

$$\mathbf{F} = \nabla\chi, \qquad \mathbf{u} = \dot{\chi}, \qquad \mathbf{L} = \operatorname{grad}\mathbf{u} = \dot{\mathbf{F}}\mathbf{F}^{-1}. \tag{2.25}$$

The deformation gradient $\mathbf{F}$ not only transforms material vectors to spatial vectors but is also dimensionless and invertible at all times. In Kroner decomposition, $\mathbf{F}^e$ and $\mathbf{F}^p$ are accurately described as elastic and plastic distortions, respectively. Specifically, $\mathbf{F}^e$ represents the stretch and rotation within an infinitesimal region around $\mathbf{X}$ (the material point), while $\mathbf{F}^p$ signifies the plastic deformation of material $\mathbf{X}$ as it moves from its reference configuration to its current configuration in space (Figure 2.36).

Equations $(2.25)_3$ and (2.24) provide further insights into

$$\mathbf{L} = \mathbf{L}^e + \mathbf{F}^e\mathbf{F}^p\mathbf{F}^{e-1}, \tag{2.26}$$

and

$$\mathbf{L}^e = \dot{\mathbf{F}}^e\mathbf{F}^{e-1}, \qquad \mathbf{L}^p = \dot{\mathbf{F}}^p\mathbf{F}^{p-1}. \tag{2.27}$$

The conventional approach defines the elastic and plastic stretching and spin tensors through

$$\begin{aligned} \mathbf{D}^e &= \operatorname{sym}\mathbf{L}^e, \qquad \mathbf{W}^e = \operatorname{skw}\mathbf{L}^e, \\ \mathbf{D}^p &= \operatorname{sym}\mathbf{L}^p, \qquad \mathbf{W}^p = \operatorname{skw}\mathbf{L}^p, \end{aligned} \tag{2.28}$$

so that $\mathbf{L}^e = \mathbf{D}^e + \mathbf{W}^e$ and $\mathbf{L}^p = \mathbf{D}^p + \mathbf{W}^p$.

The right and left polar decompositions of $\mathbf{F}^e$:

$$\mathbf{F}^e = \mathbf{R}^e\mathbf{U}^e = \mathbf{V}^e\mathbf{R}^e, \tag{2.29}$$

in which $\mathbf{R}^e$ represents a rotation, $\mathbf{U}^e$ and $\mathbf{V}^e$ are symmetric, positive-definite right and left stretch tensors with

$$\mathbf{U}^e = \sqrt{\mathbf{F}^{e\top}\mathbf{F}^e} \qquad \text{and} \qquad \mathbf{V}^e = \sqrt{\mathbf{F}^e\mathbf{F}^{e\top}}. \tag{2.30}$$

Then, the right elastic Cauchy-Green deformation tensor is expressed as:

$$\mathbf{C}^e = \mathbf{U}^{e2} = \mathbf{F}^{e\top}\mathbf{F}^e. \tag{2.31}$$

Incompressible, Irrotational Plastic Flow

Two fundamental assumptions are introduced concerning plastic flow kinematics:

(i) Under the assumption that plastic flow is incompressible

$$\det \mathbf{F}^p = 1 \qquad \text{and} \qquad \operatorname{tr} \mathbf{L}^p = 0. \tag{2.32}$$

$$J \overset{\text{def}}{=} \det \mathbf{F} \qquad \text{and} \qquad J^e \overset{\text{def}}{=} \det \mathbf{F}^e, \tag{2.33}$$

by (2.24) and $(2.32)_1$,

$$J = J^e\,. \tag{2.34}$$

(ii) The initial focus is on isotropic materials, where plastic flow is presumed to lack rotational components, termed as irrotational. This assumption is driven by practical considerations: the theory without plastic spin is notably easier to apply in the context of finite deformations compared to theories that incorporate plastic spin. Therefore, it is hypothesized

$$\mathbf{W}^p = \mathbf{0}. \tag{2.35}$$

It follows trivially, $\mathbf{L}^p \equiv \mathbf{D}^p$ and

$$\dot{\mathbf{F}}^p = \mathbf{D}^p\mathbf{F}^p. \tag{2.36}$$

The equivalent plastic tensile strain, $\overline{\epsilon}^p$, is defined and assumed to change according to the differential equation[1]

$$\dot{\overline{\epsilon}}^p = \sqrt{2/3}\,|\mathbf{D}^p| \quad \text{subject to the initial condition} \quad \overline{\epsilon}^p(\mathbf{X}, 0) = 0. \tag{2.37}$$

Thus, whenever $|\mathbf{D}^p| \neq 0$,

$$\mathbf{N}^p = \frac{\mathbf{D}^p}{|\mathbf{D}^p|}, \qquad \text{with} \qquad \operatorname{tr} \mathbf{N}^p = 0, \tag{2.38}$$

determines the plastic flow direction, and therefore

$$\mathbf{D}^p = \sqrt{3/2}\dot{\overline{\epsilon}}^p \mathbf{N}^p. \tag{2.39}$$

Therefore, utilizing equations (2.25), (2.26), (2.27), (2.35), and (2.38), the expression (2.26) can be reformulated for future application as

$$(\nabla\dot{\chi})\mathbf{F}^{-1} = \dot{\mathbf{F}}^e\mathbf{F}^{e-1} + \sqrt{3/2}\,\dot{\overline{\epsilon}}^p\,\mathbf{F}^e\,\mathbf{N}^p\,\mathbf{F}^{e-1}. \tag{2.40}$$

2.3.1.2 Development of the Theory Based on the Principle of Virtual Power

Following the virtual-power method introduced by Gurtin [71, 72] and further developed by Gurtin and Anand [73, 74], the theory outlined in this context relies on the premise that

- *Each independent "rate-like" kinematical descriptor—$\dot{\chi}, \dot{\boldsymbol{F}}^e$, $\dot{\overline{\epsilon}}^p$—should have its power expenditure expressed in relation to a corresponding force system that maintains its own equilibrium.*

The nature of these associated force balances is shaped by the principles of virtual power theory. When applying this principle, it's important to recognize that the rates $(\dot{\chi}, \dot{\mathbf{F}}^e, \dot{\overline{\epsilon}}^p)$ are not independent; instead, they are constrained

[1] This is a slight misuse of notation, as $\dot{\overline{\epsilon}}^p$ is not the material time derivative of $\overline{\epsilon}^p$, but is defined to be $\sqrt{2/3}$ times the norm of $\mathbf{D}^p$.

$$(\nabla\dot{\boldsymbol{\chi}})\mathbf{F}^{-1} = \dot{\mathbf{F}}^{e}\mathbf{F}^{e-1} + \sqrt{3/2}\,\dot{\bar{\epsilon}}^{p}\,\mathbf{F}^{e}\,\mathbf{N}^{p}\,\mathbf{F}^{e-1}. \tag{2.41}$$

A specified subregion of the reference body $\mathcal{B}$ is denoted as P, with $\mathbf{n}_{\mathrm{R}}$ being the outward unit normal on the boundary ∂P of P. The macroscopic and microscopic force systems accompany each evolution of the body. The macroscopic system includes a traction $\mathbf{t}\mathrm{R}(\mathbf{n}\mathrm{R})$ for each unit vector $\mathbf{n}\mathrm{R}$, which dissipates power through the velocity $\dot{\boldsymbol{\chi}}$, and an external generalized body force $\mathbf{b}\mathrm{R}$, assumed to represent inertia, which also dissipates power through $\dot{\boldsymbol{\chi}}$,[2] and an elastic stress, $\mathbf{S}^{e}$ that expends power over the elastic distortion rate, $\dot{\mathbf{F}}^{e}$.

The nonstandard microscopic systems involve a positive scalar known as the microscopic stress π, which expends power based on the rate of equivalent tensile plastic strain $\dot{\bar{\epsilon}}^{p}$. These forces demonstrate their characteristic power expenditure through $\mathcal{W}\mathrm{ext}(\mathrm{P})$, which denotes the power exerted on region P by external material, and $\mathcal{W}\mathrm{int}(\mathrm{P})$, representing the corresponding internal power expenditure within P. More specifically,

$$\begin{aligned}
\mathcal{W}_{\mathrm{ext}}(\mathrm{P}) &= \int_{\partial P} \mathbf{t}_{\mathrm{R}}(\mathbf{n}_{\mathrm{R}}) \cdot \dot{\boldsymbol{\chi}}\, dA + \int_{\mathrm{P}} \mathbf{b}_{\mathrm{R}} \cdot \dot{\boldsymbol{\chi}}\, dV, \\
\mathcal{W}_{\mathrm{ext}}(\mathrm{P}) &= \int_{\mathrm{P}} \left(\mathbf{S}^{e} : \dot{\mathbf{F}}^{e} + \pi\, \dot{\bar{\epsilon}}^{p}\right) dV,
\end{aligned} \tag{2.43}$$

where, $\mathbf{S}^{e}$ and π are defined throughout the body for all time.

Principle of Virtual Power

At a selected fixed time, the fields $\boldsymbol{\chi}$, $\mathbf{F}^{e}$ (and therefore $\mathbf{F}$ and $\mathbf{F}^{p}$), and $\mathbf{N}^{p}$ are known. We treat the fields $\dot{\boldsymbol{\chi}}$, $\dot{\mathbf{F}}^{e}$, and $\dot{\bar{\epsilon}}^{p}$ as virtual velocities, defined in accordance with (2.41). This means we denote these virtual fields as $\tilde{\boldsymbol{\chi}}$, $\tilde{\mathbf{F}}^{e}$, and $\tilde{\bar{\epsilon}}^{p}$, differentiating them from fields associated with the actual evolution of the body, as a condition:

[2] This defines,

$$\mathbf{b}_{\mathrm{R}} = \mathbf{b}_{0\mathrm{R}} - \rho_{\mathrm{R}}\ddot{\boldsymbol{\chi}}, \tag{2.42}$$

where $\mathbf{b}_{0\mathrm{R}}$ represents the conventional body force per unit volume of the reference body, and $-\rho_{\mathrm{R}}\ddot{\boldsymbol{\chi}}$ represents the inertial body force. Here, $\rho\mathrm{R}$ denotes the mass density of the referential body.

$$(\nabla\tilde{\boldsymbol{\chi}})\mathbf{F}^{-1} = \tilde{\mathbf{F}}^{e}\mathbf{F}^{e-1} + \sqrt{3/2}\,\tilde{\bar{\epsilon}}^{p}\mathbf{F}^{e}\,\mathbf{N}^{p}\,\mathbf{F}^{e-1}. \tag{2.44}$$

A generalized virtual velocity is specified as

$$\mathcal{V} = (\tilde{\boldsymbol{\chi}}, \tilde{\mathbf{F}}^{e}, \tilde{\epsilon}^{p}),$$

consistent with (2.44).

Then,

$$\begin{aligned} \mathcal{W}_{\text{ext}}(\mathrm{P}, \mathcal{V}) &= \int_{\partial \mathrm{P}} \mathbf{t}_{\mathrm{R}}(\mathbf{n}_{\mathrm{R}}) \cdot \tilde{\boldsymbol{\chi}}\, dA + \int_{P} \mathbf{b}_{\mathrm{R}} \cdot \tilde{\boldsymbol{\chi}}\, dV, \\ \mathcal{W}_{\text{ext}}(\mathrm{P}, \mathcal{V}) &= \int_{P} \left(\mathbf{S}^{e} : \tilde{\mathbf{F}}^{e} + \pi\, \tilde{\bar{\epsilon}}^{p} \right) dV. \end{aligned} \tag{2.45}$$

The principle of virtual power dictates that external and internal powers must balance each other for their respective virtual expenditures. Therefore, for any part P,

$$\mathcal{W}_{\text{ext}}(\mathrm{P}, \mathcal{V}) = \mathcal{W}_{\text{int}}(\mathrm{P}, \mathcal{V}) \quad \text{for all generalized virtual velocities } \mathcal{V}. \tag{2.46}$$

Macroscopic Force and Moment Balances

Consider a generalized virtual velocity where $\tilde{\bar{\epsilon}}^{p} \equiv 0$, and $\nabla\tilde{\boldsymbol{\chi}}\mathbf{F}^{p-1} = \tilde{\mathbf{F}}^{e}$. For the volume $\mathcal{V}$, (2.46) results in

$$\int_{\partial \mathrm{P}} \mathbf{t}_{\mathrm{R}}(\mathbf{n}_{\mathrm{R}}) \cdot \tilde{\boldsymbol{\chi}}\, dA + \int_{\mathrm{P}} \mathbf{b}_{\mathrm{R}} \cdot \tilde{\boldsymbol{\chi}}\, dV = \int_{\mathrm{P}} \mathbf{S}^{e} : \tilde{\mathbf{F}}^{e}\, dV = \int_{\mathrm{P}} (\mathbf{S}^{e}\mathbf{F}^{p-\top}) : \nabla\tilde{\boldsymbol{\chi}}\, dV, \tag{2.47}$$

and

$$\mathbf{T}_{\mathrm{R}} \overset{\text{def}}{=} \mathbf{S}^{e}\mathbf{F}^{p-\top}, \tag{2.48}$$

2.47 becomes

$$\int_{\partial \mathrm{P}} \mathbf{t}_{\mathrm{R}}(\mathbf{n}_{\mathrm{R}}) \cdot \tilde{\boldsymbol{\chi}}\, dA = \int_{\mathrm{P}} \left(\mathbf{T}_{\mathrm{R}} : \nabla \tilde{\boldsymbol{\chi}} - \mathbf{b}_{\mathrm{R}} \cdot \tilde{\boldsymbol{\chi}} \right) dV, \tag{2.49}$$

then form the divergence theorem

$$\int_{\partial \mathrm{P}} (\mathbf{t}_{\mathrm{R}}(\mathbf{n}_{\mathrm{R}}) - \mathbf{T}_{\mathrm{R}} \mathbf{n}_{\mathrm{R}}) \cdot \tilde{\boldsymbol{\chi}}\, dA + \int_{\mathrm{P}} (\mathrm{Div}\, \mathbf{T}_{\mathrm{R}} + \mathbf{b}_{\mathrm{R}}) \cdot \tilde{\boldsymbol{\chi}}\, dV = 0.$$

Given that this relationship must hold for all P and $\tilde{\boldsymbol{\chi}}$, standard variational principles lead to the traction condition.

$$\mathbf{t}_{\mathrm{R}}(\mathbf{n}_{\mathrm{R}}) = \mathbf{T}_{\mathrm{R}} \mathbf{n}_{\mathrm{R}}\,, \tag{2.50}$$

and the local macroscopic force balance

$$\mathrm{Div}\, \mathbf{T}_{\mathrm{R}} + \mathbf{b}_{\mathrm{R}} = \mathbf{0}. \tag{2.51}$$

$\mathbf{T}_{\mathrm{R}}$ denotes the classical Piola stress, and (2.51) signifies the local macroscopic force and moment balances in the reference body.

Microscopic Force Balances

To explore the microscopic counterparts of the macroscopic force balance, begin by selecting a generalized virtual velocity where $\tilde{\boldsymbol{\chi}} = \mathbf{0}$. Choose $\tilde{\bar{\epsilon}}^{p}$ arbitrarily, and define

$$\tilde{\mathbf{F}}^{e} = -\sqrt{3/2}\, \tilde{\bar{\epsilon}}^{p}\, \mathbf{F}^{e} \mathbf{N}^{p},$$

thus ensuring

$$\mathbf{S}^{\mathrm{e}} : \tilde{\mathbf{F}}^{\mathrm{e}} = -\tilde{\bar{\epsilon}}^{p} \left(\sqrt{3/2}\, (\mathbf{F}^{\mathrm{e}\top} \mathbf{S}^{\mathrm{e}}) : \mathbf{N}^{\mathrm{p}} \right). \tag{2.52}$$

Then, defining a Mandel stress

$$\mathbf{M}^{\mathrm{e}} \stackrel{\mathrm{def}}{=} \mathbf{F}^{\mathrm{e}\top} \mathbf{S}^{\mathrm{e}}, \tag{2.53}$$

and an equivalent tensile stress $\bar{\sigma}$ by

$$\bar{\sigma} \stackrel{\text{def}}{=} \sqrt{3/2}\, \mathbf{M}_0^{\text{e}} \colon \mathbf{N}^{\text{p}}\,, \tag{2.54}$$

in which $\mathbf{N}^p$ is deviatoric.

Then, the power balance described in equation (2.46) results in the formulation of the microscopic virtual-power relation.

$$0 = \int_{\text{P}} (\pi - \bar{\sigma}) \tilde{\dot{\epsilon}}^p \, dV \tag{2.55}$$

To be satisfied for all $\tilde{\dot{\epsilon}}^p$ and all P, this leads to the formulation of the first microscopic force balance.

$$\bar{\sigma} = \pi. \tag{2.56}$$

2.3.2 Free-Energy Imbalance (Second Law)

Under conditions where temperature remains constant (isothermal), the two laws of thermodynamics are simplified to assert that the change in free energy over time for any subregion P is not greater than the energy expended on P. Specifically, this requirement is expressed as a free-energy imbalance:

$$\dot{\overline{\int_{\text{P}} \psi \, dV}} \leq \mathcal{W}_{\text{ext}}(\text{P}) = \mathcal{W}_{\text{int}}(\text{P}). \tag{2.57}$$

where ψ represents the free energy per unit volume.

Since $\dot{\overline{\int_{\text{P}} \psi \, dV}} = \int_{\text{P}} \dot{\psi} \, dV$, $(2.43)_2$ can be employed to localize (2.57); the outcome is the free-energy imbalance

$$\dot{\psi} - \underbrace{\mathbf{S}^{\text{e}} \colon \dot{\mathbf{F}}^{\text{e}}}_{\text{elastic power}} - \pi \dot{\tilde{\epsilon}}^p \leq 0. \tag{2.58}$$

The "elastic power" $\mathbf{S}^{\mathrm{e}} : \dot{\mathbf{F}}^{\mathrm{e}}$ itself remains constant, but the stress $\mathbf{S}^{e}$ and the rate of elastic deformation $\dot{\mathbf{F}}^{\mathrm{e}}$ involved in this elastic power vary with changes in the frame of reference. According to standard treatments in finite elasticity, this elastic power can be described using $\dot{\mathbf{C}}^{\mathrm{e}}$ and a stress measure that is conjugate to power. Let

$$\mathbf{T}^{\mathrm{e}} \stackrel{\mathrm{def}}{=} \mathbf{F}^{\mathrm{e}\text{-}1}\mathbf{S}^{\mathrm{e}}; \tag{2.59}$$

then, since $\mathbf{S}^{\mathrm{e}}\mathbf{F}^{\mathrm{e}\top} = \mathbf{F}^{\mathrm{e}}\mathbf{T}^{\mathrm{e}}\mathbf{F}^{\mathrm{e}\top}$,

$$\mathbf{T}^{\mathrm{e}} = \mathbf{T}^{\mathrm{e}\top}. \tag{2.60}$$

Thus $\mathbf{S}^{\mathrm{e}} : \dot{\mathbf{F}}^{\mathrm{e}} = \mathbf{T}^{\mathrm{e}} : (\mathbf{F}^{\mathrm{e}\top}\dot{\mathbf{F}}^{\mathrm{e}})$,

$$\mathbf{S}^{\mathrm{e}} : \dot{\mathbf{F}}^{\mathrm{e}} = \frac{1}{2}\mathbf{T}^{\mathrm{e}} : \dot{\mathbf{C}}^{\mathrm{e}}. \tag{2.61}$$

Observe that, $\mathbf{T}^{\mathrm{e}}$ is invariant under a change in frame.

Using (2.61), the local free-energy imbalance (2.58) may be reformulated as

$$\dot{\psi} - \frac{1}{2}\mathbf{T}^{\mathrm{e}} : \dot{\mathbf{C}}^{\mathrm{e}} - \pi\dot{\bar{\epsilon}}^{p} \leq 0 \tag{2.62}$$

which serves as a guide in the development of an appropriate constitutive theory.

The dissipation density $\mathcal{D} \geq 0$ per unit volume per unit time is

$$\mathcal{D} = \frac{1}{2}\mathbf{T}^{\mathrm{e}} : \dot{\mathbf{C}}^{\mathrm{e}} + \pi\dot{\bar{\epsilon}}^{p} \geq 0. \tag{2.63}$$

The stress measures $\mathbf{S}^{\mathrm{e}}$, $\mathbf{T}$R, $\mathbf{M}^{\mathrm{e}}$, and $\mathbf{T}^{\mathrm{e}}$ have been introduced in the preceding discussion. It is important to note that the Piola stress $\mathbf{T}$R is connected to the symmetric Cauchy stress $\mathbf{T}$ in the deformed body by the standard relation:

$$\mathbf{T}_{\mathrm{R}} = J\,\mathbf{T}\mathbf{F}^{-\top}. \tag{2.64}$$

(2.48), (2.59), and (2.53) provide the following relationships between the stress measures $\mathbf{S}^{\mathrm{e}}$, $\mathbf{T}^{\mathrm{e}}$, $\mathbf{M}^{\mathrm{e}}$, and the Cauchy stress $\mathbf{T}$:

$$\mathbf{S}^{\mathrm{e}} = J\,\mathbf{T}\mathbf{F}^{e-\top}, \quad \mathbf{T}^{\mathrm{e}} = J\,\mathbf{F}^{e-1}\mathbf{T}\mathbf{F}^{e-\top}, \quad \text{and} \quad \mathbf{M}^{\mathrm{e}} = J\,\mathbf{F}^{e\top}\mathbf{T}\mathbf{F}^{e-\top} = \mathbf{C}^{\mathrm{e}}\mathbf{T}^{\mathrm{e}}. \tag{2.65}$$

2.3.3 Constitutive Equations

According to (2.37), the equivalent tensile plastic strain is given by

$$\overline{\epsilon}^{p}(\mathbf{X}, 0) = 0, \qquad \dot{\overline{\epsilon}}^{p}(\mathbf{X}, t) \geq 0, \tag{2.66}$$

Therefore, $\overline{\epsilon}^{p}$ increases with time during any process. It represents an isotropic measure of the accumulated plastic strain history in the material.

2.3.3.1 Free Energy Dissipation Density

The free energy is

$$\psi = \hat{\psi}(\mathbf{C}^{\mathrm{e}}, \overline{\epsilon}^{p}), \tag{2.67}$$

it produces the stress $\mathbf{T}^{\mathrm{e}}$ solely through the classical finite elasticity relation

$$\mathbf{T}^{\mathrm{e}} = 2\,\frac{\partial \hat{\psi}(\mathbf{C}^{\mathrm{e}}, \overline{\epsilon}^{p})}{\partial \mathbf{C}^{\mathrm{e}}}, \tag{2.68}$$

so that

$$\dot{\psi} = \frac{1}{2}\mathbf{T}^{\mathrm{e}} : \dot{\mathbf{C}}^{\mathrm{e}} + \pi_{\mathrm{en}}\,\dot{\overline{\epsilon}}^{p} \tag{2.69}$$

where the energetic microstress components π_{en}, $\boldsymbol{\rho}$en, and $\boldsymbol{\xi}$en are defined through the following relations

$$\pi_{\text{en}} = \frac{\partial \hat{\psi}(\mathbf{C}^{\text{e}}, \bar{\epsilon}^p)}{\partial \bar{\epsilon}^p} \tag{2.70}$$

Thus, the changes in energy over time are counterbalanced by the power exerted by the stress $\mathbf{T}^{\text{e}}$, which is paired with $\frac{1}{2}\dot{\mathbf{C}}^e$, and by a microstress π_{en} that is paired with $\dot{\bar{\epsilon}}^p$.

By (2.69), the dissipation density $\mathcal{D}$ determined by (2.63) is

$$\mathcal{D} = (\pi - \pi_{\text{en}})\dot{\bar{\epsilon}}^p \geq 0. \tag{2.71}$$

Based on this inequality

$$\pi_{\text{dis}} \overset{\text{def}}{=} \pi - \pi_{\text{en}} \tag{2.72}$$

the scalar and vector dissipative microstresses are defined, and (2.71) can be rewritten as follows:

$$\mathcal{D} = \pi_{\text{dis}}\dot{\bar{\epsilon}}^p \geq 0. \tag{2.73}$$

2.3.3.2 A Conventional Theory of Plasticity

The microforce balance (2.56) incorporating $(2.72)_1$ is expressed as

$$\bar{\sigma} = \pi_{\text{en}} + \pi_{\text{dis}}, \tag{2.74}$$

where π_{en} and π_{dis} denote the energetic and dissipative microstresses, respectively. Additionally, the dissipation density (2.63) is transformed to

$$\mathcal{D}_{\text{conv}} = \pi_{\text{dis}}\dot{\bar{\epsilon}}^p \geq 0. \tag{2.75}$$

It is assumed that this inequality holds strictly, meaning

$$\mathcal{D}_{\text{conv}} = \pi_{\text{dis}}\,\dot{\bar{\epsilon}}^{p} > 0 \qquad \text{when} \qquad \dot{\bar{\epsilon}}^{p} > 0. \tag{2.76}$$

Energetic Constitutive Equations

The spectral decomposition of $\mathbf{C}^e$ is given by

$$\mathbf{C}^e = \sum_{i=1}^{3} \lambda_i^{e\,2}\,\mathbf{r}_i^e \otimes \mathbf{r}_i^e, \tag{2.77}$$

where $(\mathbf{r}_1^e, \mathbf{r}_2^e, \mathbf{r}_3^e)$ are the orthonormal eigenvectors of $\mathbf{C}^e$, and $(\lambda_1^e, \lambda_2^e, \lambda_3^e)$ are the eigenvalues of $\mathbf{U}^e$.

The expression

$$\mathbf{E}^e \overset{\text{def}}{=} \sum_{i=1}^{3} (\ln \lambda_i^e)\,\mathbf{r}_i^e \otimes \mathbf{r}_i^e, \tag{2.78}$$

defines the logarithmic elastic strain.

The free energy is considered in its classical isotropic quadratic form:

$$\psi = \mu |\mathbf{E}_0^e|^2 + \frac{1}{2}\kappa (\text{tr}\,\mathbf{E}^e)^2, \tag{2.79}$$

where the logarithmic strain (2.78) is used instead of the classical infinitesimal strain tensor. Here, μ and κ represent the classical shear and bulk moduli of the infinitesimal theory [75, 76].

Using (2.68) and $(2.65)_3$, straightforward calculations show that the Mandel stress $\mathbf{M}^e$ is given by [cf., e.g., 77]

$$\mathbf{M}^e = 2\mu \mathbf{E}_0^e + \kappa (\text{tr}\,\mathbf{E}^e)\mathbf{1}. \tag{2.80}$$

With the free energy given by (2.79), and using (2.70), the energetic microstress π_{en} vanishes:

$$\pi_{\text{en}} = 0. \tag{2.81}$$

Thus, the microforce balance (2.74) simplifies to:

$$\bar{\sigma} = \pi_{\text{dis}}. \tag{2.82}$$

Dissipative Constitutive Equations

Our exploration of dissipative constitutive relations in the non-gradient theory relies on the following constitutive assumptions:

1. In the context of finite deformation theories of isotropic plasticity, following classical approaches [cf., e.g., 78], we adopt the assumption that the direction of the deviatoric Mandel stress $\mathbf{D}^p$ aligns with the direction of $\mathbf{M}_0^e$, indicating that $\mathbf{D}^p$ is parallel to $\mathbf{M}_0^e$.

$$\mathbf{N}^p = \frac{\mathbf{D}^p}{|\mathbf{D}^p|} \equiv \frac{\mathbf{M}_0^e}{|\mathbf{M}_0^e|}. \tag{2.83}$$

   Therefore, the resolved stress $\bar{\sigma} = \sqrt{3/2}, \mathbf{M}^e : \mathbf{N}^p$, as defined in (2.54), can be expressed as

$$\bar{\sigma} = \sqrt{3/2}\, |\mathbf{M}_0^e|. \tag{2.84}$$

2. A constitutive equation for π_{dis} takes the form:

$$\pi_{\text{dis}} = Y_{\text{dis}}(\overline{\epsilon}^p). \tag{2.85}$$

   Here,

$$Y_{\text{dis}}(\overline{\epsilon}^p) > 0, \tag{2.86}$$

   is a positive-valued scalar with dimensions of stress, representing the classical flow resistance of the material. The initial value

$$Y_0 \overset{\text{def}}{=} Y_{\text{dis}}(0) > 0, \tag{2.87}$$

defines the initial yield strength.

With π_{dis} defined in (2.85), the microforce balance (2.82) dictates that

$$\bar{\sigma} = Y_{\text{dis}}(\bar{\epsilon}^p) \qquad \text{when} \qquad \dot{\bar{\epsilon}}^p > 0. \tag{2.88}$$

Introducing an accumulated plastic strain and an evolution equation for the equivalent plastic strain rate:

$$\dot{\bar{\epsilon}}^p = \dot{\epsilon}_0 \left(\frac{\bar{\sigma} - \mathbf{Y}(\bar{\epsilon}^p)}{S} \right)^{1/m}. \tag{2.89}$$

The microscopic force balance incorporating power-law rate dependency is derived by inverting this relation:

$$\bar{\sigma} = \mathbf{Y}(\bar{\epsilon}^p) + S \left(\frac{\dot{\bar{\epsilon}}^p}{\dot{\epsilon}_0} \right)^m \tag{2.90}$$

where $\mathbf{Y}(\bar{\epsilon}^p, C)$ is the yield function, S is a material parameter, m is the rate-sensitivity parameter, and ϵ_0 is the reference flow rate.

Note that the yield function is decomposed into two parts: hardening, $H(\bar{\epsilon}^p)$, and softening, $S(\bar{\epsilon}^p)$, where the hardening part initially dominates and softening becomes more significant with increasing plastic strain:

$$\mathbf{Y}(\bar{\epsilon}^p) = H(\bar{\epsilon}^p) - S(\bar{\epsilon}^p) \tag{2.91}$$

For modeling the highly non-linear behavior of the polymer matrix, we adopt the following expressions for the hardening and softening functions:

$$H(\bar{\epsilon}^p) = h * e^{q_1 \cdot \bar{\epsilon}^p} * \bar{\epsilon}^p \tag{2.92}$$

$$S(\bar{\epsilon}^p) = s * (1 - e^{q_2 \cdot \epsilon^c}) * \bar{\epsilon}^p \tag{2.93}$$

In these equations, h, s, q_1, and q_2 represent model parameters. The softening function $S(\bar{\epsilon}^p)$ becomes active only when the total plastic strain exceeds a critical value ($\bar{\epsilon}^p > \epsilon^c$); otherwise, $S(\bar{\epsilon}^p) = 0$.

The specific values of these model parameters are determined through the implementation of the material model in UMAT.

hardening parameters:

- h = 15MPa
- q_1 = 73

softening parameters:

- s = 112MPa
- q_2 = 69
- ϵ^c=$\bar{\epsilon}^p$ − 0.024

To investigate the non-linear behavior of the matrix, the model is subjected to the displacement corresponding to the experimentally determined maximum strain value. Subsequently, the resulting uniaxial stress-strain response is generated and illustrated in Figure 2.37, where it is compared with both the Abaqus built-in implementation and experimental data.

The accuracy of these findings aligns well with the results obtained from prior numerical analyses. Due to its ease of implementation and suitability for handling a large number of realizations, Abaqus software has been chosen for the homogenization process.

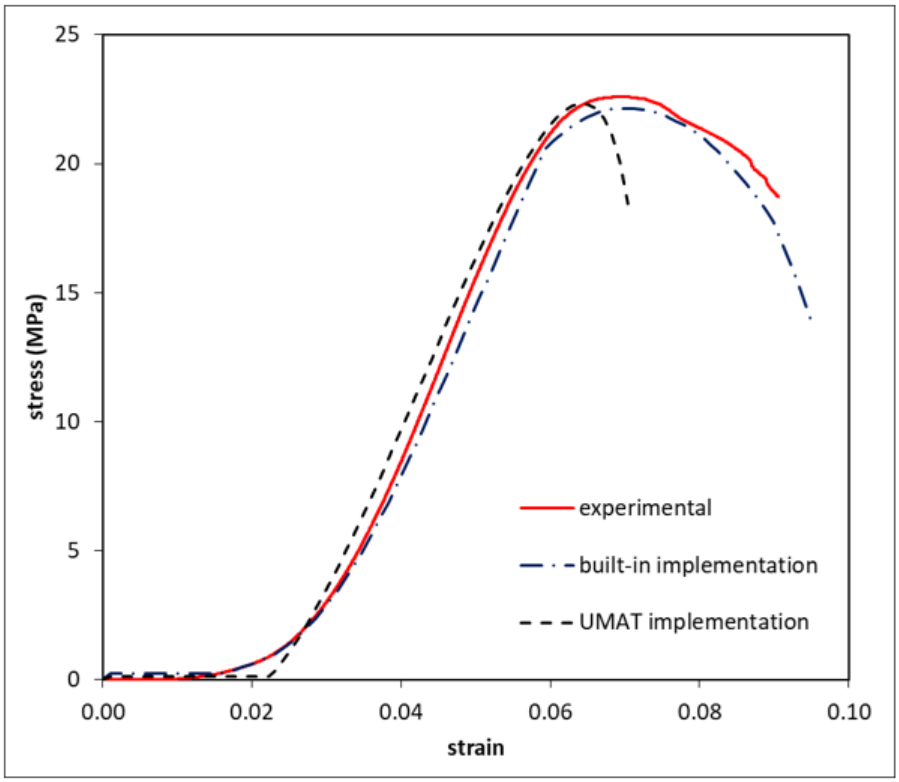

Figure 2.37: Comparison of the numerical responses of the matrix under uniaxial compression with the experimental test results

2.4 Computational Time

To assess the computational efficiency of the homogenization method, particularly in comparing the efficacy of using Representative Volume Elements (RVEs) against macrostructural analysis, we focused on the time required for computing average stress and strain values through volume integration at each integration point.

The computational tests were conducted on a robust system featuring an Intel© Xeon© Gold 6140 CPU @ 2.30GHz processor with 12 cores active out of 18 available, and 500GB of RAM, operating at a clock speed of 2.30GHz.

Table 2.9 presents a comprehensive comparison of the calculation times alongside the geometric characteristics of the models. This comparison highlights how the RVE-based homogenization method effectively addresses the intricacies of microstructure at every integration point and time step within the structure.

The goal is to illustrate the advantage of employing RVEs over traditional macrostructural analyses, particularly in terms of computational efficiency, where RVEs allow for detailed microstructural simulations at various points throughout the structure's analysis timeline.

Table 2.9: The computation time associated with the geometric models utilized in the numerical analyses

model	size	# of elements	# of nodes	# of constraint equations	CPU time (min)
micro	$L_{RVE} = 200\mu m$	3,072	1,582	94	1.09
macro	10×5 mm	817,108	408,855	-	1381

The time requirements analysis underscores a significant disparity between the macro-model and the homogenized model using RVEs. It highlights the critical need for simulations to adopt a homogenization strategy that integrates RVEs with carefully considered boundary conditions to ensure computational efficiency. This comparison underscores the essentiality of optimizing computational resources when employing homogenization techniques, particularly in complex structural analyses where detailed microstructural insights are crucial for accurate predictions and performance assessments.

2.5 Summary

Polymer-based composites, such as those incorporating matrices of Low Density Polyethylene (LDPE) and Polyurethane, have undergone extensive reinforcement processes involving the addition of fresh scrap rubber, short carbon fibers, and glass fibers. These reinforcements were strategically chosen to impart multifunctionality and enhance the mechanical properties of the composites. The manufacturing process was carefully orchestrated to ensure optimal dispersion and bonding of these additives within the polymer matrices.

To evaluate the efficacy of these reinforcement strategies, a series of rigorous analyses were conducted. This included investigating various toughening mechanisms and performing critical mechanical property assessments. Fracture toughness tests were instrumental in determining key parameters such as stress intensity factor and critical energy release rate. Microstructural investigations, facilitated by scanning electron microscopy (SEM), provided detailed insights into the interface characteristics and adhesion qualities between the polymer matrices and the different types of reinforcements. These analyses revealed favorable interfacial interactions crucial for achieving synergistic improvements in material performance.

The incorporation of fresh scrap rubber, short carbon fibers, and glass fibers resulted in substantial enhancements across both mechanical properties and fracture toughness of the polymer composites. These enhancements underscored the effectiveness of the chosen reinforcement strategies in achieving desired material characteristics and performance benchmarks.

For predictive modeling of the composite's elastic properties, an adapted version of the modified Halpin–Tsai homogenization method was employed. This method was selected for its ability to accurately capture the complex interactions between the matrix and reinforcements, highlighting the limitations of traditional analytical methods in modeling such intricate composite materials effectively.

Numerically, the study utilized multiple representative volume elements (RVEs) to simulate the behavior of the composite at the microstructural level. A custom Python script was developed to automate the generation of reinforcement configurations within

the RVEs using ABAQUS/CAE software. Implementing stringent periodic boundary conditions around the RVEs ensured that the simulations accurately represented the material's response under diverse loading conditions and across different spatial regions within the composite structure.

Validation of the numerical approach involved implementing a sophisticated multi-material model in ABAQUS/Standard, incorporating a user subroutine (UMAT) for conducting implicit nonlinear finite element simulations. This framework facilitated the replication of basic characterization tests within the RVEs, allowing for validation against experimental data. This process ensured the reliability, accuracy, and applicability of the computational methodology in analyzing and predicting the performance characteristics of the composite material.

CHAPTER 3

CONCLUSION and PERSPECTIVE

Low-density polyethylene (LDPE) and polyurethane (PU) have played significant roles in various industries due to their versatile properties and cost-effectiveness. These materials are particularly advantageous in applications such as aerospace, automotive, transportation, and construction, where reducing costs, enhancing fuel efficiency, and minimizing CO_2 emissions have been paramount goals. Consequently, developing lightweight and economical materials like LDPE and PU-based composites has been crucial for advancing these sectors.

This thesis has focused on designing LDPE and PU-based composites reinforced with micro-scale additives such as glass fibers and carbon fibers. The objective has been to develop a comprehensive numerical model for these composites and validate its predictions against experimental data.

In this study, LDPE and PU composites have been reinforced with glass fibers, chosen for their excellent weight reduction capabilities, performance attributes, ease of processing, and dimensional stability. Carbon fibers have been selected due to their exceptional tensile strength and superior thermal conductivity. After determining the optimal reinforcement configurations, specialized manufacturing processes have been employed to ensure uniform composite formation. The study has included rigorous analysis of toughening mechanisms and thorough assessments of mechanical and physical properties using fracture toughness tests. Microstructural evaluations, conducted through scanning electron microscopy (SEM), have provided insights into the fracture surfaces, highlighting strong adhesion between the reinforcements and matrix and optimal interface formation for each composite composition. Complementary

compression tests have further validated the material characterization efforts.

For predicting the elastic properties of these composites, the modified Halpin–Tsai homogenization method has been adapted, underscoring its suitability for complex composite materials. The limitations of analytical approaches like the Halpin-Tsai model in accurately predicting such materials have emphasized the necessity for precise numerical simulations.

In the numerical analysis, a robust homogenization technique has been employed to simulate the intricate microstructure of the composites. Multiple representative volume elements (RVEs) have been generated using Python scripts within the ABAQUS/CAE environment, automating the configuration of reinforcements at specified volume ratios. Crucial to computational accuracy, periodic boundary conditions have been implemented to ensure realistic micromechanical simulations across the entirety of the composite material surrounding each RVE. Careful selection of RVE size has ensured statistical representativeness of the heterogeneous composite material. Implementation of a multi-material model using ABAQUS/Standard, facilitated by a user subroutine (UMAT), has enabled implicit nonlinear finite element calculations. This approach has not only replicated basic characterization tests numerically but has also validated the results against experimental and analytical findings.

The findings of this study underscore the potential of LDPE and PU composites to significantly reduce costs and environmental impact in various applications due to their lightweight properties. The validated numerical model provides a robust framework for efficiently simulating the behavior of different composite compositions, aiding in the selection of optimal material combinations for diverse engineering applications.

Future research directions stemming from this study include expanding the developed homogenization approach to accommodate a broader range of reinforcement types, implementing advanced Python scripts for simulating RVE geometric models at the microstructural scale, modeling interfaces of micro-scale particles within composites, developing UMAT subroutines for comprehensive failure and fatigue analysis, extending multiscale homogenization methods to macroscopic structures, and optimizing parallelization efficiency for enhanced computational performance.

Future work stemming from this research includes:

- Expanding the developed homogenization approach to accommodate various types of reinforcements.
- Implementing Python scripts for simulating geometric models of RVEs at the microstructural scale.
- Modeling interfaces of micro-scale particles within the composites.
- Developing UMAT subroutine for failure and fatigue analysis.
- Extending multiscale homogenization to simulate macroscopic structures.
- Enhancing parallelization efficiency for fully optimized computational approaches.

REFERENCES

[1] P. Mallick, *Composite Materials: Science and Engineering*. CRC Press, 2012.

[2] C.A. Harper, *Handbook of Plastics Technologies: The Complete Guide to Properties and Performance*. McGraw-Hill Education, 2016, thermal conductivity of LDPE is in the range of 0.33-0.35 W/m·K.

[3] A. Patterson, "Structure and properties of ldpe," *Journal of Polymer Science*, vol. 32, pp. 467–473, 2017.

[4] M. Hassan, "Advancements in polyurethane chemistry," *Polymer Reviews*, vol. 28, pp. 193–207, 2018.

[5] S. Kim and J. Lee, "Mechanical properties of ldpe composites reinforced with recycled rubber," *Journal of Materials Science*, vol. 53, pp. 125–133, 2018.

[6] D. Smith and T. Jones, "Impact resistance of ldpe-based composites," *Polymer Composites*, vol. 22, pp. 45–52, 2017.

[7] X. Zhang and Y. Li, "Chemical resistance of ldpe and pu composites," *Journal of Polymer Research*, vol. 40, pp. 303–312, 2019.

[8] M. Hofmann, *Polyethylene: Properties, Uses and Benefits*. Nova Science Publishers, 2011.

[9] G. Ulrich and T. Poth, *Polyurethanes: Chemistry, Properties, and Applications*. Wiley-VCH, 2007.

[10] A. Fischer, "Density variations in polyurethane composites," *Polymer Science*, vol. 26, pp. 120–128, 2019.

[11] J.H. Saunders and K.C. Frisch, *Polyurethanes Chemistry and Technology*. CRC Press, 1999.

[12] R. Babu and S. Shankar, "Tensile strength of polyurethane-based composites," *Journal of Materials Science*, vol. 57, pp. 98–107, 2019.

[13] A. Smith and B. Jones, “Thermal conductivity of polyurethane foams,” *Journal of Materials Science*, vol. 40, no. 15, pp. 3987–3995, 2005.

[14] M. Johnson and L. Williams, “Polyurethane coatings: a review of recent advances and practical applications,” *Progress in Organic Coatings*, vol. 63, no. 4, pp. 386–400, 2008.

[15] X. Li, Y. Zhang, and S. Wang, “Enhanced mechanical properties of ldpe and pu composites reinforced with recycled rubber,” *Polymer Composites*, vol. 41, pp. 789–798, 2020.

[16] A. Das, M.M. Hossain, and M.Z.I. Sarker, “Mechanical properties of recycled low-density polyethylene/waste rubber powder blends: Effects of electron beam irradiation and compatibilizer,” *Journal of Vinyl and Additive Technology*, vol. 23, no. 3, pp. 217–225, 2017.

[17] Y. Liu, J. Sun, and W. Chen, “Mechanical and thermal properties of polyurethane composites filled with waste tire rubber powder,” *Polymer Composites*, vol. 40, no. 4, pp. 1372–1381, 2019.

[18] K.S. SUSlick, “Kirk-othmer encyclopedia of chemical technology,” *J. Wiley & Sons: New York*, vol. 26, pp. 517–541, 1998.

[19] A. Herrmann and R. Balmer, *Mechanical Behavior of Materials*. Prentice Hall, 2000.

[20] D.e.a. Smith, “Microstructural analysis of polymer composites,” *Microscopy and Microanalysis*, vol. 21, pp. 987–995, 2015.

[21] E.e.a. Hinton, “Finite element analysis of composite materials,” *Computational Mechanics*, vol. 27, pp. 289–302, 2001.

[22] Sudarisman and I. Davies, “Stress distribution and failure modes of carbon fiber-reinforced pu composites,” *Journal of Composite Materials*, vol. 42, pp. 1781–1797, 2008.

[23] M.e.a. Chowdhury, “Impact behavior of ldpe composites reinforced with recycled rubber,” *Journal of Applied Polymer Science*, vol. 50, pp. 1162–1171, 2013.

[24] A. Haris and S. Aziz, “Thermal properties of graphene-reinforced pu composites,” *Polymer Engineering and Science*, vol. 55, pp. 2284–2292, 2015.

[25] V. Kouznetsova, W. Brekelmans, and F. Baaijens, "An approach to micro-macro modeling of heterogeneous materials," *Computational Mechanics*, vol. 27, no. 1, pp. 37–48, 2001.

[26] J.C. Halpin, "Effects of environmental factors on composite materials," *Journal of Composite Materials*, vol. 3, no. 3, pp. 486–502, 1969.

[27] T. Mori and K. Tanaka, "Average stress in matrix and average elastic energy of materials with misfitting inclusions," *Acta Metallurgica*, vol. 21, no. 5, pp. 571–574, 1973.

[28] J.C.H. Affdl and J.L. Kardos, "The halpin-tsai equations: A review," *Polymer Engineering & Science*, vol. 16, no. 5, pp. 344–352, 1976.

[29] J.D. Eshelby, "The Determination of the Elastic Field of an Ellipsoidal Inclusion, and Related Problems," *Proceedings of the Royal Society of London Series A*, vol. 241, no. 1226, pp. 376–396, Aug. 1957.

[30] Z. Hashin, "The Elastic Moduli of Heterogeneous Materials," *Journal of Applied Mechanics*, vol. 29, no. 1, pp. 143–150, 03 1962.

[31] Z. Hashin and S. Shtrikman, "A variational approach to the theory of the elastic behaviour of multiphase materials," *Journal of the Mechanics and Physics of Solids*, vol. 11, no. 2, pp. 127–140, 1963.

[32] R. Hill, "A self-consistent mechanics of composite materials," *Journal of the Mechanics and Physics of Solids*, vol. 13, no. 4, pp. 213–222, 1965.

[33] E. Sánchez-Palencia, "Non-homogeneous media and vibration theory," *Lecture Note in Physics, Springer-Verlag*, vol. 320, pp. 57–65, 1980.

[34] A. Bensoussan, J.L. Lions, and G. Papanicolaou, *Asymptotic analysis for periodic structures*. American Mathematical Soc., 2011, vol. 374.

[35] M.J. Beran, "Statistical continuum theories," *Journal of Rheology*, vol. 9, pp. 339–355, 1965.

[36] S. Torquato, "Random Heterogeneous Media: Microstructure and Improved Bounds on Effective Properties," *Applied Mechanics Reviews*, vol. 44, no. 2, pp. 37–76, 02 1991.

[37] G.W. Milton, "The coherent potential approximation is a realizable effective

medium scheme," *Communications in Mathematical Physics*, vol. 99, pp. 463–500, 1985.

[38] J. Besson and J.L. Chaboche, *Mecanique non lineaire des materiaux*. Paris: Hermes Science Publications, 2001.

[39] E. Kröner, "Nonlinear Elastic Properties of Micro-Heterogeneous Media," *Journal of Engineering Materials and Technology*, vol. 116, no. 3, pp. 325–330, 07 1994.

[40] H. Gründemann, "Sanchez-palencia, e.; zaoui, a. (eds.), homogenization techniques for composite media. proceedings, udine, italy 1985. berlin etc., springer-verlag 1987. ix, 397 pp., dm 73,—. isbn 3-540-17616-0 (lecture notes in physics 272)," *ZAMM - Journal of Applied Mathematics and Mechanics / Zeitschrift für Angewandte Mathematik und Mechanik*, vol. 68, no. 6, pp. 212–212, 1988.

[41] S. Nemat-Nasser, *Micromechanics : overall properties of heterogeneous materials / by S. Nemat-Nasser, M. Hori.*, ser. North-Holland series in applied mathematics and mechanics ; v. 37. Amsterdam ;: North-Holland, 1993.

[42] P. Suquet, "Plasticité et homogénéisation," Ph.D. dissertation, Université Pierre et Marie Curie, Paris, France, 1982.

[43] P. Suquet, "Elements of homogenization for inelastic solid mechanics," *Homogenization techniques for composite media*, 1987.

[44] R. Hill, "Elastic properties of reinforced solids: Some theoretical principles," *Journal of the Mechanics and Physics of Solids*, vol. 11, no. 5, pp. 357–372, 1963.

[45] K. Terada and N. Kikuchi, "Nonlinear homogenization method for practical applications," *American Society of Mechanical Engineers, Applied Mechanics Division, AMD*, vol. 212, pp. 1–16, Dec. 1995, proceedings of the 1995 ASME International Mechanical Engineering Congress and Exposition ; Conference date: 12-11-1995 Through 17-11-1995.

[46] R.J.M. Smit, "Toughness of heterogeneous polymeric systems: a modeling approach," Ph.D. dissertation, Technische Universiteit Eindhoven, Eindhoven, Netherlands, 1998.

[47] R. Smit, W. Brekelmans, and H. Meijer, "Prediction of the mechanical behavior of nonlinear heterogeneous systems by multi-level finite element modeling,"

Computer Methods in Applied Mechanics and Engineering, vol. 155, no. 1, pp. 181–192, 1998.

[48] C. Miehe, J. Schröder, and J.S. Schotté, "Computational homogenization analysis in finite plasticity simulation of texture development in polycrystalline materials," *Computer Methods in Applied Mechanics and Engineering*, vol. 171, pp. 387–418, 1999.

[49] F. Feyel and J.L. Chaboche, "Fe2 multiscale approach for modelling the elastoviscoplastic behaviour of long fibre sic/ti composite materials," *Computer Methods in Applied Mechanics and Engineering*, vol. 183, pp. 309–330, 2000.

[50] H. Moulinec and P. Suquet, "A numerical method for computing the overall response of nonlinear composites with complex microstructure," *Computer methods in applied mechanics and engineering*, vol. 157, no. 1-2, pp. 69–94, 1998.

[51] C. Miehe, J. Schotte, and J. Schröder, "Computational micro–macro transitions and overall moduli in the analysis of polycrystals at large strains," *Computational Materials Science*, vol. 16, no. 1-4, pp. 372–382, 1999.

[52] M.G. Geers, V. Kouznetsova, and W. Brekelmans, "Gradient-enhanced computational homogenization for the micro-macro scale transition," *Le Journal de Physique IV*, vol. 11, no. PR5, pp. Pr5–145, 2001.

[53] V. Kouznetsova, M.G. Geers, and W.M. Brekelmans, "Multi-scale constitutive modelling of heterogeneous materials with a gradient-enhanced computational homogenization scheme," *International journal for numerical methods in engineering*, vol. 54, no. 8, pp. 1235–1260, 2002.

[54] V. Kouznetsova, M.G. Geers, and W. Brekelmans, "Multi-scale second-order computational homogenization of multi-phase materials: a nested finite element solution strategy," *Computer methods in applied Mechanics and Engineering*, vol. 193, no. 48-51, pp. 5525–5550, 2004.

[55] F. Otero, S. Oller, X. Martinez, and O. Salomón, "Numerical homogenization for composite materials analysis. comparison with other micro mechanical formulations," *Composite Structures*, vol. 122, pp. 405–416, 2015.

[56] S. Al-Salem, P. Lettieri, and J. Baeyens, "Recycling and recovery routes of plastic solid waste (psw): A review," *Waste Management*, vol. 29, no. 10, pp. 2625–2643, 2009.

[57] J. Hopewell, R. Dvorak, and E. Kosior, "Plastics recycling: Challenges and op-

portunities," *Philosophical transactions of the Royal Society of London. Series B, Biological sciences*, vol. 364, pp. 2115–26, 07 2009.

[58] A. Andrady and M. Neal, "Applications and societal benefits of plastics," *Philosophical transactions of the Royal Society of London. Series B, Biological sciences*, vol. 364, pp. 1977–84, 07 2009.

[59] H. Bhatti and I. Ahmad, "Methods for polyurethane and polyurethane composites, recycling and recovery: A review," *Reactive Functional Polymers - REACT FUNCT POLYM*, vol. 67, pp. 675–692, 08 2007.

[60] A. Aguado, L. Martínez, A. Moral, J. Fermoso, and R. Irusta, "Chemical recycling of polyurethane foam waste via glycolysis," *Chemical Engineering Transactions*, vol. 24, 05 2011.

[61] T. Kanit, S. Forest, I. Galliet, V. Mounoury, and D. Jeulin, "Determination of the size of the representative volume element for random composites: statistical and numerical approach," *International Journal of solids and structures*, vol. 40, no. 13-14, pp. 3647–3679, 2003.

[62] I. Gitman, H. Askes, and L. Sluys, "Representative volume: Existence and size determination," *Engineering Fracture Mechanics*, vol. 74, no. 16, pp. 2518–2534, 2007.

[63] Z. Hashin, "Analysis of composite materials—a survey," *Journal of Applied Mechanics*, vol. 50, pp. 481–505, 1983.

[64] W.J. Drugan and J.R. Willis, "A micromechanics-based nonlocal constitutive equation and estimates of representative volume element size for elastic composites," *Journal of Mechanics Physics of Solids*, vol. 44, no. 4, pp. 497–524, Apr. 1996.

[65] M. Ostoja-Starzewski, "Random field models of heterogeneous materials," *International Journal of Solids and Structures*, vol. 35, no. 19, pp. 2429–2455, 1998.

[66] K. Sab, "On the homogenization and the simulation of random materials," *European Journal of Mechanics A-solids*, vol. 11, pp. 585–607, 1992.

[67] C. Pelissou, J. Baccou, Y. Monerie, and F. Perales, "Determination of the size of the representative volume element for random quasi-brittle composites," *International Journal of Solids and Structures*, vol. 46, no. 14, pp. 2842–2855, 2009.

[68] L.L. Vignoli and M.A. Savi, "Multiscale failure analysis of cylindrical composite pressure vessel: A parametric study," *Latin American Journal of Solids and Structures*, vol. 15, no. Lat. Am. j. solids struct., 2018 15(11), 2018.

[69] Z. Hashin, "Theory of mechanical behavior of heterogeneous media," *Journal of Applied Mechanics*, vol. 30, no. 3, pp. 479–503, 1963.

[70] E. Kroner, "Allgemeine kontinuumstheorie der versetzungen und eigenspannungen," *Archive for Rational Mechanics and Analysis*, vol. 4, pp. 273–334, 1960.

[71] M.E. Gurtin, "On the plasticity of single crystals: Free energy, microforces, plastic-strain gradients," *Journal of the Mechanics and Physics of Solids*, vol. 48, no. 5, pp. 989–1036, 2000.

[72] M.E. Gurtin, *Configurational Forces as Basic Concepts of Continuum Physics*. Springer-Verlag, 2002.

[73] M.E. Gurtin and L. Anand, "A theory of strain-gradient plasticity for isotropic, plastically irrotational materials. part i: Small deformations," *Journal of the Mechanics and Physics of Solids*, vol. 53, no. 7, pp. 1624–1649, 2005.

[74] M.E. Gurtin and L. Anand, "Thermodynamics applied to gradient theories involving the accumulated plastic strain: The theories of aifantis and fleck and hutchinson and their generalization," *Journal of the Mechanics and Physics of Solids*, vol. 57, no. 3, pp. 405–421, 2009.

[75] L. Anand, "On h. hencky's approximate strain-energy function for moderate deformations," *Journal of Applied Mechanics*, vol. 46, no. 1, pp. 78–82, 1979.

[76] L. Anand, "Constitutive equations for hot-working of metals," *International Journal of Plasticity*, vol. 2, no. 3, pp. 213–231, 1986.

[77] S.P. Lele and L. Anand, "A large-deformation thermomechanically-coupled theory for elastomeric glasses," *Journal of the Mechanics and Physics of Solids*, vol. 57, no. 11, pp. 1811–1831, 2009.

[78] M.E. Gurtin, E. Fried, and L. Anand, "The mechanics and thermodynamics of continua," *Cambridge University Press*, 2010.

[79] L. Anand, "A thermo-mechanically-coupled theory accounting for hydrogen diffusion and large elastic-viscoplastic deformations of metals," *International Journal of Solids and Structures*, vol. 48, no. 6, pp. 962 – 971, 2011.

[80] B. Jayaraman, X. Ma, P.T. Giguere, and D.Z. Zhang, "Single and multi-velocity formulations for impact and pulverization," *International Journal of Impact Engineering*, no. 0, pp. –, 2012.

[81] D.Z. Zhang, X. Ma, and P.T. Giguere, "Material point method enhanced by modified gradient of shape function," *Journal of Computational Physics*, vol. 230, no. 16, pp. 6379 – 6398, 2011.

[82] X. Ma, P.T. Giguere, B. Jayaraman, and D.Z. Zhang, "Distribution coefficient algorithm for small mass nodes in material point method," *Journal of Computational Physics*, vol. 229, no. 20, pp. 7819 – 7833, 2010.

[83] D.Z. Zhang, Q. Zou, W.B. VanderHeyden, and X. Ma, "Material point method applied to multiphase flows," *Journal of Computational Physics*, vol. 227, no. 6, pp. 3159 – 3173, 2008.

[84] G. Weber and L. Anand, "Finite deformation constitutive equations and a time integration procedure for isotropic, hyperelastic-viscoplastic solids," *Computer Methods in Applied Mechanics and Engineering*, vol. 79, no. 2, pp. 173 – 202, 1990.

[85] M. Myhre, S. Saiwari, W. Dierkes, and J. Noordermeer, "Rubber Recycling: Chemistry, Processing, And Applications," *Rubber Chemistry and Technology*, vol. 85, no. 3, pp. 408–449, 09 2012.

[86] N. Gupta, *Reinforced Polymer Matrix Syntactic Foams Effect of Nano and Micro-Scale Reinforcement*, 1st ed., ser. SpringerBriefs in Materials. Cham: Springer International Publishing, 2013.

[87] M. Râpă, B.N. Spurcaciu, G. Coman, C.A. Nicolae, R.A. Gabor, P.N. Ghioca, A.C. Berbecaru, E. Matei, and C. Predescu, "Effect of styrene-diene block copolymers and glass bubbles on the post-consumer recycled polypropylene properties," *Materials*, vol. 13, no. 3, 2020.

[88] A. Irez, E. Bayraktar, and I. Miskioglu, "Design and mechanical-physical properties of epoxy-rubber based composites reinforced with nanoparticles," *Procedia Engineering*, vol. 184, pp. 486–496, 2017, advances in Material & Processing Technologies Conference.

[89] A.B. Irez, E. Bayraktar, and I. Miskioglu, "Recycled and devulcanized rubber modified epoxy-based composites reinforced with nano-magnetic iron oxide, fe3o4," *Composites Part B: Engineering*, vol. 148, pp. 1–13, 2018.

[90] A.B. Irez, G. Zambelis, and E. Bayraktar, "A new design of recycled ethy-

lene propylene diene monomer rubber modified epoxy based composites reinforced with alumina fiber: Fracture behavior and damage analyses," *Materials*, vol. 12, no. 17, 2019.

[91] G.C. Kabakci, O. Aslan, and E. Bayraktar, "Toughening mechanism analysis of recycled rubber-based composites reinforced with glass bubbles, glass fibers and alumina fibers," *Polymers*, vol. 13, no. 23, 2021.

[92] R.C.G. Treloar, *The Physics of Rubber Elasticity*. Oxford, UK: Oxford University Press, 1975.

[93] R.W. Ogden, *Non-linear elastic deformations*. Courier Corporation, 1997.

[94] O.H. Yeoh, "Some Forms of the Strain Energy Function for Rubber," *Rubber Chemistry and Technology*, vol. 66, no. 5, pp. 754–771, 11 1993.

[95] R.S. Marlow, *A general first-invariant hyperelastic constitutive model*. CRC Press, 2003.

[96] J. Gough, I.H. Gregory, and A.H. Muhr, "Determination of constitutive equations for vulcanized rubber," *Finite Element Analysis of Elastomers*, no. 5-26, 1999.

[97] J.R. Willis, "Variational and related methods for the overall properties of composites," *Advances in Applied Mechanics*, vol. 21, pp. 1–78, 1981.

[98] P. Suquet, *Continuum Micromechanics*, ser. CISM International Centre for Mechanical Sciences. Springer Vienna, 2014.

[99] L. Asaro, M. Gratton, S. Seghar, and N.A. Hocine, "Recycling of rubber wastes by devulcanization," *Resources, Conservation and Recycling*, vol. 133, pp. 250–262, 2018.

[100] Y. Fang, M. Zhan, and Y. Wang, "The status of recycling of waste rubber," *Materials and Design*, vol. 22, no. 2, pp. 123–128, 2001.

[101] M.M.Y. Zaghloul, Y.S. Mohamed, and H. El-Gamal, "Fatigue and tensile behaviors of fiber-reinforced thermosetting composites embedded with nanoparticles," *Journal of Composite Materials*, vol. 53, no. 6, pp. 709–718, 2019.

[102] A.B. Irez, E. Bayraktar, and I. Miskioglu, "Flexural fatigue damage analyses of recycled rubber-modified epoxy-based composites reinforced with alumina

fibres," *Fatigue & Fracture of Engineering Materials & Structures*, vol. 42, no. 4, pp. 959–971, 2019.

[103] A.K. Dhingra, N. Peacock, A.R.J.P. Ubbelohde, C. Manfre, W. Watt, B. Harris, and A.C. Ham, "Alumina fibre fp," *Philosophical Transactions of the Royal Society of London. Series A, Mathematical and Physical Sciences*, vol. 294, no. 1411, pp. 411–417, 1980.

[104] N. Platzer, "Fracture mechanics of polymers, j. g. williams, halsted press, new york, 1984, 302 pp. price: $39.95," *Journal of Polymer Science: Polymer Letters Edition*, vol. 23, no. 4, pp. 195–195, 1985.

[105] A. Geim and K. Novoselov, "The rise of graphene," *Nature materials*, vol. 6, pp. 183–91, 04 2007.

[106] Z. Zhang and H. Lei, "Preparation of α-alumina/polymethacrylic acid composite abrasive and its cmp performance on glass substrate," *Microelectronic Engineering*, vol. 85, no. 4, pp. 714–720, 2008.

[107] G. Zhang, F. Wang, J. Dai, and Z. Huang, "Effect of functionalization of graphene nanoplatelets on the mechanical and thermal properties of silicone rubber composites," *Materials*, vol. 9, no. 2, 2016.

[108] M. Shokrieh, S. Ghoreishi, and M. Esmkhani, "11 - toughening mechanisms of nanoparticle-reinforced polymers," in *Toughening Mechanisms in Composite Materials*, ser. Woodhead Publishing Series in Composites Science and Engineering, Q. Qin and J. Ye, Eds. Woodhead Publishing, 2015, pp. 295–320.

[109] C. Miehe, "Strain-driven homogenization of inelastic microstructures and composites based on an incremental variational formulation," *International Journal for Numerical Methods in Engineering*, vol. 55, no. 11, pp. 1285–1322, 2002.

[110] C. Miehe, J. Schotte, and M. Lambrecht, "Homogenization of inelastic solid materials at finite strains based on incremental minimization principles. application to the texture analysis of polycrystals," *Journal of the Mechanics and Physics of Solids*, vol. 50, no. 10, pp. 2123–2167, 2002.

[111] G. Çakır Kabakcı, Ö. Aslan, and E. Bayraktar, "Impact behaviour of recycled rubber-based composites reinforced with glass bubbles and alumina fibers (γ-al2o3)," in *Mechanics of Composite, Hybrid & Multi-functional Materials, Volume 5*, V. Chalivendra and F. Gardea, Eds. Cham: Springer International Publishing, 2023, pp. 17–28.

[112] G. K-Çakır, Ö. Aslan, and E. Bayraktar, "Toughening mechanism of recy-

cled rubber based composites reinforced with glass fibers + alumina fibers for military applications," in *Mechanics of Composite, Hybrid and Multifunctional Materials, Fracture, Fatigue, Failure and Damage Evolution, Volume 3*, V. Chalivendra, A.M. Beese, and R.B. Berke, Eds. Cham: Springer International Publishing, 2022, pp. 99–109.

[113] G.C. Kabakci, O. Aslan, and E. Bayraktar, "A review on analysis of reinforced recycled rubber composites," *Journal of Composites Science*, vol. 6, no. 8, 2022.

[114] B. Yalcin, S. Amos, M. Williams, I. Gunes, and T. Ista, "3m™ glass bubbles im16k for reinforced thermoplastics," 2016. [Online]. Available: www.3M.com/glassbubbles

[115] T.e.a. Nguyen, "Versatility of polyurethane foams and elastomers," *Advanced Polymer Technology*, vol. 29, pp. 233–247, 2020.

[116] L.e.a. Thomas, "Shore hardness in polyurethane composites," *Journal of Polymer Engineering*, vol. 34, pp. 89–98, 2019.

[117] P.e.a. Mukhopadhyay, "Elongation at break of polyurethane elastomers," *Polymer Engineering and Science*, vol. 45, pp. 143–151, 2019.

[118] S.e.a. Dasari, "Thermal insulation properties of polyurethane foams," *Journal of Applied Polymer Science*, vol. 58, pp. 203–211, 2018.

[119] K.e.a. Jayaraman, "Durability of polyurethane composites," *Journal of Polymer Research*, vol. 48, pp. 315–324, 2020.

[120] R.e.a. Siddique, "Mechanical properties of ldpe composites reinforced with recycled rubber," *Journal of Materials in Civil Engineering*, vol. 20, pp. 640–649, 2008.

[121] V.e.a. Rajan, "Tensile strength and flexibility of pu composites reinforced with recycled rubber," *Composite Structures*, vol. 140, pp. 95–106, 2016.

Appendix A

ALGORITHMS

A.1 Python Script for Creating 2D Representative Volume Elements (RVEs) with Rectangular Inclusions

This Python script is designed to generate distributed rectangular inclusions within a matrix that do not overlap and exhibit a periodic geometry. The periodic nature of the geometry ensures that an inclusion cut off on one side of the matrix will continue seamlessly on the opposite side, creating a continuous and repeatable pattern. This feature is particularly useful for simulations and analyses in materials science, where modeling the behavior of composites with regularly spaced inclusions is necessary. The script ensures that the inclusions are placed randomly but without intersecting each other, maintaining a specific volume fraction and the desired spatial distribution.

```
# FUNCTION TO CREATE 2D RVE WITH RECTANGULAR INCLUSIONS
def intersection1(newfiber, fiber, Tol):
# Calculate the diagonal length of the new fiber
F_L = newfiber[2]
F_W = newfiber[4]
dfiber1 = (F_L**2.0 + F_W**2.0)**0.5

# Calculate the diagonal length of the existing fiber
F_L = fiber[2]
F_W = fiber[4]
dfiber2 = (F_L**2.0 + F_W**2.0)**0.5
```

```
# Determine the distance between the fibers
D = ((fiber[1] - newfiber[1])**2.0 + (fiber[0] - newfiber[0])**2.0)**0.5
Dmin = dfiber1 / 2.0 + dfiber2 / 2.0 + Tol

# Check if fibers intersect
if D > Dmin:
Intersection1 = 'No'
else:
Intersection1 = 'Yes'
return Intersection1

def intersection2(newfiber, fiblist, Tol):
Intersection2 = 'No'
for fiber in fiblist:
Check = intersection1(newfiber, fiber, Tol)
if Check == 'Yes':
Intersection2 = 'Yes'
return Intersection2

def ran(x1, x2):
# Generate a random value between x1 and x2
value = (x2 - x1) * random() + x1
return value

# Initialize parameters for the RVE and fibers
W =
H =
fibwidth = ()
F_Lmax = ()
F_Lmin = ()
Tol = () * fibwidth
Vf =
```

```
# Initialize the first fiber
xc = ran(0 - F_Lmax / 2.0, W + F_Lmax / 2.0)
yc = ran(0 - F_Lmax / 2.0, H + F_Lmax / 2.0)
F_L = ran(F_Lmin, F_Lmax)
Theta = ran(0, pi)

fiblist = [[xc, yc, F_L, Theta, fibwidth]]
Vff = fibwidth * F_L / (W * H)

# Loop to add fibers until volume fraction Vf is reached
while Vff < Vf:
xc = ran(0 - F_Lmax / 2.0, W + F_Lmax / 2.0)
yc = ran(0 - F_Lmax / 2.0, H + F_Lmax / 2.0)
F_L = ran(F_Lmin, F_Lmax)
Theta = ran(0, pi)
newfiber = [xc, yc, F_L, Theta, fibwidth]
Check = intersection2(newfiber, fiblist, Tol)

if Check == 'No':
fiblist = fiblist + [newfiber]

# Check and add periodic boundary conditions
if newfiber[0] < 0:
newfiber = [xc + W, yc, F_L, Theta, fibwidth]
if Check == 'No':
fiblist = fiblist + [newfiber]
if newfiber[1] < 0:
newfiber = [xc, yc + H, F_L, Theta, fibwidth]
if Check == 'No':
fiblist = fiblist + [newfiber]
if W < newfiber[0]:
newfiber = [xc - W, yc, F_L, Theta, fibwidth]
if Check == 'No':
```

```
fiblist = fiblist + [newfiber]
if H < newfiber[1]:
newfiber = [xc, yc - H, F_L, Theta, fibwidth]
if Check == 'No':
fiblist = fiblist + [newfiber]

Vff = Vff + fibwidth * F_L / (W * H)
print Vff

# Create part (rectangle) - matrix
s = mdb.models['Model-1'].ConstrainedSketch(name='__profile__',
sheetSize=())
g, v, d, c = s.geometry, s.vertices, s.dimensions, s.constraints
s.setPrimaryObject(option=STANDALONE)
s.rectangle(point1=(0.0, 0.0), point2=(W, H))
p = mdb.models['Model-1'].Part(dimensionality=TWO_D_PLANAR,
name='Part-1', type=DEFORMABLE_BODY)
p = mdb.models['Model-1'].parts['Part-1']
p.BaseShell(sketch=s)
s.unsetPrimaryObject()
session.viewports['Viewport: 1'].setValues(displayedObject=p)
del mdb.models['Model-1'].sketches['__profile__']

# Partition
f, e, d1 = p.faces, p.edges, p.datums
t = p.MakeSketchTransform(sketchPlane=f[0], sketchPlaneSide=
SIDE1, origin=(0.0, 0.0, 0.0))
s1 = mdb.models['Model-1'].ConstrainedSketch(gridSpacing=(),
name='__profile__', sheetSize=(), transform=t)
g, v, d, c = s1.geometry, s1.vertices, s1.dimensions, s1.constraints
s1.sketchOptions.setValues(decimalPlaces=3)
s1.setPrimaryObject(option=SUPERIMPOSE)
p = mdb.models['Model-1'].parts['Part-1']
```

```
p.projectReferencesOntoSketch(filter=COPLANAR_EDGES, sketch=s1)

# Loop to create fibers
for fiber in fiblist:
xc = fiber[0]
yc = fiber[1]
Lfib = fiber[2]
Theta = fiber[3]
Sin = sin(Theta)
Cos = cos(Theta)
Wfib = fibwidth

# Calculate the coordinates of the rectangle corners
x1 = xc - (Lfib * Cos / 2 - Wfib * Sin / 2)
y1 = yc - (Lfib * Sin / 2 + Wfib * Cos / 2)

x2 = xc + (Lfib * Cos / 2 + Wfib * Sin / 2)
y2 = yc + (Lfib * Sin / 2 - Wfib * Cos / 2)

x3 = xc + (Lfib * Cos / 2 - Wfib * Sin / 2)
y3 = yc + (Lfib * Sin / 2 + Wfib * Cos / 2)

x4 = xc - (Lfib * Cos / 2 + Wfib * Sin / 2)
y4 = yc - (Lfib * Sin / 2 - Wfib * Cos / 2)

# Draw the rectangle for the fiber
s1.Line(point1=(x1, y1), point2=(x2, y2))
s1.Line(point1=(x2, y2), point2=(x3, y3))
s1.Line(point1=(x3, y3), point2=(x4, y4))
s1.Line(point1=(x4, y4), point2=(x1, y1))

p = mdb.models['Model-1'].parts['Part-1']
f = p.faces
```

```
pickedFaces = f.getSequenceFromMask(('[#1 ]',),)
e1, d2 = p.edges, p.datums
p.PartitionFaceBySketch(faces=pickedFaces, sketch=s1)
s1.unsetPrimaryObject()
del mdb.models['Model-1'].sketches['__profile__']

# Create matrix material
mdb.models['Model-1'].Material(name='matrix')
mdb.models['Model-1'].materials['matrix'].Elastic(table=(( , ),))
mdb.models['Model-1'].HomogeneousSolidSection(material='matrix',
name='matrix', thickness=None)
p = mdb.models['Model-1'].parts['Part-1']
f = p.faces
faces = f.findAt((0, 0, 0))
q = faces.index
face = f[q:q+1]
region = p.Set(faces=face, name='Set-matrix')
p = mdb.models['Model-1'].parts['Part-1']
p.SectionAssignment(region=region, sectionName='matrix',
offset=0.0,
offsetType=MIDDLE_SURFACE, offsetField='',
thicknessAssignment=FROM_SECTION)

# Create fiber material
mdb.models['Model-1'].Material(name='fiber')
mdb.models['Model-1'].materials['fiber'].Elastic(table=(( , ),))
mdb.models['Model-1'].HomogeneousSolidSection(material='fiber',
name='Section-1', thickness=None)
f = p.faces
i = 1
for fiber in fiblist:
xc = fiber[0]
yc = fiber[1]
```

```
Theta = fiber[3]
faces = f.findAt((xc, yc, 0))

face = f[q:q+1]
region = p.Set(faces=face, name='fiber-' + str(i))

p.SectionAssignment(region=region, sectionName='Section-1',
offset=0.0, offsetType=MIDDLE_SURFACE, offsetField='',
thicknessAssignment=FROM_SECTION)

p.DatumCsysByThreePoints(name='fiber-' + str(i),
coordSysType=CARTESIAN,
origin=(xc, yc, 0), point1=(xc + cos(Theta), yc + sin(Theta), 0),
point2=(xc - sin(Theta), yc + cos(Theta), 0))

datkey = mdb.models['Model-1'].parts['Part-1'].datums.keys()
q = datkey[-1]
orientation = mdb.models['Model-1'].parts['Part-1'].datums[q]

mdb.models['Model-1'].parts['Part-1'].MaterialOrientation
(region=region,orientationType=SYSTEM, axis=AXIS_3,
localCsys=orientation, fieldName='',
additionalRotationType=ROTATION_NONE, angle=0.0,
additionalRotationField='', stackDirection=STACK_3)
i = i + 1

# ASSEMBLE
mdb.models['Model-1'].rootAssembly.Instance(dependent=ON,
name='Instance-1',
part=mdb.models['Model-1'].parts['Part-1'])

# CREATE PERIODIC BOUNDARY CONDITIONS
mdb.models['Model-1'].rootAssembly.DatumCsysByDefault(CARTESIAN)
```

```
mdb.models['Model-1'].rootAssembly.Set(edges=(
mdb.models['Model-1'].rootAssembly.instances['Instance-1'].edges,),
name='PerBound')

(CoorFixNode, NameRef1, NameRef2) = PeriodicBound2D(mdb, 'Model-1',
'PerBound', [(W, 0.0), (0.0, H)],)

# CREATE STEP AND APPLY BC
mdb.models['Model-1'].StaticStep(name='Step-1', nlgeom=ON,
previous='Initial')

# Apply boundary conditions on reference nodes
DefMat = [(0.5, UNSET), (UNSET, UNSET)]
mdb.models['Model-1'].DisplacementBC(amplitude=UNSET,
createStepName='Step-1',
distributionType=UNIFORM, fieldName='', fixed=OFF, localCsys=None,
name='BC-REF-1', region=Region(referencePoints=(
mdb.models['Model-1'].rootAssembly.instances[NameRef1].
referencePoints[1],)))
mdb.models['Model-1'].DisplacementBC(amplitude=UNSET,
createStepName='Step-1', distributionType=UNIFORM, fieldName='',
fixed=OFF, localCsys=None,
name='BC-REF-2', region=Region(referencePoints=(
mdb.models['Model-1'].rootAssembly.instances[NameRef2].
referencePoints[1], )))
mdb.models['Model-1'].DisplacementBC(amplitude=UNSET,
createStepName='Step-1',
distributionType=UNIFORM, fieldName='', fixed=OFF,
localCsys=None, name='BC-FIXNODE', region=Region(
nodes=mdb.models['Model-1'].rootAssembly.instances['Instance-1'].
nodes.getByBoundingBox(H - H / 5, H - H / 5, 0, H, H, 0)),
u1=0.0, u2=0.0, ur3=UNSET)
```

```
# JOB AND RUN
mdb.Job(atTime=None, contactPrint=OFF, description='', echoPrint=OFF,
explicitPrecision=SINGLE, getMemoryFromAnalysis=True, historyPrint=OFF,
memory=90, memoryUnits=PERCENTAGE, model='Model-1', modelPrint=OFF,
multiprocessingMode=DEFAULT, name='Job-1', nodalOutputPrecision=SINGLE,
numCpus=1, queue=None, scratch='', type=ANALYSIS, userSubroutine='',
waitHours=0, waitMinutes=0)
mdb.jobs['Job-1'].submit(consistencyChecking=OFF)
```

Appendix B

ALGORITHMS-2

B.1 Python Script for Volume Integration in Stress and Strain Analysis

This appendix presents a meticulously developed Python script designed to facilitate volume integration. This process is essential for evaluating average stress and strain values at each integration point throughout the simulation, crucial for accurately modeling the mechanical behavior of heterogeneous composite materials. The script discretizes the composite volume into finite elements, calculates local stress and strain at each integration point, and aggregates these to determine the overall macroscopic stress and strain responses.

```
%# Choose loading types:
%# 0 for normal x direction
%# 1 for normal y direction
%# 2 for normal z direction
%# 3 for shear xy direction
loadlist = [0, 1, 2, 3]

# Element type being used
element_type = [' ']

# Accessing the first step in the ODB
stepim = odb.steps.values()[0]

# Initialize arrays for storing stress data
```

```
list_macroscopic_stress = np.zeros(4)
nframes = len(stepim.frames)
stress_allframes = np.zeros((nframes, 4))

print("Number of frames:", nframes)

# Loop through each frame
for x in range(nframes):
print("Processing frame", x)
currentFrame = stepim.frames[x]

# Define the region of interest (all elements in this case)
region = myAssembly.elementSets['ALL ELEMENTS']

# Extract stress and volume data at integration points
stressField = currentFrame.fieldOutputs['S']  # Stress field 'S'
strainField = currentFrame.fieldOutputs['LE']  # Strain field 'LE'
ivolField = currentFrame.fieldOutputs['IVOL']

# Subset the stress and volume fields
field_stress = stressField.getSubset(region=region,
position=INTEGRATION_POINT, elementType=' ')
field_strain = strainField.getSubset(region=region,
position=INTEGRATION_POINT, elementType=' ')
field_ivol = ivolField.getSubset(region=region,
position=INTEGRATION_POINT, elementType=' ')

# Initialize variables for calculating macroscopic stress
i = 0
for loadtype in loadlist:
# Loop through each integration point in the RVE
count = 0
vol = 0
```

```
temp_stress_times_vol = 0

# Calculate total volume and stress*volume for the current load type
for v in field_stress.values:
vol += field_ivol.values[count].data
temp_stress_times_vol += v.data[loadtype]
*field_ivol.values[count].data
count += 1

# Calculate macroscopic stress
macroscopic_stress = temp_stress_times_vol / vol
list_macroscopic_stress[i] = macroscopic_stress
i += 1

# Store calculated macroscopic stresses for the current frame
stress_allframes[x, :] = list_macroscopic_stress[:]
```

CURRICULUM VITAE

[CURRICULUM VITAE]

Surname, Name: Çakır Kabakcı, Gamze

EDUCATION

Degree	Institution	Year of Graduation
PhD	Atılım University Mechanical Engineering	2024
MS	Middle East Technical University Engineering Sciences	2018
BS	Middle East Technical University Civil Engineering	2013

FOREIGN LANGUAGES

Advanced English

PUBLICATIONS

1. Kabakci, G.C.; Aslan, O.; Bayraktar, E. "An investigation of recycled rubber composites reinforced with micro glass bubbles: An experimental and numerical approach", Composites Communications, 2023 (submitted).

2. Kabakci, G.C..; Sait F.; Baranoglu B.; Aslan, O. “Modeling and Simulation of Electromagnetic Sheet Metal Forming for Large Deformations”, Applied Science, 2023 (submitted).

3. Kabakci, G.C.; Sonar M.; Aslan, O.; Bayraktar, E. "Recycled Natural Rubber-Based Composites Reinforced with Nano Boron Nitride in Thermal Conductive and Electrical-Insulating Fields", In: Chalivendra, V., Gardea, F. (eds) Mechanics of Composite, Hybrid & Multi-functional Materials, Volume 5, Springer, Cham., 2023. https://doi.org/10.1007/978-3-031-17445-2_2

4. Kabakci, G.C.; Aslan, O.; Bayraktar E. "Impact Behaviour of Recycled Rubber-Based Composites Reinforced with Glass Bubbles and Alumina Fibers (γ-Al_2O_3)", In: Chalivendra, V., Gardea, F. (eds) Mechanics of Composite, Hybrid & Multifunctional Materials, Volume 5, Springer, Cham, 2023. https://doi.org/10.1007/978-3-031-17445-2_3

5. Kabakci, G.C.; Aslan, O.; Bayraktar, E. "A Review on Analysis of Reinforced Recycled Rubber Composites", Journal of Composites Science 6.8,225, 2022. https://doi.org/10.3390/jcs6080225

6. Kabakci, G.C.; Aslan, O.; Bayraktar, E. "Toughening Mechanism Analysis of Recycled Rubber-Based Composites Reinforced with Glass Bubbles, Glass Fibers and Alumina Fibers", Polymers, 13, 4215, 2021. https://doi.org/10.3390/polym13234215

7. Kabakci, G.C.; Aslan, O.; Bayraktar, E. "Toughening Mechanism of Recycled Rubber Based Composites Reinforced with Glass Fibers + Alumina Fibers for Military Applications.", Mechanics of Composite, Hybrid and Multifunctional Materials, Fracture, Fatigue, Failure and Damage Evolution, Volume 3, Springer Book Chapter 17, 2021. https://doi.org/10.1007/978-3-030-86741-6_17

8. Kabakci, G.C.; Aslan, O.; Bayraktar, E. "Numerical Modeling of Recycled Rubber Based Composites Reinforced with Glass Fibers at High Strain Rates", Mechanics of Composite, Hybrid and Multifunctional Materials, Fracture, Fatigue, Failure and Damage Evolution, Volume 3, Springer Book Chapter 13, 2021. https://doi.org/10.1007/978-3-030-86741-6_13